Numerical Simulation of Fluid-Fluid and Solid-Fluid Interactions: A Lattice Boltzmann Strategy

By
©Mohammad bagher Asadi

A thesis submitted to the school of Graduate Studies in partial fulfilment of the requirements for the degree of

Doctor of Philosophy

Faculty of Engineering and Applied Science
Memorial University of Newfoundland

May, 2021

St. John's, Newfoundland and Labrador
Canada

ABSTRACT

It is crucial to obtain a better understanding of fluid-fluid and solid-fluid interactions with several applications in science and engineering disciplines. Associating fluids such as water, alcohols, asphaltene might exist in many processes. Modeling associating fluids to explore phase equilibrium behaviors is required for proper design, operation, and optimization of various chemical and energy processes. Pseudopotential lattice Boltzmann method (LBM) can be a promising and capable mesoscopic approach to study phase transition and thermodynamic behaviors of complex fluid systems. Results of integrating the cubic equations of state (EOSs) with LBM showed a considerable deviation from experimental data for associating fluids. Cubic-plus-association (CPA) EOS is utilized in the LBM to increase the accuracy of modeling associating fluids. A global optimization approach is applied to determine the optimum association parameters of CPA EOS for water and primary alcohols in the lattice units. Maxwell equal area construction is used to verify the thermodynamic consistency. By increasing the isotropy order of gradient operator, the spurious velocities are decreased, and an extended form of CPA EOS is introduced to find proper initial densities, which increase the stabilities at low reduced temperatures.

Simulating fluid flow at high Reynolds number is another aspect of an LBM study that needs further improvement. In fluid flow in porous media, specifically at tight gas reservoirs, a high flow rate might happen at pore throat. Therefore, to increase the stability of the model at high Reynolds number, the central moments collision operator is implemented in the LBM. The advantages of central moments collision operator are shown by comparing with multi relaxation time (MRT) collision operator in the double shear layers test. It is found that using a higher order of isotropy in the gradient operator can lead to a 34% reduction in spurious velocities. From the thermodynamic consistency point of view, it is concluded that collision operators can also have an

impact on the consistency of the model. Furthermore, the model validation is performed by observing a straight line in the Laplace law test.

Surface wettability is known as an important concept to achieve a better understanding of fluid flow and distribution in both porous and non-porous systems. Improving the solid-fluid interaction can help to have a better understanding of thermodynamics of curved interfaces. The contact angle is an important parameter to study the multiphase fluid flow in various systems such as porous media and membranes. It helps to design better production, separation, treatment, and reaction processes in different applications. In order to increase the accuracy and reliability of the model for simulation of the surface wettability and absorption, a new solid-fluid interaction in the pseudopotential approach is introduced. Usually, the surface wettability is reported by the contact angle, which is measured by fitting a circle on the drop. Because the circle is a constant curvature shape, it is not suitable to consider the disjoining pressure. A new strategy is presented based on the Smoothing Splines to measure the contact angle without considering a constant curvature shape of the interface profile. The new solid-fluid interaction exhibits the capability of simulating extreme non-wetting surfaces without detaching the drop. The probability histogram of the density domain appears to be a reliable tool to measure the phase density in the presence of a surface.

The results of the current research have a wide range of applications in energy and environment, such as simulation of fluid flow in porous systems (e.g., shale reservoirs and membranes). Pores and fractures are large in conventional permeable media and pressure-drive convective flow is applicable in the framework of continuum flow. Shale reservoir have fine grains and pores in the range on nanometer where fluid molecular distribution is inhomogeneous and surface adsorption may be significant. Coupling the introduced method with nucleation theory provide a powerful tool to simulate asphaltene precipitation in the porous media. The presence of water component as an associating fluid in some biological processes such as blood coagulation makes the presented model an effective tool to simulate those processes.

ACKNOWLEDGMENTS

I would like to acknowledge those special people without whom this dissertation would not been accomplished.

First and foremost, I express my sincere gratitude and thanks to my supervisor, Dr. Sohrab Zendehboudi. His spectacular insights and visions have always inspired me. I would like to thank Dr. Alessandro de Rosis for his continued support and guidance towards my thesis completion. I would also like to express my sincere gratitude to Dr. M. Anne Kietzig for letting me to join her research team and learn a lot about experimental aspects of wetting phenomena.

Most importantly, none of this would have been possible without the love and patience of my family.

Last but not least, I would like to thank Memorial University (NL, Canada), InnovateNL, and Equinor (formerly Statoil) Canada for their financial support.

This thesis is dedicated to my parents, Kobra and Rostam.

Table of Contents

LIST OF TABLES

LIST OF FIGURES

1.CHAPTER ONE

Introduction and Overview

The lattice gas automaton (LGA) can be considered as the roots of the Lattice Boltzmann method (LBM) [1-4]. Simple cellular automata method was systematically studied by Wolfram; this led the first application in fluid cases [5]. This study resulted to the first technical paper that proposed a lattice gas cellular automaton (LGCA) for the N–S equations [6]. This method has been employed as an effective alternative to simulate fluid flow behavior and numerically solve nonlinear equations. LBM has been used in a wide range of engineering applications such as single-phase flow [7-9], multiphase flow [10-13], the turbulent regime in various transport phenomena [14-18], phase-change heat transfer [12, 19], and solving nonlinear partial differential equations (NPDEs) including convection-diffusion equations [20-26]. LBM is a powerful tool in the modeling of interface phenomena because of its kinetic basis [27-29]. In spite of the molecular dynamic kinetic origins of LBM, which is more fundamental compared to the continuum approaches, LBM is efficient in recovering the traditional macroscopic scale continuity and Navier–Stokes (N–S) equations. LBM does not require mesh movement and capable of being computed parallel and locally. Furthermore, handling different boundary conditions is possible with LBM.

However, two-phase/multiphase LBM classifications can be different based on different aspects such as methodology, structure, limitations and capabilities, and application [12]; however, it can be generally categorized in four groups: color-gradient [30, 31], pseudopotential [32, 33], free-energy [34, 35], and mean-field [36]. The pseudopotential LBM approach, also known as Shan-Chen (SC) approach, has received significant attention among researchers working on multiphase LBM models due to its simplicity in implementing and acceptable performance in the computation [30-35, 37]. The pseudopotential approach does not require other numerical methods to track and capture the phase segregation interfaces because of its particle interaction considerations. However, high spurious velocities and thermodynamic inconsistency are still the main challenges in employing the pseudopotential approach. Attaining high-density ratios, decreasing spurious velocity, increasing thermodynamic consistency, and increasing the Reynolds number/decreasing viscosity should be handled simultaneously in the pseudopotential approach. Thermodynamic inconsistency is tackled by introducing an effective forcing scheme [38] and new pseudopotential forms [39]. The multi-range pseudopotential, which is a combination of nearest and next-nearest neighbor interactions, was proposed by Sbragaglia et al. [40]. The double attractive pseudopotential was introduced by Falcucci et al. [41]. Higher anisotropy order of the gradient operator is implemented to overcome high spurious velocities.

To evaluate fluid-fluid interaction, Yuan and Schaefer employed different cubic and non-cubic equations of state (EOSs) in the pseudopotential approach. They assessed LBM's thermodynamic consistency by comparing the simulation results of a stationary droplet with Maxwell equal-area. Furthermore, they studied the effects of different EOSs on the maximum spurious velocity [42]. Finally, they compared the LBM results with experimental data of water; a considerable deviation in the liquid phase was noticed. Cubic EOSs such as Soave-Redlich-Kwong (SRK) [43] and Peng-Robinson (PR) [44] have been broadly applied to study the thermodynamic behaviors of hydrocarbon and non-hydrocarbon fluids due to their accuracy and simplicity. Polar components may form a stronger bonding in comparison with the physical interactions. Some unusual thermodynamic behaviors such as reverse density trend during solidification, high liquid density, and high boiling point are observed in the presence of fluids with hydrogen bonding; these phenomena may not be fully explored (and justified) by cubic EOSs [45]. Water as an associating component may exist in different fluid mixtures such as petroleum reservoir fluids in various forms such as injection fluids and connate water. As another example, asphaltene that might contain a group of complex components may form aggregates due to the association forces. To consider the association forces in associating fluids, the cubic plus association (CPA) EOS was introduced by Kontogeorgis et al. [46]. Both physical and association parts are included in the CPA EOS. In the absence of associating components, CPA turns to the cubic EOS. The CPA EOS has been widely used to study the thermodynamic conditions of complex reservoir fluids. For instance, Li and Firoozabadi presented a generalized approach based on CPA EOS to evaluate the amount of asphaltene precipitation [47-49]. For further details on CPA EOS, a general review of the CPA EOS is presented by Kontogeorgis et al. [45, 50].

Collision and streaming are the major steps of LBM simulation. Single relaxation time, also known as Bhatnagar Gross and Krook (BGK), is a common collision operator. This operator applies all the populations to relax to an equilibrium state at the same rate [51]. The BGK collision operator is unstable at high-velocity gradient cases because of non-hydrodynamic ghost modes. For decomposing the collision operator as well as raw moments, the multiple-relaxation-time (MRT) collision operator is introduced to extend the range of stable Reynolds number. These moments are mapped to different hydrodynamic parameters and their fluxes which can relax at different time scales. In the BGK collision operator, the Prandtl number is fixed by non-hydrodynamic damping modes [52] and acoustic waves [53]. One can achieve a model to adjust the Prandtl number, improve the numerical stability, and handle the modeling of complex fluids such as viscoelastic fluids in the MRT collision operator [54]. The Galilean invariance is trimmed because the MRT operator represents the collision in a frame at rest.

Recently, a novel collision kernel through shifting the lattice directions by the local fluid velocity was proposed by Geier et al. [55]. By developing the central moments (CMs) concept, a pyramidal hierarchical structure is introduced where the post-collision state of a certain moment at a given order depends on lower-order ones. Therefore, this collision operator is also known as "cascaded operator". Initially, an orthogonal basis of central moments was considered for the cascaded LBM. In spite of practical implementation specifically in three-dimensional cases [56] and overwhelming analytical formulation, this collision operator leads to a significant stability enhancement in many cases such as high Reynolds number flow, fixed and moving immersed boundaries, and convective heat transfer enhancement in jet impingement [55, 57-74]. More recently, De Rosis introduced a new LBM structure based on the central moments, which is different from the cascaded scheme in two aspects. First, the relaxation to the discrete second order shortens the equilibrium population, and second, a non-orthogonal basis is adopted. The non-pyramidal structure exhibits interesting features in terms of convergence, stability, and accuracy [75, 76].

In order to evaluate solid-fluid interactions, Martys and Chen initially introduced a solid-fluid (SF) interaction force for interaction description [77]. To adjust the contact angle, a factor is needed to represent the high-density strength of the SF interaction. At first, this factor was considered to be density; it was then supposed to be pseudopotential [27, 78, 79]. To adjust the contact angle, Benzi et al. suggested $\psi(p_w)$ [80]. Li et al. found that the ψ-based method is proper for high density ratio cases; they introduced a modified version of the pseudopotential-based SF interaction method to simulate high contact angle ranges [81]. Based on a geometric method, Hu et al. [82] also proposed an approach to predetermine the contact angle [83]. It should be mentioned that their strategy did not take into account the adsorbed layer near the solid surface [84]. Furthermore, Colosqui et al. used an SF interaction form, which includes repulsive core and attraction tails, to mimic disjoining pressure [85]. Additionally, Huang et al. [86] and Bao and Schaefer [87] applied the pseudopotential multi-component method to approximate the contact angle.

Curve fitting techniques are used in most of the aforementioned studies where a circle is fitted on the droplet to obtain the contact angle. This method is valid for droplets with a constant curvature;

however, the disjoining pressure can change the curvature of the droplet [88]. Wang [89] explained the importance of a non-constant curvature profile on the wetting dynamic. The disjoining pressure plays an essential role in many processes/phenomena, such as enhanced oil recovery (EOR) operations and membrane separation systems [90].

As the first phase in this research work, the fluid-fluid interactions are studied in the LBM. The CPA EOS is utilized in the LBM system to increase the accuracy of modeling results for association fluids. The method is validated by comparing the real data and simulation results with the Maxwell equal area construction. The Li et al.'s forcing scheme is used to improve the thermodynamic consistency. The fluid dynamic behavior of the model is enhanced by implementing the central moments as the collision operator.

In this research study, the second phase is to investigate the solid-fluid interactions in the LBM. A multi-range interaction scheme is introduced to simulate the surface wettability. To increase accuracy, a new contact angle measurement is proposed.

In terms of the applicability of the current study in real-world problems, associating fluids such as water can be present in hydrocarbon reservoirs as connate water, injection fluid, and injection fluids. Additionally, alcohol and asphaltene are considered as associating fluids. Considering associating forces in LBM is essential to study associating fluid flow in porous systems. Using the current model and implementing the nucleation theory, one can study the asphaltene precipitation in porous media. Furthermore, associating fluid like water can be considered as the main component in many biological processes.

By increasing the model's fluid dynamic stability through the implementation of central moments collision operator, the current research becomes more suitable to study fluid flow at high Reynolds number cases. This high potential is more highlighted in many practical cases such as high gas flow rate in tight and shale gas reservoirs, particularly at pore throat.

Improving the surface wettability modeling helps to better understand curved interface thermodynamics, which is needed for more accurate estimation of the gas in place, oil in place, and gas condensate at low permeable reservoirs. Further highlighting the LBM capability to handle complex boundaries, accurate and reliable simulation of the contact angle hysteresis gives a promising tool to study multiphase flow in porous media. Capillary pressure plays an essential role in multiphase flow in porous systems, which is required to design more efficient corresponding processes.

The main contributions of this research project are given below:

- A better thermodynamic consistency is achieved by implementing the CPA EOS.
- Based on the global search optimization method, a new approach is presented to determine the association parameters in the lattice units for water and primary alcohols (e.g., methanol and 1-butanol).
- Better agreement between CPA/LBM and experimental data is noticed compared to PR/LBM approach.
- The Li et al.'s forcing scheme is implemented to maintain the computations stable at low temperatures (high-density ratio) by improving the thermodynamic consistency.
- An extended version of CPA EOS is introduced for determination of initial density distribution.

- Central moments collision operator is implemented to increase the stability of the model and achieve more stable results at high Reynolds number conditions. The results are compared to the MRT collision operator while conducting the double sheer layer test.
- A new SF interaction is proposed to handle both wettability and surface adsorption, leading to a more reliable and accurate technique for contact angle determination.
- A new contact angle measurement is introduced to consider the disjoining pressure as well as the non-constant curvature drop shape.
- The probability histogram is proposed as a tool to determine the phase density in the presence of surface absorption.
- Extreme non-wetting cases can be simulated by the new solid-fluid interaction approach.

This thesis consists of three manuscripts (either published or under review for publication), as listed below:

The second chapter has been published in the Physical Review E. The impacts of increasing isotropy order of gradient operator in fluid-fluid interactions on the stability of the model and reduction of the spurious velocity are described in this manuscript. The CPA EOS is implemented in the pseudopotential approach of LBM in order to improve the thermodynamic consistency. The third chapter has been published in the Journal of Physical Chemistry B. Central moments collision operator is used to increase the stability of the model at high Raynolds numbers. The double sheer layers test is used to show greater performance of the central moment collision operator compared to MRT collision operator. The fourth chapter includes a manuscript that is under review process. A new solid-fluid interaction scheme is introduced to mimic both wettability and absorption behaviour. The new method can simulate high non-wetting cases. The last chapter covers the summary, conclusions, and recommendations for future work.

1. Aidun, C.K. and J.R. Clausen, *Lattice-Boltzmann method for complex flows.* Annual review of fluid mechanics, 2010. **42**: p. 439-472.

2. Chen, S. and G.D. Doolen, *Lattice Boltzmann method for fluid flows.* Annual review of fluid mechanics, 1998. **30**(1): p. 329-364.

3. Succi, S., *The lattice Boltzmann equation: for fluid dynamics and beyond*. 2001: Oxford university press.

4. Succi, S. and S. Succi, *The Lattice Boltzmann Equation: For Complex States of Flowing Matter*. 2018: Oxford University Press.

5. Wolfram, S., *Statistical mechanics of cellular automata.* Reviews of modern physics, 1983. **55**(3): p. 601.

6. Frisch, U., B. Hasslacher, and Y. Pomeau, *Lattice-gas automata for the Navier-Stokes equation.* Physical review letters, 1986. **56**(14): p. 1505.

7. Gupta, N., E. Fathi, and F. Belyadi, *Effects of nano-pore wall confinements on rarefied gas dynamics in organic rich shale reservoirs.* Fuel, 2018. **220**: p. 120-129.

8. Tao, S. and Z. Guo, *Boundary condition for lattice Boltzmann modeling of microscale gas flows with curved walls in the slip regime.* Physical Review E, 2015. **91**(4): p. 043305.

9. Yang, L., et al., *Boundary conditions with adjustable slip length for the lattice Boltzmann simulation of liquid flow.* Computers & Fluids, 2018. **174**: p. 200-212.

10. Abadi, R.H.H., A. Fakhari, and M.H. Rahimian, *Numerical simulation of three-component multiphase flows at high density and viscosity ratios using lattice Boltzmann methods.* Physical Review E, 2018. **97**(3): p. 033312.

11. Chen, L., et al., *A critical review of the pseudopotential multiphase lattice Boltzmann model: Methods and applications.* International Journal of Heat and Mass Transfer, 2014. **76**: p. 210-236.

12. Li, Q., et al., *Lattice Boltzmann methods for multiphase flow and phase-change heat transfer.* Progress in Energy and Combustion Science, 2016. **52**: p. 62-105.

13. Liu, H., et al., *Multiphase lattice Boltzmann simulations for porous media applications.* Computational Geosciences, 2016. **20**(4): p. 777-805.

14. Arabjamaloei, R. and D. Ruth, *Numerical study of inertial effects on permeability of porous media utilizing the Lattice Boltzmann Method.* Journal of Natural Gas Science and Engineering, 2017. **44**: p. 22-36.

15. Chai, Z., et al., *Non-Darcy flow in disordered porous media: A lattice Boltzmann study.* Computers & Fluids, 2010. **39**(10): p. 2069-2077.

16. Foroughi, S., S. Jamshidi, and M.R. Pishvaie, *New Correlative Models to Improve Prediction of Fracture Permeability and Inertial Resistance Coefficient.* Transport in Porous Media, 2018. **121**(3): p. 557-584.

17. Hasert, M., J. Bernsdorf, and S. Roller. *Lattice Boltzmann simulation of non-Darcy flow in porous media*. in *ICCS*. 2011.

18. Sukop, M.C., et al., *Evaluation of permeability and non-Darcy flow in vuggy macroporous limestone aquifer samples with lattice Boltzmann methods.* Water Resources Research, 2013. **49**(1): p. 216-230.

19. He, Y.-L., et al., *Lattice Boltzmann methods for single-phase and solid-liquid phase-change heat transfer in porous media: A review.* International Journal of Heat and Mass Transfer, 2019. **129**: p. 160-197.

20. Zhang, L., et al., *Consistent boundary conditions of the multiple-relaxation-time lattice Boltzmann method for convection–diffusion equations.* Computers & Fluids, 2018. **170**: p. 24-40.

21. Wang, H., et al., *Finite-difference lattice Boltzmann model for nonlinear convection-diffusion equations.* Applied Mathematics and Computation, 2017. **309**: p. 334-349.

22. Shi, B. and Z. Guo, *Lattice Boltzmann simulation of some nonlinear convection–diffusion equations.* Computers & Mathematics with Applications, 2011. **61**(12): p. 3443-3452.

23. Shi, B. and Z. Guo, *Lattice Boltzmann model for nonlinear convection-diffusion equations.* Physical Review E, 2009. **79**(1): p. 016701.

24. Shi, B., et al., *A new scheme for source term in LBGK model for convection–diffusion equation.* Computers & Mathematics with Applications, 2008. **55**(7): p. 1568-1575.

25. Lai, H. and C. Ma, *A higher order lattice BGK model for simulating some nonlinear partial differential equations.* Science in China Series G: Physics, Mechanics and Astronomy, 2009. **52**(7): p. 1053-1061.

26. Chai, Z., et al., *Lattice Boltzmann model for high-order nonlinear partial differential equations.* Physical Review E, 2018. **97**(1): p. 013304.

27. Sukop, M., *DT Thorne, Jr. Lattice Boltzmann Modeling Lattice Boltzmann Modeling*. 2006: Springer.

28. Huang, H., M. Sukop, and X. Lu, *Multiphase lattice Boltzmann methods: Theory and application*. 2015: John Wiley & Sons.

29. Guo, Z. and C. Shu, *Lattice Boltzmann method and its applications in engineering*. Vol. 3. 2013: World Scientific.

30. Grunau, D., S. Chen, and K. Eggert, *A lattice Boltzmann model for multiphase fluid flows.* Physics of Fluids A: Fluid Dynamics, 1993. **5**(10): p. 2557-2562.

31. Gunstensen, A.K., et al., *Lattice Boltzmann model of immiscible fluids.* Physical Review A, 1991. **43**(8): p. 4320.

32. Shan, X. and H. Chen, *Simulation of nonideal gases and liquid-gas phase transitions by the lattice Boltzmann equation.* Physical Review E, 1994. **49**(4): p. 2941.

33. Shan, X. and H. Chen, *Lattice Boltzmann model for simulating flows with multiple phases and components.* Physical Review E, 1993. **47**(3): p. 1815.

34. Swift, M.R., W. Osborn, and J. Yeomans, *Lattice Boltzmann simulation of nonideal fluids.* Physical review letters, 1995. **75**(5): p. 830.

35. Swift, M.R., et al., *Lattice Boltzmann simulations of liquid-gas and binary fluid systems.* Physical Review E, 1996. **54**(5): p. 5041.

36. He, X., S. Chen, and R. Zhang, *A lattice Boltzmann scheme for incompressible multiphase flow and its application in simulation of Rayleigh–Taylor instability.* Journal of Computational Physics, 1999. **152**(2): p. 642-663.

37. Liu, H., A.J. Valocchi, and Q. Kang, *Three-dimensional lattice Boltzmann model for immiscible two-phase flow simulations.* Physical Review E, 2012. **85**(4): p. 046309.

38. Li, Q., K.H. Luo, and X. Li, *Forcing scheme in pseudopotential lattice Boltzmann model for multiphase flows.* Physical Review E, 2012. **86**(1): p. 016709.

39. Sbragaglia, M. and X. Shan, *Consistent pseudopotential interactions in lattice Boltzmann models.* Physical Review E, 2011. **84**(3): p. 036703.

40. Sbragaglia, M., et al., *Generalized lattice Boltzmann method with multirange pseudopotential.* Physical Review E, 2007. **75**(2): p. 026702.

41. Falcucci, G., S. Ubertini, and S. Succi, *Lattice Boltzmann simulations of phase-separating flows at large density ratios: the case of doubly-attractive pseudo-potentials.* Soft Matter, 2010. **6**(18): p. 4357-4365.

42. Yuan, P. and L. Schaefer, *Equations of state in a lattice Boltzmann model.* Physics of Fluids, 2006. **18**(4): p. 042101.

43. Soave, G., *Equilibrium constants from a modified Redlich-Kwong equation of state.* Chemical engineering science, 1972. **27**(6): p. 1197-1203.

44. Peng, D.-Y. and D.B. Robinson, *A new two-constant equation of state.* Industrial & Engineering Chemistry Fundamentals, 1976. **15**(1): p. 59-64.

45. Kontogeorgis, G.M., et al., *Ten years with the CPA (Cubic-Plus-Association) equation of state. Part 1. Pure compounds and self-associating systems.* Industrial & engineering chemistry research, 2006. **45**(14): p. 4855-4868.

46. Kontogeorgis, G.M., et al., *An equation of state for associating fluids.* Industrial & engineering chemistry research, 1996. **35**(11): p. 4310-4318.

47. Li, Z. and A. Firoozabadi, *Cubic-plus-association equation of state for water-containing mixtures: Is "cross association" necessary?* AIChE journal, 2009. **55**(7): p. 1803-1813.

48. Li, Z. and A. Firoozabadi, *Cubic-plus-association equation of state for asphaltene precipitation in live oils.* Energy & fuels, 2010. **24**(5): p. 2956-2963.

49. Li, Z. and A. Firoozabadi, *Modeling asphaltene precipitation by n-alkanes from heavy oils and bitumens using cubic-plus-association equation of state.* Energy & fuels, 2010. **24**(2): p. 1106-1113.

50. Kontogeorgis, G.M., et al., *Ten years with the CPA (Cubic-Plus-Association) equation of state. Part 2. Cross-associating and multicomponent systems.* Industrial & Engineering Chemistry Research, 2006. **45**(14): p. 4869-4878.

51. Bhatnagar, P.L., E.P. Gross, and M. Krook, *A model for collision processes in gases. I. Small amplitude processes in charged and neutral one-component systems.* Physical review, 1954. **94**(3): p. 511.

52. d'Humieres, D., *Multiple–relaxation–time lattice Boltzmann models in three dimensions.* Philosophical Transactions of the Royal Society of London. Series A: Mathematical, Physical and Engineering Sciences, 2002. **360**(1792): p. 437-451.

53. Marié, S., D. Ricot, and P. Sagaut, *Comparison between lattice Boltzmann method and Navier–Stokes high order schemes for computational aeroacoustics.* Journal of Computational Physics, 2009. **228**(4): p. 1056-1070.

54. Lallemand, P. and L.-S. Luo, *Theory of the lattice Boltzmann method: Dispersion, dissipation, isotropy, Galilean invariance, and stability.* Physical Review E, 2000. **61**(6): p. 6546.

55. Geier, M., A. Greiner, and J.G. Korvink, *Cascaded digital lattice Boltzmann automata for high Reynolds number flow.* Physical Review E, 2006. **73**(6): p. 066705.

56. Premnath, K.N. and S. Banerjee, *On the three-dimensional central moment lattice Boltzmann method.* Journal of Statistical Physics, 2011. **143**(4): p. 747-794.

57. Geier, M., A. Greiner, and J.G. Korvink, *Properties of the cascaded lattice Boltzmann automaton.* International Journal of Modern Physics C, 2007. **18**(04): p. 455-462.

58. Asinari, P., *Generalized local equilibrium in the cascaded lattice Boltzmann method.* Physical Review E, 2008. **78**(1): p. 016701.

59. Geier, M., *De-aliasing and stabilization formalism of the cascaded lattice Boltzmann automaton for under-resolved high Reynolds number flow.* International journal for numerical methods in fluids, 2008. **56**(8): p. 1249-1254.

60. Geier, M., A. Greiner, and J.G. Korvink, *A factorized central moment lattice Boltzmann method.* The European Physical Journal Special Topics, 2009. **171**(1): p. 55-61.

61. Premnath, K.N. and S. Banerjee, *Incorporating forcing terms in cascaded lattice Boltzmann approach by method of central moments.* Physical Review E, 2009. **80**(3): p. 036702.

62. Geier, M., et al., *The cumulant lattice Boltzmann equation in three dimensions: Theory and validation.* Computers & Mathematics with Applications, 2015. **70**(4): p. 507-547.

63. De Rosis, A. and E. Lévêque, *Central-moment lattice Boltzmann schemes with fixed and moving immersed boundaries.* Computers & Mathematics with Applications, 2016. **72**(6): p. 1616-1628.

64. De Rosis, A., *Alternative formulation to incorporate forcing terms in a lattice Boltzmann scheme with central moments.* Physical Review E, 2017. **95**(2): p. 023311.

65. Fei, L. and K.H. Luo, *Consistent forcing scheme in the cascaded lattice Boltzmann method.* Physical Review E, 2017. **96**(5): p. 053307.

66. Geier, M., A. Pasquali, and M. Schönherr, *Parametrization of the cumulant lattice Boltzmann method for fourth order accurate diffusion part I: Derivation and validation.* Journal of Computational Physics, 2017. **348**: p. 862-888.

67. Geier, M., A. Pasquali, and M. Schönherr, *Parametrization of the cumulant lattice Boltzmann method for fourth order accurate diffusion Part II: Application to flow around a sphere at drag crisis.* Journal of Computational Physics, 2017. **348**: p. 889-898.

68. Kumar, C.S., et al., *Numerical investigations on convective heat transfer enhancement in jet impingement due to the presence of porous media using cascaded lattice Boltzmann method.* International Journal of Thermal Sciences, 2017. **122**: p. 201-217.

69. Shah, N., et al., *Cascaded collision lattice Boltzmann model (CLBM) for simulating fluid and heat transport in porous media.* Numerical Heat Transfer, Part B: Fundamentals, 2017. **72**(3): p. 211-232.

70. Sharma, K.V., R. Straka, and F.W. Tavares, *New Cascaded Thermal Lattice Boltzmann Method for simulations of advection-diffusion and convective heat transfer.* International Journal of Thermal Sciences, 2017. **118**: p. 259-277.

71. Fei, L. and K.H. Luo, *Cascaded lattice Boltzmann method for thermal flows on standard lattices.* International Journal of Thermal Sciences, 2018. **132**: p. 368-377.

72. Fei, L. and K.H. Luo, *Cascaded lattice Boltzmann method for incompressible thermal flows with heat sources and general thermal boundary conditions.* Computers & Fluids, 2018. **165**: p. 89-95.

73. Fei, L., K.H. Luo, and Q. Li, *Three-dimensional cascaded lattice Boltzmann method: Improved implementation and consistent forcing scheme.* Physical Review E, 2018. **97**(5): p. 053309.

74. Geier, M. and A. Pasquali, *Fourth order Galilean invariance for the lattice Boltzmann method.* Computers & Fluids, 2018. **166**: p. 139-151.

75. De Rosis, A., *Nonorthogonal central-moments-based lattice Boltzmann scheme in three dimensions.* Physical Review E, 2017. **95**(1): p. 013310.

76. Rosis, A.D., R. Huang, and C. Coreixas, *Universal formulation of central-moments-based lattice Boltzmann method with external forcing for the simulation of multiphysics phenomena.* Physics of Fluids, 2019. **31**: p. 117102.

77. Martys, N.S. and H. Chen, *Simulation of multicomponent fluids in complex three-dimensional geometries by the lattice Boltzmann method.* Physical review E, 1996. **53**(1): p. 743.

78. Raiskinmäki, P., et al., *Lattice-Boltzmann simulation of capillary rise dynamics.* Journal of statistical physics, 2002. **107**(1-2): p. 143-158.

79. Raiskinmäki, P., et al., *Spreading dynamics of three-dimensional droplets by the lattice-Boltzmann method.* Computational Materials Science, 2000. **18**(1): p. 7-12.

80. Benzi, R., et al., *Mesoscopic modeling of a two-phase flow in the presence of boundaries: the contact angle.* Physical Review E, 2006. **74**(2): p. 021509.

81. Li, Q., et al., *Contact angles in the pseudopotential lattice Boltzmann modeling of wetting.* Physical Review E, 2014. **90**(5): p. 053301.

82. Hu, A., et al., *Contact angle adjustment in equation-of-state-based pseudopotential model.* Physical Review E, 2016. **93**(5): p. 053307.

83. Ding, H. and P.D. Spelt, *Wetting condition in diffuse interface simulations of contact line motion.* Physical Review E, 2007. **75**(4): p. 046708.

84. Guo, L., et al., *Modeling adsorption with lattice Boltzmann equation.* Scientific reports, 2016. **6**: p. 27134.

85. Colosqui, C.E., et al., *Mesoscopic model for microscale hydrodynamics and interfacial phenomena: Slip, films, and contact-angle hysteresis.* Physical Review E, 2013. **87**(1): p. 013302.

86. Huang, H., et al., *Proposed approximation for contact angles in Shan-and-Chen-type multicomponent multiphase lattice Boltzmann models.* Physical Review E, 2007. **76**(6): p. 066701.

87. Bao, J. and L. Schaefer, *Lattice Boltzmann equation model for multi-component multi-phase flow with high density ratios.* Applied Mathematical Modelling, 2013. **37**(4): p. 1860-1871.

88. Starov, V. and M. Velarde, *Surface forces and wetting phenomena.* Journal of Physics: Condensed Matter, 2009. **21**(46): p. 464121.

89. Wang, H., *From contact line structures to wetting dynamics.* Langmuir, 2019. **35**(32): p. 10233-10245.

90. Fang, C., S. Sun, and R. Qiao, *Structure, Thermodynamics, and Dynamics of Thin Brine Films in Oil–Brine–Rock Systems.* Langmuir, 2019. **35**(32): p. 10341-10353.

2. CHAPTER TWO

Hybridized Method of Pseudopotential Lattice Boltzmann and Cubic-Plus-Association EOS Assesses Thermodynamic Characteristics of Associating Fluids

Preface

A version of this manuscript has been published in the Physical Review E 2019. **100**(4): p. 043302. Asadi, M.B. and Zendehboudi, S. are the authors of this paper. Asadi along with the co-author developed the conceptual thermodynamic and lattice Boltzmann models. Both authors designed the manuscript's structure. Most of the literature review, data collection, and the performance comparison of different methods were done by Asadi, M.B., as the first author. The first draft and the revised version of the manuscript were prepared by the first author based on the co-author's feedback and comments received from journal reviewers. The co-author, Zendehboudi, S., supervised the first author, guided the project, and edited the manuscript.

ABSTRACT

It is crucial to properly describe the associating fluids in terms of phase equilibrium behaviours, which are needed for design, operation, and optimization of various chemical and energy processes. Pseudopotential lattice Boltzmann method (LBM) appears to be a reliable and efficient approach to study thermodynamic behaviours and phase transition of complex fluid systems. However, when conventional/cubic equations of state (EOSs) are incorporated into single-component multiphase LBM, simulation results are not well matched with experimental data. This study presents the utilization of cubic-plus-association (CPA) EOS in the LBM structure to obtain more accurate modeling results for associating fluids. A new approach based on the global search optimization algorithm is introduced to find the optimal association parameters of CPA EOS for water and primary alcohols in the lattice units. The thermodynamic consistency is verified by the Maxwell construction and is also improved by the Li et al. forcing scheme [1,2]. The spurious velocity is reduced with increasing isotropy in the gradient operator. Furthermore, an extended version of CPA EOS is introduced, which increases the system stability at low reduced temperatures. There is a very good match between the LBM results and experimental data, confirming the reliability of the model developed in the present study. The introduced approach has potential to be employed for simulating transport phenomena and interfacial characteristics of associating fluids in porous systems.

Keywords: Pseudopotential Lattice Boltzmann; Cubic-Plus-Association; Maxwell Construction; Global Search Optimization; Spurious Velocity

2.1 INTRODUCTION

Cubic equations of state (EOSs) such as Peng-Robinson (PR) [3] and Soave-Redlich-Kwong (SRK) [4] have been extensively used to model thermodynamic behaviours of hydrocarbon and non-hydrocarbon fluids, due to their simplicity and accuracy. Unusual thermodynamic behaviors are generally experienced for fluids with hydrogen bonds while employing cubic EOSs [5]. Water is an associating component, which commonly exists in various mixtures such as petroleum reservoir fluids as a connate water and injection fluid. Taking another example, asphaltene molecules as a group of complex components may form aggregates due to the association forces. The bonding among polar components is stronger than physical interactions. Therefore, the associating fluids may not be fully described by cubic EOSs [6]. The cubic plus association (CPA) EOS was introduced by Kontogeorgis et al. [7] to consider the association effects in associating fluids. The CPA EOS has both physical and association parts so that it turns to the cubic EOS in the absence of associating components. In fact, the additional term in the CPA EOS exhibits the association impacts, which is originated from the Wertheim's theory. This is the same association expression that is utilized in the statistical association fluid theory (SAFT) EOS. The CPA EOS has been broadly employed to study the thermodynamic conditions of complex reservoir fluids. For example, Li and Firoozabadi introduced a generalized strategy based on the CPA EOS to determine the amount of asphaltene precipitation [8-10]. A general review on the CPA EOS can be found in the works conducted by Kontogeorgis et al. [5, 11].

On the basis of the Reynolds-averaged Navier–Stokes (RANS) equations, the computational fluid dynamics (CFD) has been successfully implemented in several mechanical and chemical engineering cases. The applications of large eddy simulation (LES) and direct numerical simulation (DNS) approaches have been considerably increased due to the strong computational capability of supercomputers. However, these methods are based on the continuum assumption. Hence, they might not be able to capture the micro/mesoscale physics of targeted processes/phenomena. On the other hand, some basic modeling particle-based techniques have been introduced to provide better physical insights of multiphase flow systems. For instance, quantum molecular simulation (QMS), molecular dynamic simulation (MD), direct simulation Monte Carlo (DSMC), and dissipative particle dynamic (DPD) appear to be efficient strategies to explore the molecular interactions and forces as well as detailed mechanisms of phenomena occurring at micro/mesoscales. However, these tools dictate high computational costs, which may make them unfeasible/uneconomical in practical scenarios.

Figure 2-1 provides some information such as computational costs, scale, and physical insights corresponding to the experimental and modeling techniques with focus on flow in porous media. The flow regime is also categorized based on the Knudsen number. As mentioned before, the modeling technique are divided into the continuum based and particle-dynamic based modeling approaches. Additionally, the experimental techniques and their scale are demonstrated. According to Figure 2-1, as the capability of modeling techniques is increased, the computational costs will increase.

The lattice Boltzmann method (LBM) as a mesoscale technique was introduced in the 1980’s [12, 13]. The LBM is recognized as a strategy based on a particle picture to obtain the macroscopic properties of fluids and processes [14]. Over the past three decades, LBM has been used in a variety of engineering and science problems such as single phase flow [15-17], multiphase flow [1, 18-20], phase-change heat transfer [1, 21], and turbulent regime in various transport phenomena [22-26]. This method can be also utilized as a tool to solve non-linear partial differential equations (PDEs) [27-32].

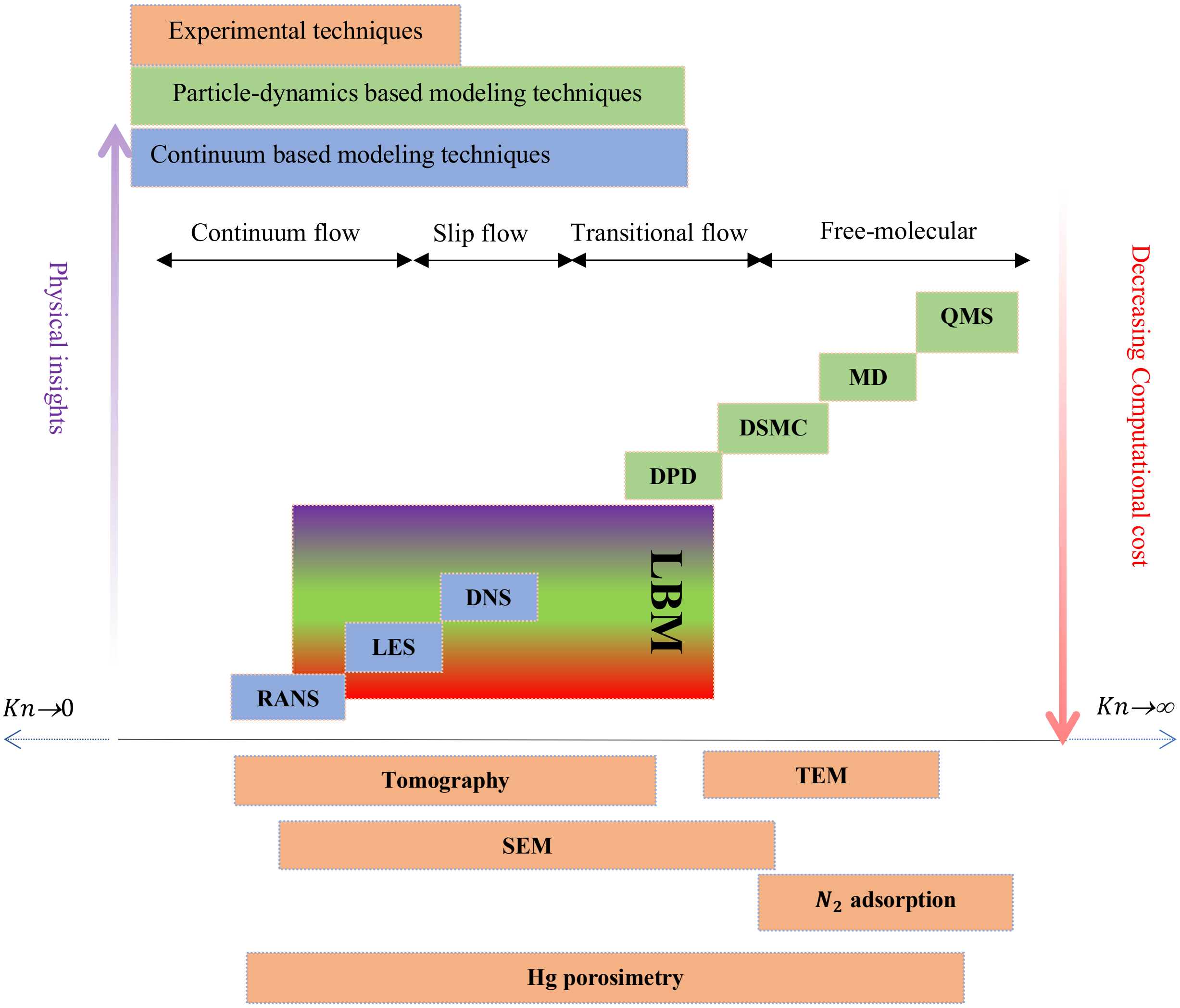

Figure 2-1 Experimental and modeling approaches to investigate transport phenomena in porous media, modified after [1, 2]. [QMS is the quantum molecular simulation; MD is the molecular dynamic simulation; DSMC refers to the direct simulation Monte Carlo; DPD is the dissipative particle dynamic; LBM refers to the lattice Boltzmann method; DNS is the direct numerical simulation; LES represents the large eddy simulation; RANS refers to the Reynolds-averaged Navier –Stokes; TEM is the transmission electron microscopy; and SEM denotes the scanning electron microscope] (The scale of methods is shown approximately and there are overlaps between different methods.).

Multiphase/multicomponent interfaces play a crucial role in several soft matters and complex fluids. Interfaces are deformable and not known a priori. Therefore, different techniques have been proposed to study the dynamics of interfaces [31]. The methodologies fall into two main categories [33]. First, the interface-tracking methods such the front tracking approach [34], which track the interface by marking a cluster of points. The second class is the interface-capturing techniques including the level set method [35], volume of fluid method (VOF) [36], and phase filled approach [37] that capture the interface by evaluating an order parameter.

Several multiphase LBM approaches have been developed during the past three decades. The color-gradient method [38, 39], free energy model [40], interface tracking model (also known as HCZ technique) [41], and pseudopotential [42] are the most common multiphase LBMs. More details about various LBM approaches are provided in the literature [14, 19, 20, 43-47]. Among the LBM techniques, the pseudopotential approach (also known as Shan-Chen) has been widely used in some research studies due to its mesoscopic feature and computational simplicity [43-48]. In this approach, the interactions between molecules are represented by a pseudopotential, which is density dependent. Microscopic molecular short-range interactions between different phases are taken into account in this method. Therefore, the interface-capturing or explicit interface-tracking is not required anymore, which leads to different/unique features for the pseudopotential model, compared to most of other multiphase models [19]. The pseudopotential LBM has some drawbacks. For instance, it suffers from high spurious velocity as the density ratio of two phases is increased near a curved interface. Shan showed that increasing the order of isotropic gradient operator can lower the spurious velocity [49]. The mid-range potential can be an alternative to enlarge the interface thickness and to decrease the spurious velocity by considering the nearest and next nearest-neighbor interactions [50]. Sbragaglia and Shan proposed a consistent form of the pseudopotential and compared it with the common form of the pseudopotential function available in the literature when a simulation was performed using the 8th order of isotropy [51]. Khajepor et al. introduced a multi-pseudopotential interaction (MPI) scheme to meet the thermodynamic consistency by determining the interaction strength pseudopotential constants through a trial and error procedure [52]. Later on, Khajepor and Chen mapped the cubic EOS (e.g., SRK and PR) to MPI when the Gou et al.'s forcing scheme was employed [53]. Li et al. introduced a new forcing scheme to meet the thermodynamic consistency when the Carnahan-Starling (C-S) EOS was utilized in the pseudopotential function [54]. The implemented forcing scheme represents the exact Navier-Stokes equations.

Yuan and Schaefer suggested a method of integrating LBM with different EOSs [55]. They evaluated the performance of cubic and non-cubic EOSs and determined the maximum density ratio. The coexistence curves of static bubbles, which were simulated by LBM, were compared with the coexistence curves obtained from the Maxwell construction. Kupershtokh et al. obtained a higher density ratio by introducing the exact difference method (EDM) force scheme [56]. In the Yuan and Schaefer's method, different densities in some specific ranges might give the same effective mass, where the physical basis of the original Shan-Chen pseudopotential LBM may be lost [55]. Zhang and Tian proposed an extra parameter to avoid this problem. However, it leads to a high spurious current and low-density ratio and it does not meet the Galilean invariance [57]. Yuan and Schaefer compared the LBM results of different EOSs with the experimental saturated density data of water [55]. An appreciable difference between the LBM results and real data was reported in the liquid phase region. In this study, we aim to increase the LBM accuracy and reliability (or lower the difference between the LBM outputs and experimental data) for associating fluids by filling the knowledge gap described above. For this purpose, CPA EOS is incorporated into the LBM strategy. It should be noted that the computational cost is lower while using the CPA EOS, compared to other EOSs such as perturbed-chain statistical associating fluid theory (PC-SAFT) that take into account the associating forces. Further highlighting the main contribution of the current study, the parameters of CPA EOS are redefined in the lattice units with the aid of an effective global optimization search method. We also introduce a new perturbation, which guarantees the thermodynamic consistency and/or stability of the model within a broad range of thermodynamic conditions, particularly at low temperatures.

The remaining of this chapter is organized as follows. First, a review on CPA EOS, LBM, framework of their combination, and the numerical modeling set up are presented in the THEORY AND METHODOLOGY section. Then, the model limitations/drawbacks are given in the LIMITATIONS section. The modeling validation, results of numerical runs, and interpretation of the results trends are reported in the RESULTS AND DISCUSSION section. In fact, the method is validated through comparing the simulation results with the Maxwell equal area construction and real data. The thermodynamic consistency is improved by using the Li et al.'s forcing scheme. The reliability of the introduced CPA EOS/LBM is also examined where the experimental data of water and simulation results are compared. By increasing the order of isotropic gradient operator, the method stability at low reduced temperatures is also discussed in this section. Lastly, the main outcomes of the current study are listed in the CONCLUSIONS section.

2.2 THEORY AND METHODOLOGY

First, the structure and theory of LBM and CPA EOS are briefly presented in this section. We will then describe the integration of LBM and CPA EOS as well as the setup and required steps in the numerical modeling approach.

Fundamentals of LBM. The Boltzmann equation with the collisional term is expressed as follows [58]:

$$\frac{\partial f}{\partial t}+\mathbf{v}\frac{\partial f}{\partial \mathbf{x}}+\frac{\boldsymbol{F}}{\rho}\frac{\partial f}{\partial \mathbf{x}}=\Omega \tag{2-1}$$

where $f(\mathbf{x},\mathbf{v},t)$ denotes the particle distribution function; x refers to the spatial coordination; v is the particle velocity; t symbolizes the time; ρ represents the fluid density; and F stands for the force. The parameter Ω in the right-hand side of Equation (2-1) represents the collision term, which describes the particle distribution function due to the particle collisions. The velocity space is discretized into a finite set of vectors, $\{e_i\}$, along with the lattice structure in the space. Thus, the destruction density function is discretized $\{f(\mathbf{x},\mathbf{v})\}$ in the LBM. The lattice Boltzmann equation (LBE) is a nonlinear differential integral equation, which is targeted to be approximated by the LBM from the particle point of view [58]. A common way to simplify the collisional integral term is using a single relaxation time towards a suitable local equilibrium, which is known as Bhatnagar−Gross−Krook (BGK). The LBE can be written in the lattice based on the BKG approximation, as given below [58]:

$$\mathrm{f}_i(x+\boldsymbol{e}_i\delta_t,t+\delta_t)-\mathrm{f}_i(x,t)=\frac{\delta_t}{\tau}\left(\mathrm{f}_i^{eq}(x,t)-\mathrm{f}_i(x,t)\right)+S_i \quad i=0,1,2,\ldots \tag{2-2}$$

in which, S_i introduces the forcing source and e_i symbolizes the discrete velocities. The left hand side of Equation (2-2) represents the molecular free-streaming, and the right-hand side of Equation (2) signifies the time relaxation (due to collisions) towards the local Maxwellian equilibrium f_i^{eq} on a time scale τ [14, 43, 47, 59]. The Maxwellian equilibrium function is truncated at the second order to recover the correct hydrodynamic balance in the isothermal regime as follows:

$$\mathrm{f}_\mathrm{i}^{eq}=\omega_i\rho_i\left[1+\frac{\boldsymbol{u_a e_{ia}}}{c_S^2}+\frac{\boldsymbol{u_a u_b}\colon(\boldsymbol{e_{ia}e_{ib}}-c_S^2\delta_{ab})}{2c_S^4}\right] \tag{2-3}$$

In Equation (2-3), $c_S=c/\sqrt{3}$ denotes the speed of sound where $c=\delta_x/\delta_t$. δ_t and δ_x represent the lattice time step and spacing, respectively; δ_{ab} is the Kronecker delta where a and b designate the Cartesian components; u is the velocity; the ω_i's symbolize a set of weights, which impose the isotropy of the hydrodynamic equations [14, 43, 47].

Figure 2-2 demonstrates up to 16th order of the isotropy and associated weights in a two-dimensional (2D) domain. Grid points indicate a set of velocity fields and the size and color of points represent the magnitude of weights. The method of calculating the extent of weights for higher orders of isotropy are explained with details in the references [60] and [50]. One can calculate the fluid density ρ and velocity u from the first and the second momentum of density distribution function as given below:

$$\rho = \sum_i \mathrm{f_i} \tag{2-4}$$

$$\rho\mathbf{u} = \sum_i \mathrm{f_i} e_i \tag{2-5}$$

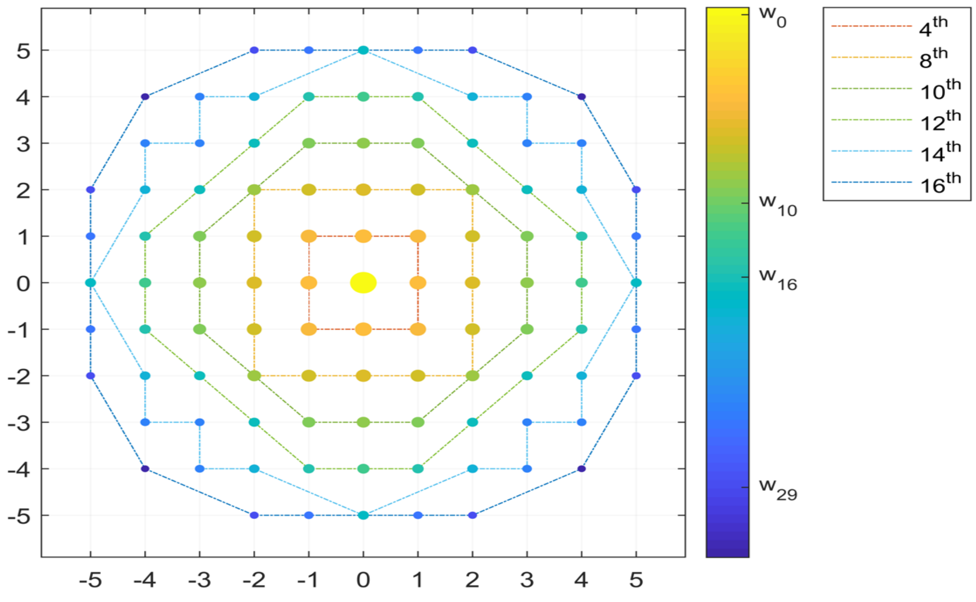

Figure 2-2: Different orders of isotropy in 2D domain. The value of weights is determined by size and color of grids.

Pseudopotential interactions in LBM. In the pseudopotential LBM, a mean-field intraction force is employed to mimic the molecular intractions that cause the phase sepration. Based on the local fluid density, an intraction potential (ψ) is defined and the intraction force is calculated from the intractions that lead to phase separation. In the single-component multiphase (SCMP) LBM, the interparticle force is given as the summation of the pairwise intractions among a particle at a specified lattice site and those at neghboring sites. The interparticle force (F_{int}) can be defined by the following equation:

$$\boldsymbol{F}_{int}(x,t) = -G\psi(x,t)\sum_{i=0}^{q}\omega_i\psi(x+\boldsymbol{e}_i,t)e_i \tag{2-6}$$

where G is a controlling parameter of the interparticle strength. The intraction force can be expanded through the Taylor series as follows [54]:

$$\boldsymbol{F}_{int} = -\mathrm{G}c^2[\psi\nabla\psi + \frac{1}{2}c^2\psi\nabla(\nabla^2\psi) + \cdots] \tag{2-7}$$

To evaluate the mechanical balance at the interface, the pressure tensor should be determined. The following general rule of the force balance is used to obtain the pressure tensor [61]:

$$\Sigma P.A = \Sigma_x F \tag{2-8}$$

For the one-dimensional interface, the analytical expression of the normal pressure tensor (up to the second-order derivative) is given below [61]:

$$P_n = c_s^2\rho + \frac{1}{2}Gc^2\psi^2(\rho) + \frac{Gc^4}{12}\left[\alpha\left(\frac{d\psi}{dn}\right)^2 + \beta\psi\frac{d^2\psi}{dn^2}\right] \tag{2-9}$$

In Equation (2-9), $\alpha = 1 - 3e^4$ and $\beta = 1 + 6e^4$. e^4 refers to the fourth-order tensor associated with the weights, as defined below [51]:

$$e^4 = \frac{\omega_1}{2} + 2\omega_2 + 8\omega_4 + 25\omega_5 + 32\omega_8 + \cdots \tag{2-10}$$

The first two diagonal terms of the pressure tensor for the bulk homogenous phase transition (P_b) are obtained by the non-ideal equation of state as follows [55, 62]:

$$P_b = c_s^2\rho + \frac{1}{2}Gc^2\psi^2(\rho) \tag{2-11}$$

Therefore, when the density is known, one can calculate the pressure P_b using the CPA EOS. In this method, the association forces will be considered. The magnitude of G for the SCMP case is not important as it will be canceled out if the bulk pressure definition is used to determine the pseudopotential function (see Equations (2-6) and (2-11)). P_n should be equal to a constant static bulk pressure at the equilibrium, which leads to the following mechanical stability condition [61]:

$$\int_{\rho_g}^{\rho_l}\left(p_0 - \rho c_s^2 - \frac{Gc^2}{2}\psi^2\right)\frac{\psi'}{\psi^{1+\epsilon}}dp = 0 \tag{2-12}$$

where $\epsilon = -2\alpha/\beta$; and ρ_l and ρ_g stand for the liquid and gas density, respectively. Li et al. proposed the following general forcing scheme [54]:

$$S_i = \omega_i\delta_t[\frac{B_a\boldsymbol{e_{ia}}}{c_s^2} + \frac{C_{ab}\colon(\boldsymbol{e_{ia}e_{ib}} - c_s^2\delta_{ab})}{2c_s^4}] \tag{2-13}$$

where

$$B_a = B_eF_a, \quad C_{ab} = C_e(\boldsymbol{v_b}F_a + \boldsymbol{v_a}F_b) \tag{2-14}$$

B_e and C_e are the constants, which are determined based on the forcing scheme. Li et al. introduced a modified velocity v', which is defined as $v' = v + \sigma'F/(\boldsymbol{\nu}\psi^2)$. $\boldsymbol{\nu} = (\tau - 0.5)$ stands for the kinematic viscosity and σ' is a constant. In the case of $\sigma' = 0$, the forcing scheme will reduce to the Guo et al.'s forcing structure [63]. Hence, implementing Li et al.'s forcing approach improves the thermodynamic consistency by adding an extra term to the Navier-Stokes equations, which is not dependent on a local quantity.

Cubic plus association equation of state. The CPA EOS was introduced by Kontogeorgis et al. [7]. This EOS is a combination of a cubic EOS and an association term taken from the Wertheim theory. Originally, the Soave-Redlich-Kwong (SRK) EOS was utilized to describe the physical part of the CPA EOS. Firoozabadi used Peng-Robinson (PR) EOS, which is more suitable for thermodynamic modeling of hydrocarbon reservoir fluids [6]. The association term considers the specific site-site interactions due to hydrogen bonding, which appears in two categories; namely, self-association (between the same species) and cross-association (between different species). The association term is based on the Wertheim's first-order thermodynamic perturbation theory (TPT-1) [64]. The system pressure is represented by the CPA EOS as follows [6]:

$$\mathrm{P} = \frac{\mathrm{RT}}{\mathrm{v-b}} - \frac{a}{v(v+b)+b(v-b)} - \frac{1}{2}\frac{RT}{v}\left(1 - v\frac{\partial lng}{\partial v}\right)\Sigma_i x_i \Sigma_{Ai}(1 - X_{Ai}),\ i = 1,2,\ldots,n_c \tag{2-15}$$

where P refers to the pressure; R is the universal gas constant; T introduces the absolute temperature; v is the molar volume; x denotes the mole fraction; a and b are the attraction and repulsion parameters, respectively; n_c is the number of components; and A_i stands for the active association site. g signifies the hard sphere radial distribution function (RDF) and X_{Ai} represents the fraction of site A on component i that does not form association with other sites, as defined below:

$$\mathrm{g} \approx \frac{2-\eta}{2(1-\eta)^3} \quad \text{where } \eta = \frac{b}{4v} \tag{2-16}$$

$$\mathrm{X_{Ai}} = \frac{1}{1 + \Sigma_{j=1}^{n_c} \sum_{k=A,B,\ldots} \rho x_j X_{kj} \Delta_{Ai}^{kj}} \tag{2-17}$$

in which, $\rho = 1/v$ refers to the density and Δ_{Ai}^{kj} denotes the self-association strength between sites A and B, as expressed below:

$$\Delta_{Ai}^{kj} = g\left[\exp\left(\frac{\epsilon^{A_i K_i}}{RT}\right) - 1\right] b_{ij} \beta^{A_i K_i} \tag{2-18}$$

$$\mathrm{b_{ij}} = \frac{b_i+b_j}{2} \tag{2-19}$$

in which, $\epsilon^{A_iK_i}$ and $\beta^{A_iK_i}$ introduce the self-association energy and bonding volume parameters, respectively. The association term in Equation (2-15) is derived by Michelsen and Hendriks [65] and Hendriks et al. [66] to accelerate the computational process. In this study, we use the four-site model (4C) (see panel a of Figure 2-3), which can generate reliable results for highly hydrogen bonded substances such as water and glycol [6]. Two A sites are for two oxygen lone pairs and two B sites belong to two hydrogen atoms. According to Huang and Radosz, alcohols can be modeled by two-site scheme (2B): one site for both oxygen lone pairs and one for the hydrogen atom, as depicted in Figure 2-3 b [67].

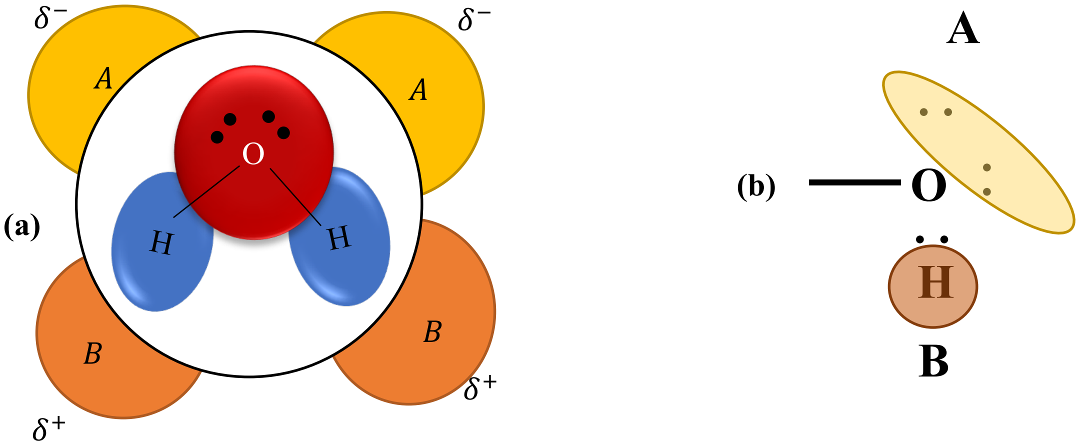

Figure 2-3: Simple sketch of (a) A four- site model (4C) of water molecules and (b) A two-site model (2B) of alcohols.

Based on the literature, the attraction, repulsion parameters, and universal gas constant of CPA EOS are generally kept at $a = 2/49$, $b = 2/21$, and $R = 1$, respectively, in the lattice units [52, 55]. However, the reduced properties should be the same, while the units are used based on the law of corresponding states. Therefore, the critical properties of the fluid should be updated based on the parameters selected for CPA EOS in the lattice units. For a single component system, the critical condition is defined as follows [6]:

$$\frac{dP}{dv}|_{T=T_c} = 0 \tag{2-20}$$

and

$$\frac{d^2P}{dv^2}|_{T=T_c} = 0 \tag{2-21}$$

where T_c represents the critical temperature. The explicit form of the first and second derivations of pressure is obtained by the MAPLE software [68]. The nonlinear system of equations (e.g., Equations (2-20) and (2-21)) is solved by a MATLAB intrinsic solver (e.g., *fzero*). Initial guesses are selected based on the roots of the PR EOS [69]. When the critical properties are calculated, the reduced properties can be determined in the lattice units. Thus, it is possible to make a comparison between the experimental data and results of CPA EOA in the lattice units. To determine the association parameters, the experimental data of coexistence densities and saturation pressures are used (see Figure 2-5). Coexistence densities are calculated based on the Maxwell construction (see Appendix A). The objective function is defined as follows:

$$F = R_{squared}\left(P_r^{sat^{exp}}, P_r^{sat^{cal}}\right) + R_{squared}(\rho_r^{sat^{exp}}, \rho_r^{sat^{cal}}) \tag{2-22}$$

in which, superscripts sat, exp, and cal denote the saturation condition, experimental data, and calculated results, respectively. A global search optimization is performed to determine the self-association energy (ϵ) and bonding volume (β) parameters.

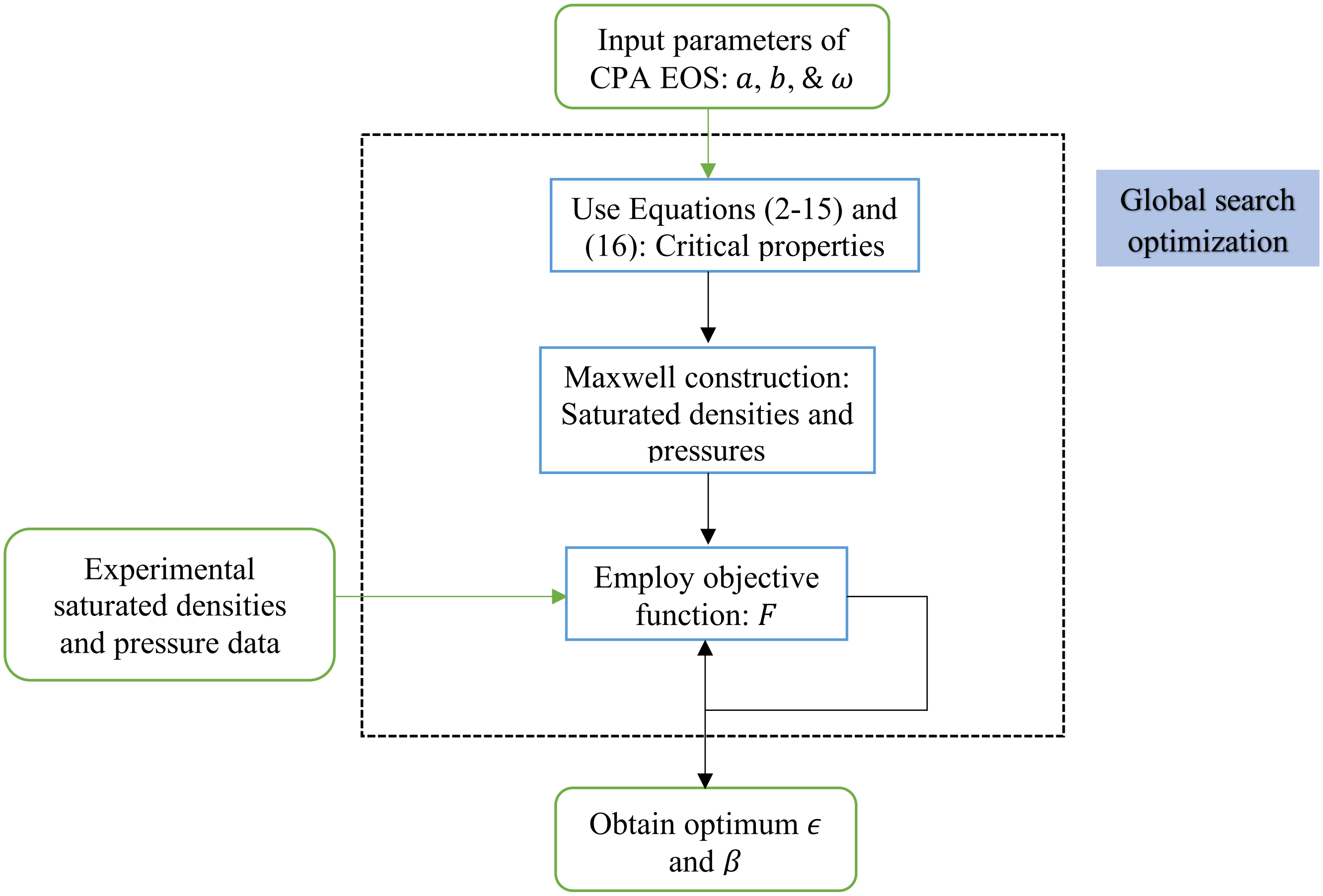

Figure 2-4: Workflow for association parameters optimization.

The global search optimization method is selected to avoid being stuck in probable local optimum points. More details about the global search optimization are provided by Ugray et al. [70].

Customized CPA EOS. Generally, the highest numerical errors happen within the sharp reigns of the interfaces, which fall in the unstable branch of the EOS where $\left(\frac{\partial p}{\partial v}\right)_T > 0$ (e.g., between the spinodal points). The unstable branch can be modified as it is experimentally unapproachable. As Colosqui et al. reported, increasing the slope of the unstable branch increases the internal forces towards the liquid side of spinodal and decreases the internal forces towards the vapor zone [71].

However, their proposed piecewise linear EOS had a discontinuity in the first derivative, which is a serious flaw in the numerical discretization [71]. In this study, we propose a new perturbation in the unstable branch, which meets the continuity of the first derivative and increases the slope at the same time, as expressed below:

$$P_{\boldsymbol{Customized}} = P_{CPA} + \delta P \tag{2-23}$$

where δP is a first derivative continuous function as follows:

$$\delta P = \begin{cases} 0 & if\ v < v_l \\ \kappa\left(\sin\left(\frac{\pi(v-v_l)}{L_1}+\frac{3\pi}{2}\right)+1\right) & if\ v_l < v < v_M \\ \kappa\left(\sin\left(\frac{\pi(v-v_l)}{L_2}+\frac{\pi}{2}\right)+1\right) & if\ v_M < v < v_g \\ 0 & if\ v_g < v \end{cases} \tag{2-24}$$

In Equation (2-24), $v_m = v_g - \alpha(v_g - v_l)$. v_l and v_g stand for the spinodal molar volumes on the liquid and gas sides, respectively. The perturbation is determined by a pair of (α, κ) uniquely.

Numerical modeling setup. In this part, the numerical setup is explained, and a new convergence condition is introduced. A 100×100 lattice and periodical boundary conditions are used in the numerical bubble tests to study the single component multiphase (SCMP) LBM. First, a droplet with a radius of $R_{ini} = 30$ is placed at the center of the domain. Inside the droplet is the liquid phase and the vapor phase is placed outside the droplet. The initial densities are selected based on the Maxwell construction results (see Appendix A). The initial density distribution is defined by the following function:

$$\rho(x,y) = \frac{\rho_{liquid} + \rho_{gas}}{2} - \frac{\rho_{liquid} - \rho_{gas}}{2}\left[\tanh\left(\frac{2\sqrt{(x-x_1)^2 - (y-y_1)^2} - R_0}{w}\right)\right] \quad (2\text{-}25)$$

In Equation (2-25), w introduces the initial interface thickness and R_0 refers to the initial radius. Each test is continued until the steady state condition is established. The maximum magnitude of spurious velocity, $|u^s|_{max}$, is selected as the convergence condition to ensure that the steady state condition is reached. As shown in Figure 2-5, the spurious current exhibits high fluctuations. The simulation is performed at $T_r = 0.8$, where the calculated gas and liquid densities by Maxwell construction are$\rho_{gas} = 0.2327$ and $\rho_{liquid} = 7.3347$, respectively. Yuan and Scheafer performed all runs up to 30000 time steps when the relative difference of spurious velocity at the time step t and $t - 1000$ is less than 10^{-6} [55]. Huang et al. proposed a convergence criterion by evaluating the relative difference of the entire domain velocity between 2000 time steps [72]. In this study, the relative difference of $|u^s_{max}|$ is calculated every 100 time steps to avoid unnecessary computational process/calculations and local extremums (due to the highly fluctuation behaviours at the maximum magnitude of the spurious velocity). When the maximum spurious velocity becomes on the order of 10^{-6} for more than 10 times constantly, the system is assumed to be at the equilibrium state. The animations of density and pressure variations during different time steps can visualize and identify this specific condition.

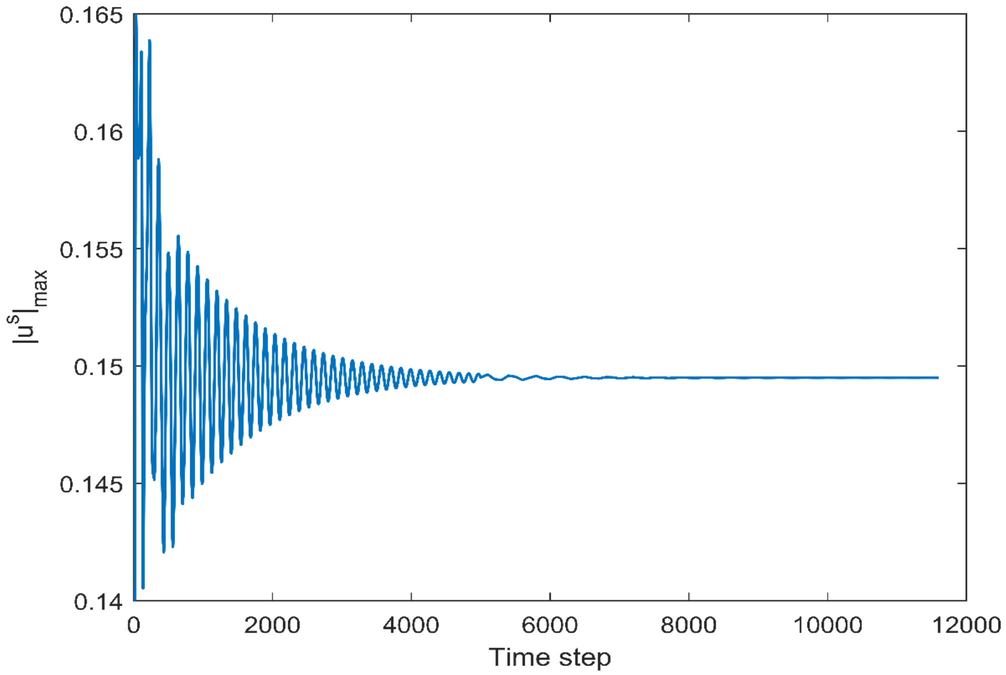

Figure 2-5: Fluctuations of the maximum spurious velocity at different time steps.

2.3 LIMITATIONS

The proposed single-relaxation time collision (BGK) is appropriate for low Reynolds number (particularly stationary) cases. To extend the model to high Reynolds number conditions, the multi-relaxation time (MRT) collision scheme is proposed [73, 74].

In the CPA EOS, it is assumed that the activity of each bonding site is independent of other bonding sites in the molecule, implying negligence of the steric hindrance and cooperativity effects. The polarity and quadrupolar interactions are also disregarded in the proposed model [75, 76].

2.4 RESULTS AND DISCUSSION

In this section, the consistency of the CPA EOS case is examined. Simulation outputs of the CPA and PR EOSs are presented and then a comparison between the modeling results and real saturation data is made. The Li et al.'s forcing scheme is employed to achieve an improvement in thermodynamic consistency and spurious velocity distribution. The discrete gradient operator with a higher isotropic order is used to lower the spurious velocity, while the modified CPA EOS is implemented to determine the initial density.

The effectiveness/reliability of the proposed model is assessed by comparison of the LBM simulation results with the outputs of the Maxwell construction approach. Figure 2-6 illustrates the coexistence density/reduced temperature curves attained from the Maxwell construction and the LBM simulations when utilizing the CPA EOS. As it is clear from Figure 2-6, an acceptable match is achieved for the liquid branch, however the difference between the LBM and Maxwell construction results is noticeable for the gas phase.

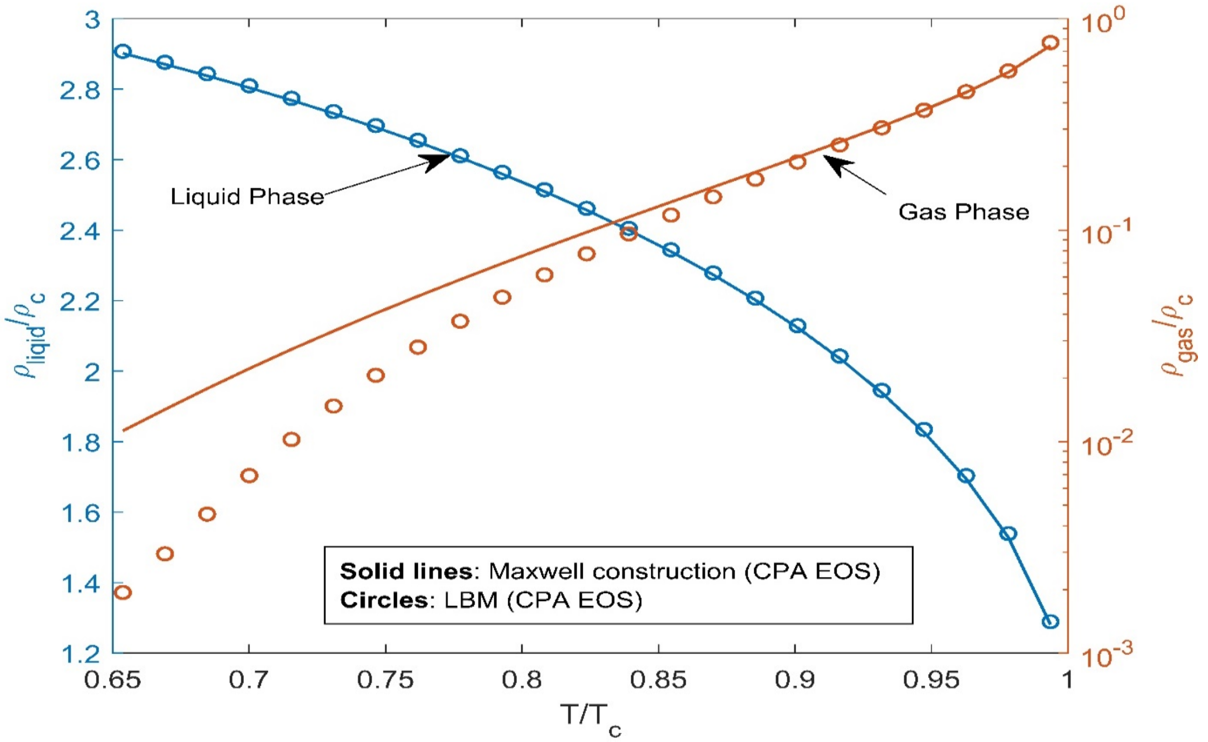

Figure 2-6: Comparison of coexistence curves based on LBM simulations and Maxwell construction.

To explain this considerable deviation, the gas branch is simulated based on both CPA and PR EOSs as shown in Figure 2-7 in the semi log-scale where the LBM and Maxwell construction strategies are employed. According to Figure 2-7, the difference between the PR/LBM and CPA/LBM cases will increase as the temperature decreases. As expected, such a deviation is not observed for the PR and CPA EOSs while using the Maxwell construction. The relative errors ($|\rho_{LBM} - \rho_{Mc}|/\rho_{Mc}$), where ρ_{LBM} and ρ_{Mc} are the gas density calculated from the LBM simulation and Maxwell construction, are 3.3612% and 4.4223% at $T_r = 0.65$ for the gas phase modeled by CPA and PR EOSs, respectively. The difference between the mechanical stable results (e.g., LBM results) and thermodynamically stable results (e.g., Maxwell results) for the gas phase is due to the curved interface of the droplet and/or additional term which is introduced into the macroscopic equations when the velocity shift (or Shan-Chen) forcing scheme is used. Li et al. showed that ϵ in Equation (2-12) should be between $\epsilon=1$ and $\epsilon=2$ to obtain a better agreement with the Maxwell construction [1].

Thus, the thermodynamic inconsistency is tackled through different approaches such as multi-pseudopotential interaction (MPI) [52, 53] and improved force scheme in multi-relaxation time (MRT) LBM to enhance the model reliability [73, 77]. The self tuning EOS is also employed to achieve more stable results [71, 78].

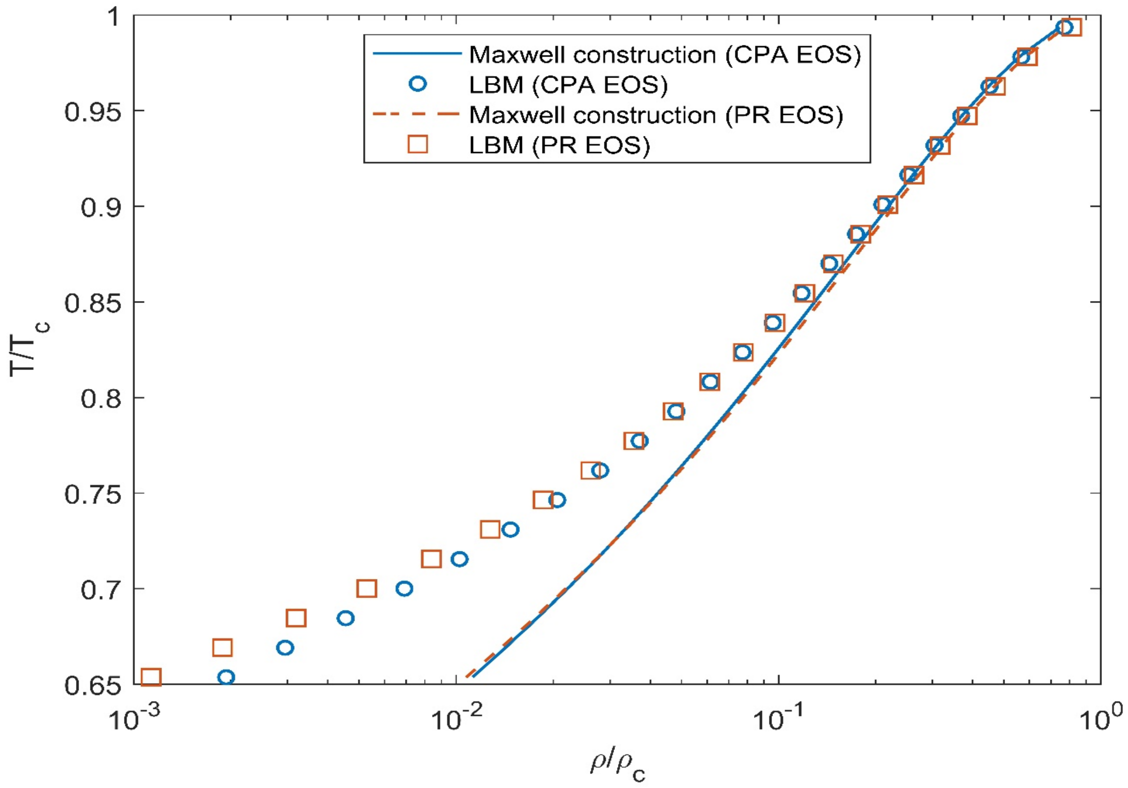

Figure 2-7: Comparison between the reduced densities of the gas phase of the coexistence phases determined from the LBM simulation and Maxwell construction when PR and CPA EOSs are employed.

Through implementation of the Li et al. forcing scheme, it is expected to improve the thermodynamic consistency. Figure 2-8 illustrates the thermodynamic consistency of the LBM method when CPA EOS is utilized with $\sigma' = 0.2885$ (see Equation (2-13)). As seen in Figure 2-8, there is a very good match between the LBM and Maxwell construction outputs. In addition, the thermodynamic consistency in the gas phase is improved considerably. However, a small deviation in the liquid phase is noticed. The association parameters of CPA EOS (e.g., $\epsilon^{A_iK_i}$ and $\beta^{A_iK_i}$) are selected to attain a good match with the experimental data while employing the velocity shifting forcing scheme. Therefore, the thermodynamic consistency in liquid phase might decrease slightly when the magnitude of σ' is increased to improve the thermodynamic consistency in the gas phase. Hence, the parameter σ' is used in the Li et al. forcing scheme to modify the intraction properties. Li et al. proved that the model will be unstable when $\sigma' = 0$ (e.g., the Guo et al.'s forcing scheme), due to the high thermodynamic inconsistency.

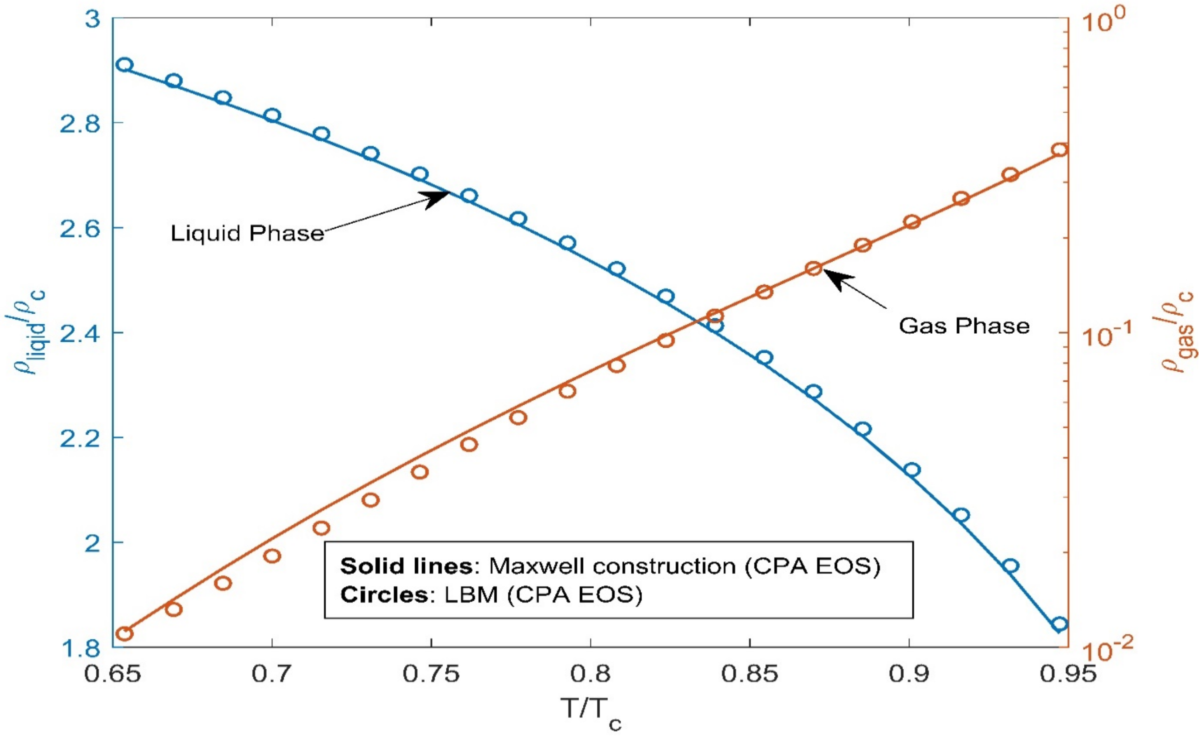

Figure 2-8: Reduced density of both liquid and gas phases versus reduced temperature based on LBM simulations and Maxwell construction when the Li et al.'s forcing scheme is employed (comparing to Figure 2-6, only forcing scheme is changed).

The numerical stability of the integrated CPA / LBM model can be evaluated based on the maximum magnitude of the spurious velocity, $|u^s|_{max}$. Figure 2-9 compares the $|u^s|_{max}$ trends for both CPA/LBM and PR/LBM cases at different reduced temperatures (panel a of Figure 2-9) and density ratios (panel b of Figure 2-9). According to Figure 2-9, the value of the spurious velocity is increased with decreasing the reduced temperature for both CPA and PR EOSs. The lower density ratio does not reveal the lower capability of the CPA/LBM approach that might be due to the higher density in the gas phase (see Figure 2-7). The maximum magnitude of spurious velocity is not changed considerably when the implemented EOS is switched from PR to CPA, since the extent of spurious velocity is mainly affected by the order of isotopy in the gradient operator and the forcing scheme.

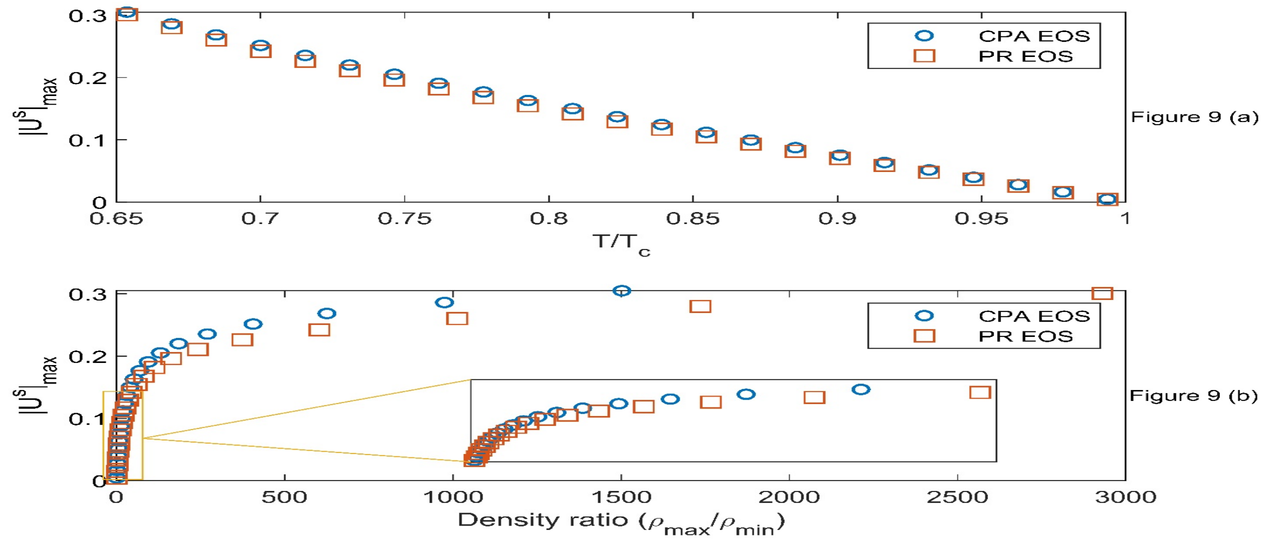

Figure 2-9: Variation of the maximum magnitude of spurious velocity with: (a) reduced temperature and (b) density ratio for the CPA and PR EOSs.

It should be noted that the results shown in Figure 2-9 are based on the SC forcing scheme (known as the velocity shift method). To elaborate the impact of the forcing scheme, the contour map and velocity field of a static droplet are depicted in Figure 2-10 for both Li et al. and SC forcing schemes when $T/T_c = 0.9$ and $\tau = 1$.

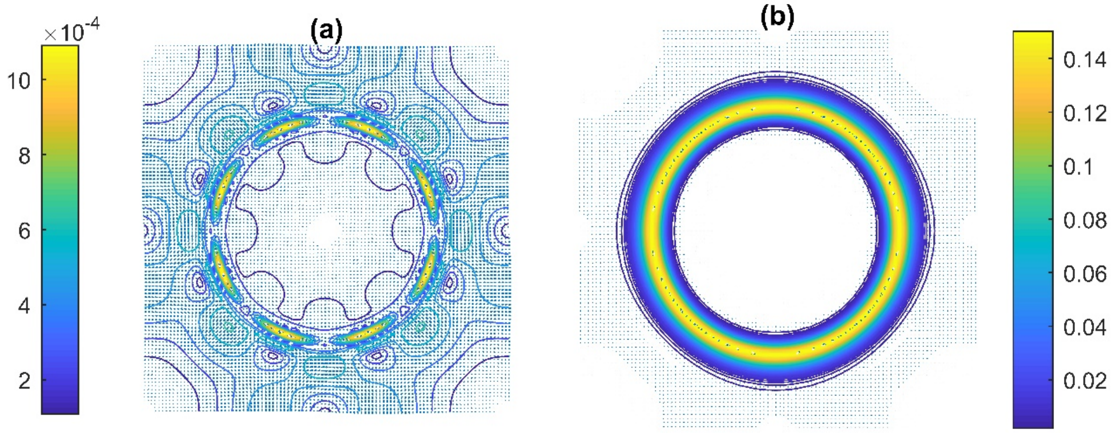

Figure 2-10: Velocity field and contour for a static droplet on the basis of a) Li et al. and b) SC forcing schemes.

As shown in Figure 2-10, the Li et al.'s forcing scheme exhibits lower spurious velocities. Based on the velosity contour profile, the velocity distribution patterns are also different for these two different forcing schemes, implying that the Li et al.'s forcing scheme is able to better demonstrate the flow behaviours obtained from the Navier-Stokes equations, compared to the SC forcing scheme. Hence, it appears to be a better representation of the isotopy in the LBM discrete gradient operator.

To examine the capability of the CPA /LBM strategy to model the real data, a comparison between the experimental data of water and simulation results is made. Figure 2-11 presents the results of the CPA/ LBM simulations for estimation of the liquid phase density, where the SC forcing scheme is employed. As illustrated in Figure 2-11, the CPA EOS offers a greater precision for both phases, compared to the PR EOS case. Table 2-1 presents a comparison of the results obtained from both CPA and PR EOSs. According to Table 2-1, CPA has a lower error percentage (e.g., minimum error, maximum error, and mean squared error), compared to PR. As the parameters for the association part of the CPA EOS (e.g., ϵ and β) approach zero, the results of the CPA EOS become closer to the PR EOS simulation outputs. Therefore, it is vital to determine the associating parameters in the lattice units with a high accuracy to attain reliable trends/outcome. As explained in the methodology section, the association parameters for water in the lattice units are $\epsilon = 0.1636$ and $\beta = 0.0973$. Table 2-2 summarizes the self-association energy and bonding volume parameters for five associating fluids including water, methanol, ethanol, 1-propanol, and 1-butanol. It is worth noting that the global search optimization is chosen to avoid the local optima, though the initial guesses might still affect the final optimal points.

Table 2-1: Error comparison of CPA and PR results of LBM simulation.

EOS	Max error (%)	Min error (%)	Mean squared error
CPA	76.0435	0.0169	0.0030
PR	87.8518	0.0546	0.0355

Table 2-2: Associating parameters in the lattice units suggested for water and normal alcohols (from methanol to 1- butanol) while implementing the global search optimization [a=2/49, b=2/21, and R=1].

Compound	ω	ϵ^{AB}	β	$R_{squared}$
Water	0.344	0.1636	0.09730	0.9992
Methanol	0.565	0.5638	0.0733	0.9984
Ethanol	0.643	0.6086	0.0727	0.9979
1-Propanol	0.620	0.5324	0.0877	0.9984
1-Butanol	0.588	0.5994	0.0828	0.9988

Li et al. concluded that a lower value for the attraction parameter in EOS (a) results in a greater stability at lower reduced temperatures [73]. Therefore, the CPA EOS association parameters are listed in Table 2-3 for lower values of the attraction parameter. As mentioned earlier, the 4C and 2B bonding schemes are employed for water and alcohols, respectively.

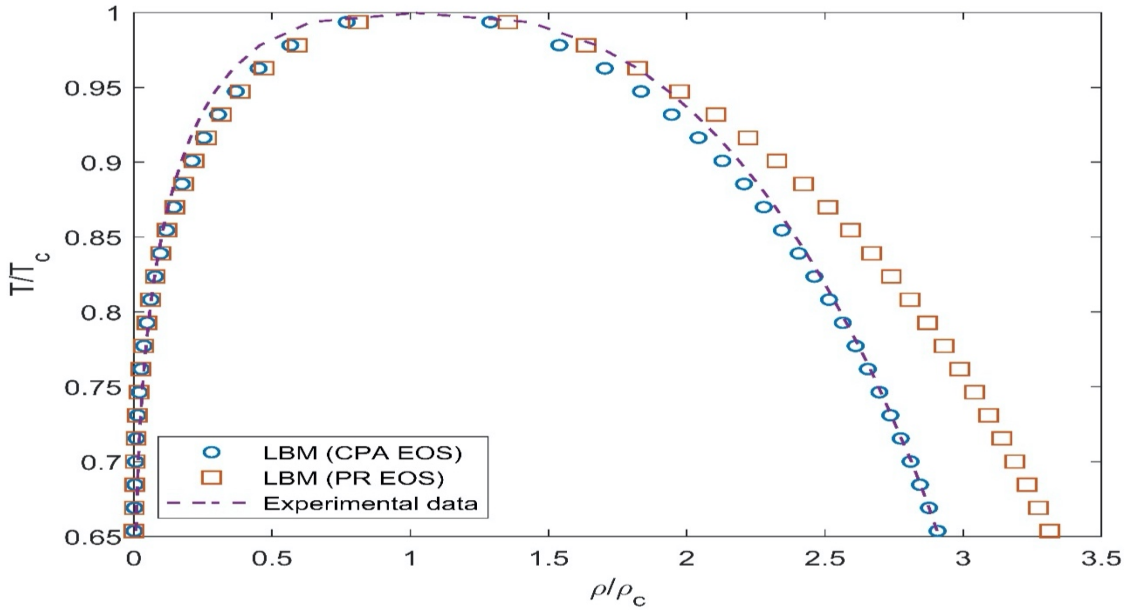

Figure 2-11: Comparison of the values of saturated water density obtained from experiments and LBM strategy based on CPA and PR EOSs.

Table 2-3: Associating parameters in the lattice units for pure compounds such as water and normal alcohols (from methanol to 1- butanol) using the global search optimization when b=2/21 and R=1.

Compound	$a = 1/49$			$a = 1/98$		
	ϵ^{AB}	β	$R_{squared}$	ϵ^{AB}	β	$R_{squared}$
Water	0.0819	0.0972	0.9992	0.0433	0.0854	0.9992
Methanol	0.3795	0.0505	0.9983	0.2526	0.0372	0.9983
Ethanol	0.3730	0.0569	0.9979	0.2561	0.0401	0.9979
1-Propanol	0.3966	0.0538	0.9983	0.2498	0.0419	0.9983
1-Butanol	0.4247	0.0537	0.9987	0.2522	0.0451	0.9987

Up to now, all LBM results have been obtained based on the 4th order isotropy of the discrete gradient operator. As it is known, increasing the isotropy leads to a decrease in the spurious velocity [49, 50]. Our plan is to investigate the impact of isotropic order of the discrete gradient operator up to 8th order on the simulation outputs. It was found that the system becomes unstable due to low interfacial tention at low reduced temperature and/or high density ratio conditions. Therefore, an extended version of the CPA EOS is used to determine the initial density distribution. Figure 2-12 presents the LBM results using 8th order of isotropy. To obtain the initial density distribution funcrion, (80,0.5) is selected as the pair of input parameters of the extended CPA EOS. The Li et al.'s forcing scheme is applied to improve the thermodynamic consistency. Considering the same input parameter of the extended model for the entire temperature interval can cause high computational costs. Additionally, assuming the same σ' as an input parameter for the Li et al.'s forcing scheme within a broad interval of the reduced temperature leads to an appreciable departure from the Maxwell equal area construction (see Figure 2-12). Hence, a smart method can be utilized to choose a suitable pair input parameter for the extended CPA EOS,(α, κ), and the input parameter of Li et al.'s forcing scheme at each tempereture. Such a strategy can decrease the computational costs and improve the thermodynamic consistency.

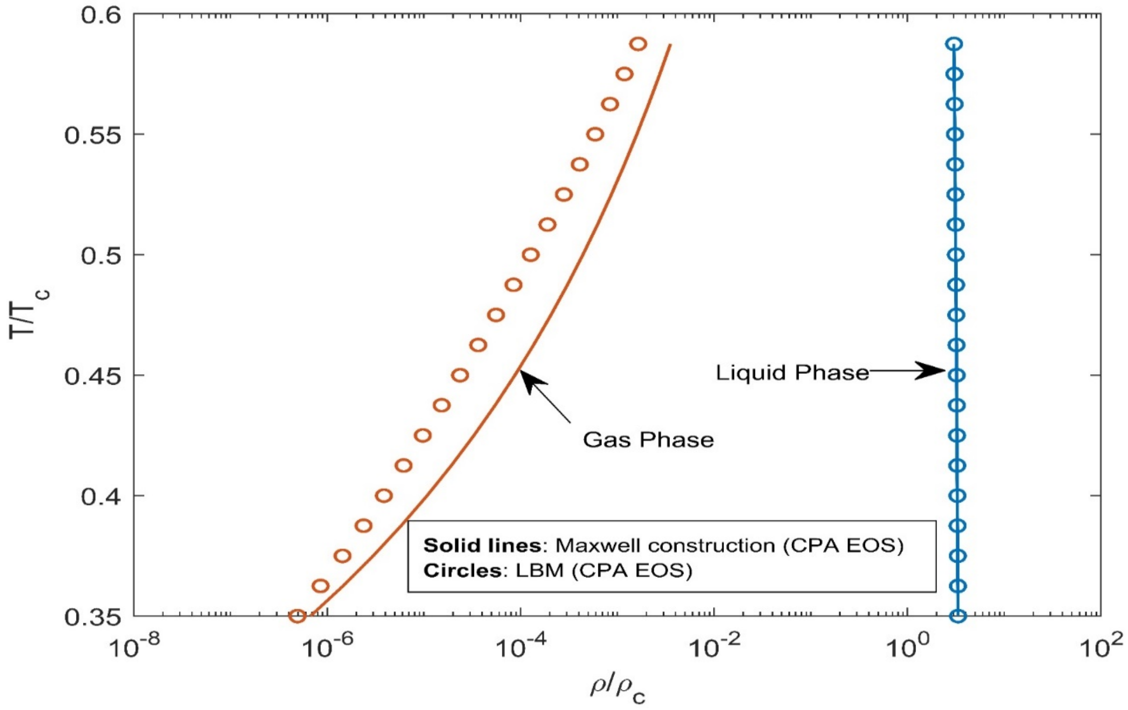

Figure 2-12: Coexistence curves results of the LBM simulation and Maxwell equal area construction with 8th order of isotropy in the discrete gradient operator.

To study the capillary effect, the simulation runs need to be conducted at different droplet radii. The slope of differential pressure between the gas and liquid phases (e.g., capillary pressure) versus the inverse of the radius is then related to the interfacial tension (see Equation (A-6)). Figure 2-13 illustrates the variations of the capillary pressure with the inverse of the droplet radius for water at $T_r = 0.7929$. The interfacial tension can be tuned by including the multi-range potential in the improved forcing term of MRT LBM [79, 80]. The influence of droplet size can be minimized by the use of self-tuning equation of state [71]. Li and Luo concluded that the droplet size impact on the gas phase density can be reduced by increasing the slope of EOS in the vapor phase [78].

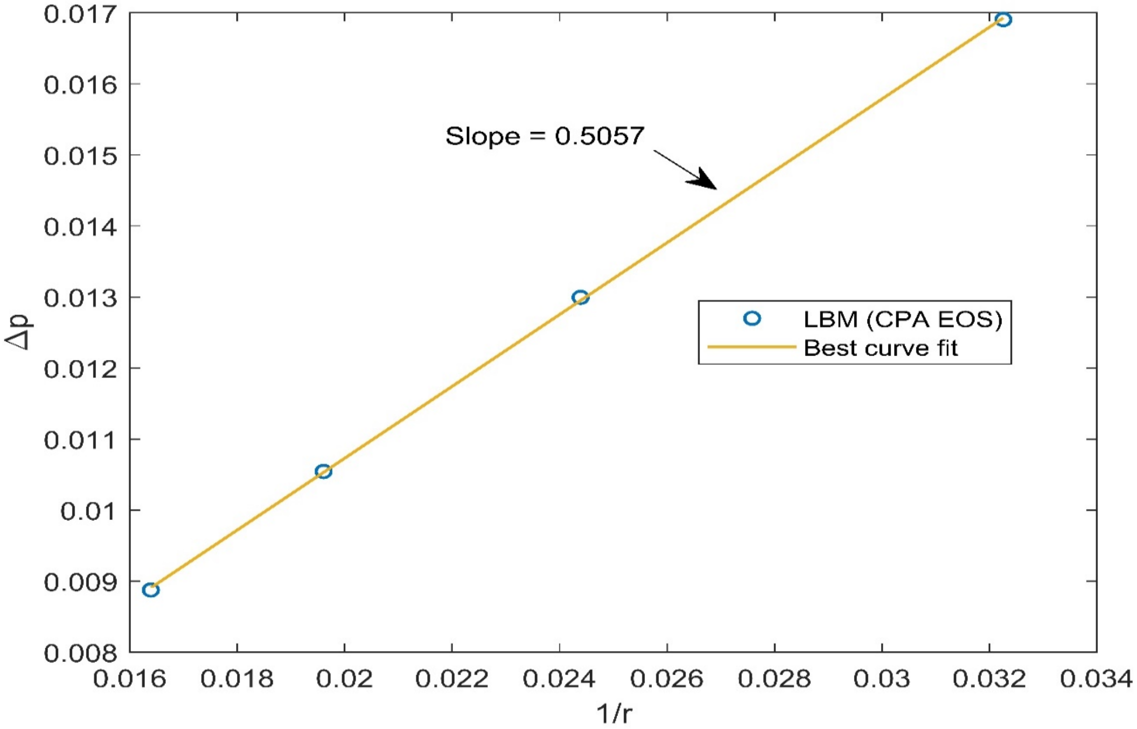

Figure 2-13: The pressure difference (Δp) against $1/r$ for water at $T_r = 0.7929$.

The same procedure is followed at different reduced temperatures to figure out the trend/behaviours of the interfacial tension, σ, with temperature. The interfacial tension of water versus reduced temperature is shown in Figure 2-14. As it is clear, the interfacial tension results attained from LBM simulations follow the same trend/behaviours as the measured values (real data). Due to the implemented single range pseudo-potential approach in the current study, the interfacial tension cannot be tuned. To address this limitation, multi-range pseudo-potential is introduced [81-83].

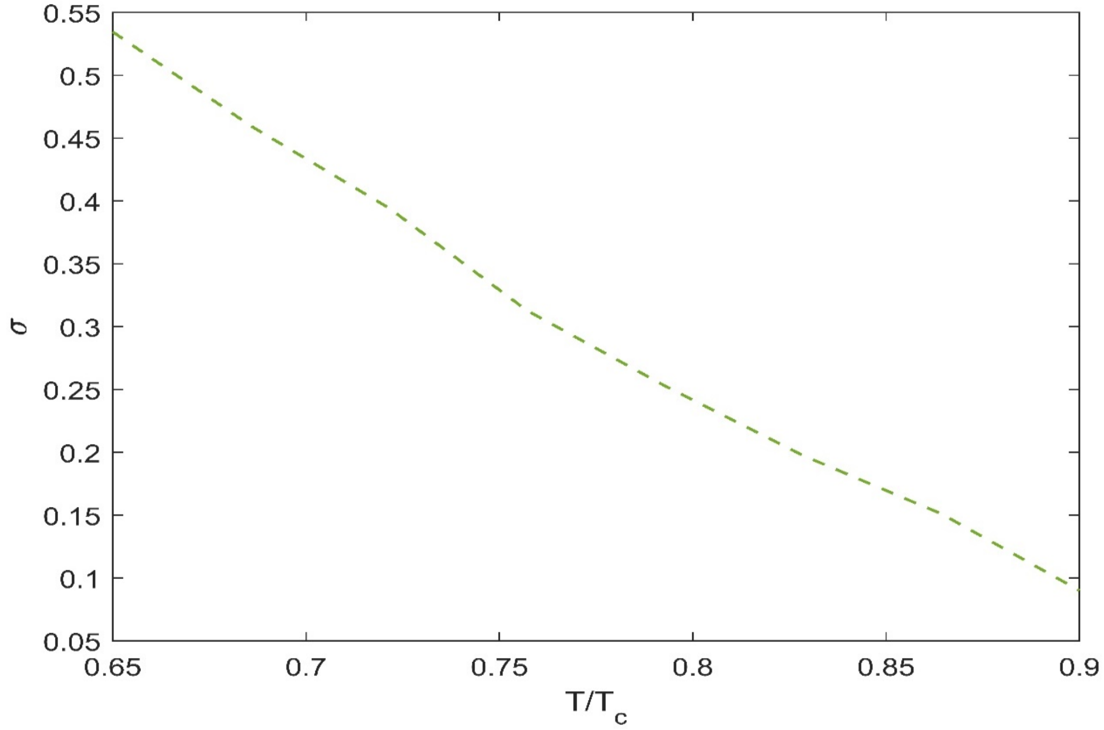

Figure 2-14: Interfacial tension trend versus the reduced temperature in the lattice units for water.

Associating fluids play a crucial rule in different processes/phenomena such as biological processes [84], oil production/recovery from hydrocarbon reservoirs [20], energy systems, and chemical production. Therefore, development of a reliable LBM approach to simulate the thermodynamic characteristics of associating fluids seems vital to better design and operate the corresponding processes. The methodology proposed in this research work is appropriate for static problems by using the BGK collision scheme. MRT collision scheme can be an appropriate alternative to extend this approach to the cases at high Reynolds number conditions. Also, the cascaded model can be used to improve the ability of the LBM for fluid flow and thermal transport modeling. The cascaded, which is also known as the central-moment-based lattice Boltzmann method (CLBM), is proposed to tackle the numerical instability in the zero-viscosity limit. This generally happens by an insufficient degree of Galilean invariance of the relaxation-type lattice Boltzmann collision operation [85].

2.5 CONCLUSIONS

Some fluids associate due to the hydrogen bonding. This association results in unusual thermodynamic behaviors. In this research work, the CPA EOS is included in the LBM to model the thermodynamic behaviors of this type of fluids. The method accuracy is verified with the Maxwell construction approach and experimental data. The main conclusions drawn based on the study results are listed below:

- A more reliable stability condition is proposed to decrease the computational costs. Furthermore, a better thermodynamic consistency in the gas phase is attained by implementing the CPA EOS in the LBM.
- A new approach based on the global search optimization method is developed to determine the association parameters in the lattice units for water and primary alcohols (e.g., methanol and 1-butanol).
- There is a very good agreement between the CPA/LBM results and experimental data, while the PR/LBM case is not able to simulate the real thermodynamic behaviours with an acceptable accuracy.
- The thermodynamic consistency is enhanced by employing the Li et al.'s forcing scheme. It is also possible to maintain the stability and thermodynamic consistency at low reduced temperatures through using higher order of isotropy in the gradient operator.

- An extended version of CPA EOS is introduced to determine the initial density distribution, making the computation faster and more reliable.
- The interfacial tension of water as a function of the reduced temperature is acceptably simulated with the CPA/LBM approach.

ACKNOWLEDGEMENTS

The authors wish to acknowledge the support of Memorial University, Canada; the Natural Sciences and Engineering Research Council of Canada (NSERC); InnovateNL; and Equinor (formerly Statoil Canada).

APPENDIX A2: MAXWELL CONSTRUCTION AND COMPUTATION ALGORITHM

The equality of the Gibbs free energy at the saturation point for a droplet is expressed as follows:

$$G^l = G^g \tag{A2-1}$$

$$A^l + P^l v^l = A^g + P^g v^g \tag{A2-2}$$

where G and A represent the Gibbs and Helmholtz free energies, respectively. For flat interfaces, both pressures in the liquid and gas phase are equal to the saturation pressure, as shown below:

$$P^l = P^g = P^{sat} \tag{A2-3}$$

Since dT=0 (isotherm condition) at the equilibrium, we can write the following equation:

$$A^g - A^l = -\int P dv \tag{A2-4}$$

Using Equations (A-2) to (A-4), the saturation coexistence densities can be calculated through using the following equation:

$$-\int_{v_l}^{vg} P dv = -P^{sat}(v^l - v^g) \qquad \text{(A2-5)}$$

To calculate the coexistence volumes/densities, first an initial saturation pressure is guessed. Based on the initial guess, the liquid and gas volumes/densities are calculated using an EOS. If the left-hand side (LHS) is more than the right-hand side (RHS), the pressure for the next loop should be increased to obtain the correct value; otherwise, it should be decreased. This loop will be repeated until the relative differences between two loops are very small (10^{-10}).

The guessed initial pressure should be between the spinodal points where $\frac{dP}{dv} = 0$. Due to the nonlinearity of the CPA EOS, the first spinodal point (e.g., with a lower volume) is determined by finding the global minimum of CPA EOS. Searching the global minimum is started from the repulsion parameter (e.g., b in Equation (2-14)). The second spinodal point, which has a higher volume than the first spinodal point, is then determined through finding the global maximum point. Searching the global maximum is also commenced from the first spinodal point. The *fminsearch* and *fminbnd* MATLAB functions are utilized to determine the minimum and maximum spinodal points, respectively. To obtain the roots of CPA EOS, a MATLAB intrinsic solver (e.g., *fsolve*) is employed [69]. The initial guesses for the CPA EOS roots are chosen based on the roots of the PR EOS. The procedure on the Maxwell construction is demonstrated in Figure A2-1.

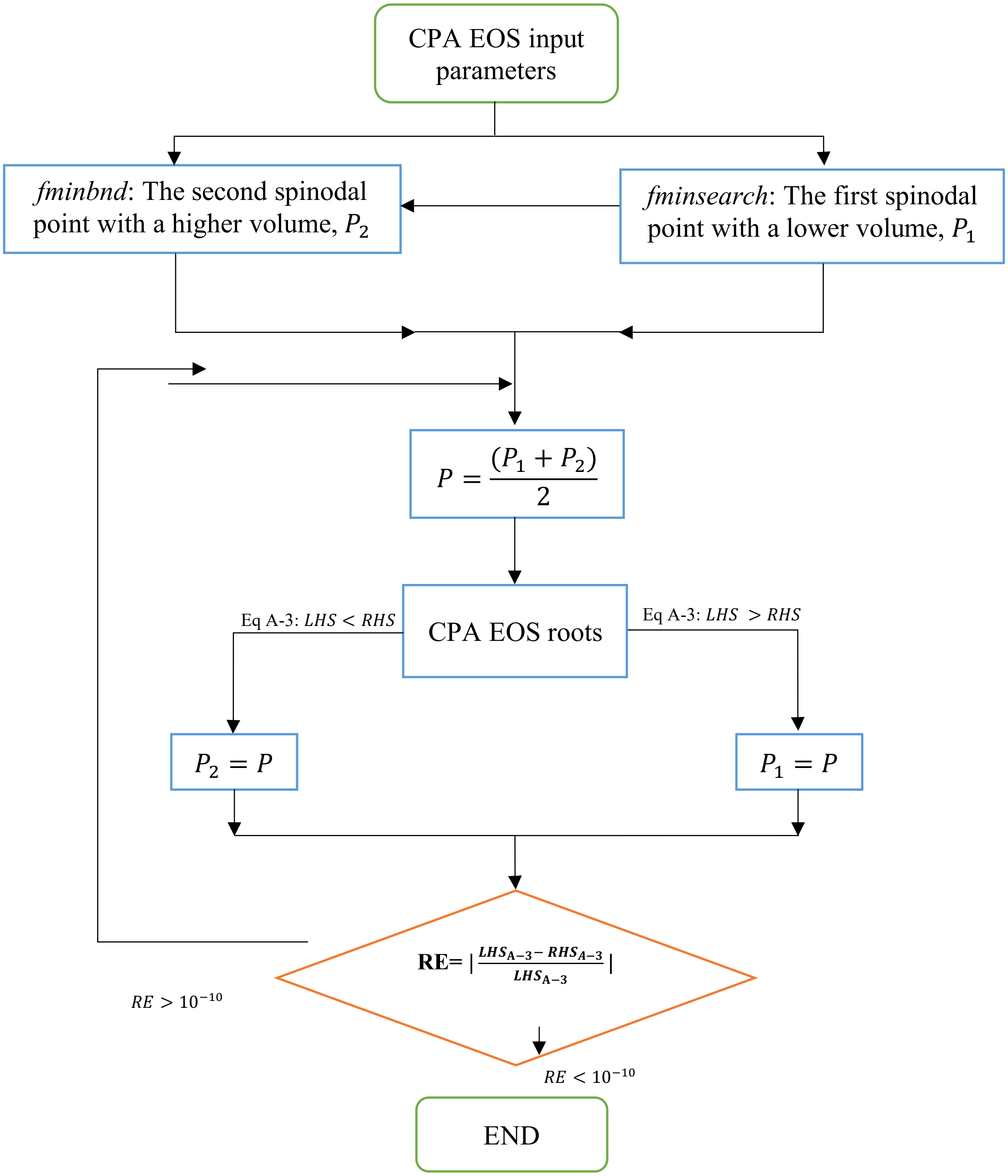

Figure A2-1: Work flow Maxwell construction while utilizing CPA EOS [RE stands for the relative error].

When the interface between two phases are curved, the Young-Laplace equation of capillarity provides the mechanical equilibrium for a droplet, as given below [86]:

$$P^l - P^g = P_c = \frac{2\sigma}{r} \tag{A2-6}$$

in which, P_c is the capillary pressure; P^l is the liquid pressure; P^g introduces the gas pressure; σ refers to the interfacial tension; and r stands for the radius of the droplet.

NOMENCLATURES

Acronyms

BGK = Bhatnagar−Gross−Krook
CFD = Computational Fluid Dynamic
CPA = Cubic-Plus-Association
DNS = Direct Numerical Simulation
DPD = Dissipative Particle Dynamic
DSMC = Direct Simulation Monte Carlo
EDM = Exact Difference Method
EOS = Equation of State
LBE = Lattice Boltzmann Equation
LBM = Lattice Boltzmann Method
LES = Large Eddy Simulation
LHS = Left-Hand Side
MD = Molecular Dynamic
MRT = Multi-Relaxation Time

PC-SAFT = Perturbed-Chain Statistical Associating Fluid Theory

PDE = Partial Differential Equation

PR = Peng-Robinson

QMS = Quantum Molecular Simulation

RANS = Reynolds-Averaged Naiver-Stokes

RDF = Radial Distribution Function

RHS = Right-Hand Side

SCMP = Single Component Multiphase

SRK = Soave-Redlich-Kwong

Variables

a = Attraction parameter of EOS

$\beta^{A_iK_i}$ = Bonding volume

T_c = Critical temperature

$\boldsymbol{F}$ = Force

$f_i()$ = Density distribution function

τ = Dimensionless relaxation time

f_i^{eq} = Equilibrium distribution function

S_i = Forcing source

X_{Ai} = Fraction of site A on the component of i which did not form associate with other sites

G = Gibbs free energy

g = Hard sphere radial distribution function

A = Helmholtz free energy

$\boldsymbol{F}_{int}$ = Interparticle forces

v = Molar volume

$\boldsymbol{\nu}$ = Kinematic viscosity

$\mathbf{v}$ = Particle velocity

x = Mole fraction

$\mathbf{x}$ = Spatial coordination

n_c = Number of components

e_i = Particle discretized velocity vector

P = Pressure

P_b = Bulk pressure

r = Radius of droplet

b = Repulsion parameter of EOS

C_s = Speed of sound

e^4 = Fourth-order tensor associated with weights

T = Temperature

t = Time

R = Universal gas constant

R_0 = Initial radius

G = Interparticle strength

Greek symbols/variables

β = Bonding volume

φ = Effective mass

σ = Interfacial tension

ϑ = Kinematic viscosity

δ_x = Lattice spacing

δ_t = Lattice time step

ρ = Molar density

$\epsilon^{A_iK_i}$ = Self-association energy

Δ_{Ai}^{kj} = Self-association strength between site A and B

ω_i = Weight factors

Ω = Collision term

ψ = Interaction potential

Superscripts

eq = Equilibrium

s = Spurious

Subscripts

A_i = Active association site

int = Interparticle

REFERENCES

1. Li, Q., et al., *Lattice Boltzmann methods for multiphase flow and phase-change heat transfer.* Progress in Energy and Combustion Science, 2016. **52**: p. 62-105.
2. Vanson, J.-M., et al., *Kinetic Accessibility of Porous Material Adsorption Sites Studied through the Lattice Boltzmann Method.* Langmuir, 2017. **33**(6): p. 1405-1411.

3. Peng, D.-Y. and D.B. Robinson, *A new two-constant equation of state.* Industrial & Engineering Chemistry Fundamentals, 1976. **15**(1): p. 59-64.

4. Soave, G., *Equilibrium constants from a modified Redlich-Kwong equation of state.* Chemical engineering science, 1972. **27**(6): p. 1197-1203.

5. Kontogeorgis, G.M., et al., *Ten years with the CPA (Cubic-Plus-Association) equation of state. Part 1. Pure compounds and self-associating systems.* Industrial & engineering chemistry research, 2006. **45**(14): p. 4855-4868.

6. Firoozabadi, A., *Thermodynamics and applications in hydrocarbon energy production*. 2016: McGraw-Hill Education New York.

7. Kontogeorgis, G.M., et al., *An equation of state for associating fluids.* Industrial & engineering chemistry research, 1996. **35**(11): p. 4310-4318.

8. Li, Z. and A. Firoozabadi, *Cubic-plus-association equation of state for water-containing mixtures: Is "cross association" necessary?* AIChE journal, 2009. **55**(7): p. 1803-1813.

9. Li, Z. and A. Firoozabadi, *Cubic-plus-association equation of state for asphaltene precipitation in live oils.* Energy & fuels, 2010. **24**(5): p. 2956-2963.

10. Li, Z. and A. Firoozabadi, *Modeling asphaltene precipitation by n-alkanes from heavy oils and bitumens using cubic-plus-association equation of state.* Energy & fuels, 2010. **24**(2): p. 1106-1113.

11. Kontogeorgis, G.M., et al., *Ten years with the CPA (Cubic-Plus-Association) equation of state. Part 2. Cross-associating and multicomponent systems.* Industrial & Engineering Chemistry Research, 2006. **45**(14): p. 4869-4878.

12. McNamara, G.R. and G. Zanetti, *Use of the Boltzmann equation to simulate lattice-gas automata.* Physical review letters, 1988. **61**(20): p. 2332.

13. Frisch, U., B. Hasslacher, and Y. Pomeau, *Lattice-gas automata for the Navier-Stokes equation.* Physical review letters, 1986. **56**(14): p. 1505.

14. Chen, S. and G.D. Doolen, *Lattice Boltzmann method for fluid flows.* Annual review of fluid mechanics, 1998. **30**(1): p. 329-364.

15. Gupta, N., E. Fathi, and F. Belyadi, *Effects of nano-pore wall confinements on rarefied gas dynamics in organic rich shale reservoirs.* Fuel, 2018. **220**: p. 120-129.

16. Tao, S. and Z. Guo, *Boundary condition for lattice Boltzmann modeling of microscale gas flows with curved walls in the slip regime.* Physical Review E, 2015. **91**(4): p. 043305.

17. Yang, L., et al., *Boundary conditions with adjustable slip length for the lattice Boltzmann simulation of liquid flow.* Computers & Fluids, 2018. **174**: p. 200-212.

18. Abadi, R.H.H., A. Fakhari, and M.H. Rahimian, *Numerical simulation of three-component multiphase flows at high density and viscosity ratios using lattice Boltzmann methods.* Physical Review E, 2018. **97**(3): p. 033312.

19. Chen, L., et al., *A critical review of the pseudopotential multiphase lattice Boltzmann model: Methods and applications.* International Journal of Heat and Mass Transfer, 2014. **76**: p. 210-236.

20. Liu, H., et al., *Multiphase lattice Boltzmann simulations for porous media applications.* Computational Geosciences, 2016. **20**(4): p. 777-805.

21. He, Y.-L., et al., *Lattice Boltzmann methods for single-phase and solid-liquid phase-change heat transfer in porous media: A review.* International Journal of Heat and Mass Transfer, 2019. **129**: p. 160-197.

22. Arabjamaloei, R. and D. Ruth, *Numerical study of inertial effects on permeability of porous media utilizing the Lattice Boltzmann Method.* Journal of Natural Gas Science and Engineering, 2017. **44**: p. 22-36.

23. Chai, Z., et al., *Non-Darcy flow in disordered porous media: A lattice Boltzmann study.* Computers & Fluids, 2010. **39**(10): p. 2069-2077.

24. Foroughi, S., S. Jamshidi, and M.R. Pishvaie, *New Correlative Models to Improve Prediction of Fracture Permeability and Inertial Resistance Coefficient.* Transport in Porous Media, 2018. **121**(3): p. 557-584.

25. Hasert, M., J. Bernsdorf, and S. Roller. *Lattice Boltzmann simulation of non-Darcy flow in porous media*. in *ICCS*. 2011.

26. Sukop, M.C., et al., *Evaluation of permeability and non-Darcy flow in vuggy macroporous limestone aquifer samples with lattice Boltzmann methods.* Water Resources Research, 2013. **49**(1): p. 216-230.

27. Chai, Z., et al., *Lattice Boltzmann model for high-order nonlinear partial differential equations.* Physical Review E, 2018. **97**(1): p. 013304.

28. Lai, H. and C. Ma, *A higher order lattice BGK model for simulating some nonlinear partial differential equations.* Science in China Series G: Physics, Mechanics and Astronomy, 2009. **52**(7): p. 1053-1061.

29. Shi, B. and Z. Guo, *Lattice Boltzmann model for nonlinear convection-diffusion equations.* Physical Review E, 2009. **79**(1): p. 016701.

30. Shi, B. and Z. Guo, *Lattice Boltzmann simulation of some nonlinear convection–diffusion equations.* Computers & Mathematics with Applications, 2011. **61**(12): p. 3443-3452.

31. Wang, H., et al., *Finite-difference lattice Boltzmann model for nonlinear convection-diffusion equations.* Applied Mathematics and Computation, 2017. **309**: p. 334-349.

32. Zhang, L., et al., *Consistent boundary conditions of the multiple-relaxation-time lattice Boltzmann method for convection–diffusion equations.* Computers & Fluids, 2018. **170**: p. 24-40.

33. Krüger, T., et al., *Numerical simulations of complex fluid-fluid interface dynamics.* The European Physical Journal Special Topics, 2013. **222**(1): p. 177-198.

34. Tryggvason, G., et al., *A front-tracking method for the computations of multiphase flow.* Journal of Computational Physics, 2001. **169**(2): p. 708-759.

35. Sethian, J.A. and P. Smereka, *Level set methods for fluid interfaces.* Annual review of fluid mechanics, 2003. **35**(1): p. 341-372.

36. Hirt, C.W. and B.D. Nichols, *Volume of fluid (VOF) method for the dynamics of free boundaries.* Journal of computational physics, 1981. **39**(1): p. 201-225.

37. Badalassi, V., H. Ceniceros, and S. Banerjee, *Computation of multiphase systems with phase field models.* Journal of Computational Physics, 2003. **190**(2): p. 371-397.

38. Gunstensen, A.K., et al., *Lattice Boltzmann model of immiscible fluids.* Physical Review A, 1991. **43**(8): p. 4320.

39. Rothman, D.H. and J.M. Keller, *Immiscible cellular-automaton fluids.* Journal of Statistical Physics, 1988. **52**(3-4): p. 1119-1127.

40. Swift, M.R., W. Osborn, and J. Yeomans, *Lattice Boltzmann simulation of nonideal fluids.* Physical review letters, 1995. **75**(5): p. 830.

41. He, X., S. Chen, and R. Zhang, *A lattice Boltzmann scheme for incompressible multiphase flow and its application in simulation of Rayleigh–Taylor instability.* Journal of Computational Physics, 1999. **152**(2): p. 642-663.

42. Shan, X. and H. Chen, *Lattice Boltzmann model for simulating flows with multiple phases and components.* Physical Review E, 1993. **47**(3): p. 1815.

43. Benzi, R., S. Succi, and M. Vergassola, *The lattice Boltzmann equation: theory and applications.* Physics Reports, 1992. **222**(3): p. 145-197.

44. Huang, H., M. Sukop, and X. Lu, *Multiphase lattice Boltzmann methods: Theory and application*. 2015: John Wiley & Sons.

45. Succi, S., *The lattice Boltzmann equation: for fluid dynamics and beyond*. 2001: Oxford university press.

46. Succi, S., *The Lattice Boltzmann Equation: For Complex States of Flowing Matter*. 2018: Oxford University Press.

47. Wolf-Gladrow, D.A., *Lattice-gas cellular automata and lattice Boltzmann models: an introduction*. 2004: Springer.

48. Parsa, M.R. and A.J. Wagner, *Lattice gas with molecular dynamics collision operator.* Physical Review E, 2017. **96**(1): p. 013314.

49. Shan, X., *Analysis and reduction of the spurious current in a class of multiphase lattice Boltzmann models.* Physical Review E, 2006. **73**(4): p. 047701.

50. Sbragaglia, M., et al., *Generalized lattice Boltzmann method with multirange pseudopotential.* Physical Review E, 2007. **75**(2): p. 026702.

51. Sbragaglia, M. and X. Shan, *Consistent pseudopotential interactions in lattice Boltzmann models.* Physical Review E, 2011. **84**(3): p. 036703.

52. Khajepor, S., J. Wen, and B. Chen, *Multipseudopotential interaction: a solution for thermodynamic inconsistency in pseudopotential lattice Boltzmann models.* Physical Review E, 2015. **91**(2): p. 023301.

53. Khajepor, S. and B. Chen, *Multipseudopotential interaction: A consistent study of cubic equations of state in lattice Boltzmann models.* Physical Review E, 2016. **93**(1): p. 013303.

54. Li, Q., K.H. Luo, and X. Li, *Forcing scheme in pseudopotential lattice Boltzmann model for multiphase flows.* Physical Review E, 2012. **86**(1): p. 016709.

55. Yuan, P. and L. Schaefer, *Equations of state in a lattice Boltzmann model.* Physics of Fluids, 2006. **18**(4): p. 042101.

56. Kupershtokh, A., D. Medvedev, and D. Karpov, *On equations of state in a lattice Boltzmann method.* Computers & Mathematics with Applications, 2009. **58**(5): p. 965-974.

57. Zhang, J. and F. Tian, *A bottom-up approach to non-ideal fluids in the lattice Boltzmann method.* EPL (Europhysics Letters), 2008. **81**(6): p. 66005.

58. Sukop, M. and D. Thorne, *Lattice Boltzmann modeling: An introduction for geoscientists and engineers. Springer-Verlag, Berlin.* Lattice Boltzmann modeling: An introduction for geoscientists and engineers. Springer-Verlag, Berlin., 2006: p. -.

59. Krook, P.B.-E.G.-M., P. Bhatnagar, and E. Gross, *A model for collision processes in gases.* Phy. Rev, 1954. **94**: p. 511-524.

60. Shan, X., X.-F. Yuan, and H. Chen, *Kinetic theory representation of hydrodynamics: a way beyond the Navier–Stokes equation.* Journal of Fluid Mechanics, 2006. **550**: p. 413-441.

61. Shan, X., *Pressure tensor calculation in a class of nonideal gas lattice Boltzmann models.* Physical Review E, 2008. **77**(6): p. 066702.

62. Benzi, R., et al., *Mesoscopic modeling of a two-phase flow in the presence of boundaries: the contact angle.* Physical Review E, 2006. **74**(2): p. 021509.

63. Guo, Z., C. Zheng, and B. Shi, *Discrete lattice effects on the forcing term in the lattice Boltzmann method.* Physical Review E, 2002. **65**(4): p. 046308.

64. Chapman, W.G., et al., *New reference equation of state for associating liquids.* Industrial & Engineering Chemistry Research, 1990. **29**(8): p. 1709-1721.

65. Michelsen, M.L. and E.M. Hendriks, *Physical properties from association models.* Fluid phase equilibria, 2001. **180**(1-2): p. 165-174.

66. Hendriks, E., J. Walsh, and A. Van Bergen, *A general approach to association using cluster partition functions.* Journal of statistical physics, 1997. **87**(5-6): p. 1287-1306.

67. Huang, S.H. and M. Radosz, *Equation of state for small, large, polydisperse, and associating molecules.* Industrial & Engineering Chemistry Research, 1990. **29**(11): p. 2284-2294.

68. Maple, *Toronto: Maplesoft, a division of Waterloo Maple Inc.* 2017.

69. MATLAB, *The MathWorks, Inc., Natick, Massachusetts, United States.* R2018b.

70. Ugray, Z., et al., *Scatter search and local NLP solvers: A multistart framework for global optimization.* INFORMS Journal on Computing, 2007. **19**(3): p. 328-340.

71. Colosqui, C.E., et al., *Mesoscopic simulation of non-ideal fluids with self-tuning of the equation of state.* Soft Matter, 2012. **8**(14): p. 3798-3809.

72. Huang, H., M. Krafczyk, and X. Lu, *Forcing term in single-phase and Shan-Chen-type multiphase lattice Boltzmann models.* Physical Review E, 2011. **84**(4): p. 046710.

73. Li, Q., K. Luo, and X. Li, *Lattice Boltzmann modeling of multiphase flows at large density ratio with an improved pseudopotential model.* Physical Review E, 2013. **87**(5): p. 053301.

74. Yu, Z. and L.-S. Fan, *Multirelaxation-time interaction-potential-based lattice Boltzmann model for two-phase flow.* Physical Review E, 2010. **82**(4): p. 046708.

75. Bjørner, M.G. and G.M. Kontogeorgis, *Modeling derivative properties and binary mixtures with CO_2 using the CPA and the quadrupolar CPA equations of state.* Fluid Phase Equilibria, 2016. **408**: p. 151-169.

76. Bjørner, M.G., G. Sin, and G.M. Kontogeorgis, *Uncertainty analysis of the CPA and a quadrupolar CPA equation of state–With emphasis on CO_2.* Fluid Phase Equilibria, 2016. **414**: p. 29-47.

77. Zhang, L., et al., *The role of wettability of nonideal nozzle plate: From drop-on-demand droplet jetting to impact on solid substrate.* AIChE Journal, 2018. **64**(7): p. 2837-2850.

78. Li, Q. and K. Luo, *Thermodynamic consistency of the pseudopotential lattice Boltzmann model for simulating liquid–vapor flows.* Applied Thermal Engineering, 2014. **72**(1): p. 56-61.

79. Li, Q. and K. Luo, *Achieving tunable surface tension in the pseudopotential lattice Boltzmann modeling of multiphase flows.* Physical Review E, 2013. **88**(5): p. 053307.

80. Xu, A., et al., *A three-dimensional pseudo-potential-based lattice Boltzmann model for multiphase flows with large density ratio and variable surface tension.* International Journal of Heat and Fluid Flow, 2015. **56**: p. 261-271.

81. Falcucci, G., et al., *Lattice Boltzmann models with mid-range interactions.* Commun. Comput. Phys, 2007. **2**(6): p. 1071-1084.

82. Falcucci, G., et al., *Lattice Boltzmann methods for multiphase flow simulations across scales.* Communications in Computational Physics, 2011. **9**(2): p. 269-296.

83. Falcucci, G., S. Ubertini, and S. Succi, *Lattice Boltzmann simulations of phase-separating flows at large density ratios: the case of doubly-attractive pseudo-potentials.* Soft Matter, 2010. **6**(18): p. 4357-4365.

84. Montessori, A., et al., *Multicomponent lattice Boltzmann models for biological applications*, in *Numerical Methods and Advanced Simulation in Biomechanics and Biological Processes*. 2018, Elsevier. p. 357-370.

85. Geier, M., A. Greiner, and J.G. Korvink, *Cascaded digital lattice Boltzmann automata for high Reynolds number flow.* Physical Review E, 2006. **73**(6): p. 066705.

86. Mukherjee, S., P. Berghout, and H.E. Van den Akker, *A lattice Boltzmann approach to surfactant-laden emulsions.* AIChE Journal, 2018.

3. CHAPTER THREE

Central-Moments-Based Lattice Boltzmann for Associating Fluids: A New Integrated Approach

Preface

A version of this manuscript has been published in the Journal of Physical Chemistry B, 2020. **124**(14): p. 2900-2913. Asadi, M.B. is the primary author of this paper. Along with the co-authors (De Rosis, A., and Zendehboudi, S.), Asadi developed the conceptual thermodynamic and Lattice Boltzmann models and designed the manuscript's structure. Most of the literature review, data collection, and the performance comparison of different methods were done by Asadi, M.B., as the first author. The first draft and revised version of the manuscript were prepared by the first author based on the co-authors' feedback and comments received from journal reviewers. De Rosis, A. provided the central moments part and helped in explaining the results. The co-author, Zendehboudi, S., had the supervision role and edited the manuscript.

ABSTRACT

Dynamic and thermodynamic behavior of associating fluids play a crucial role in a variety of engineering and science disciplines. Cubic plus association equation of state (CPA EOS) is implemented in a central-moments-based lattice Boltzmann method (LBM) in order to mimic the thermodynamic behavior of associating fluids. The pseudopotential approach is selected to model the multiphase thermodynamic characteristics such as reduced density of associating fluids. The priority of central moments-based approach over multiple-relaxation-time collision operator is shown by performing double shear layers. The integration of central-moments-based LBM and CPA EOS is useful to simulate associating fluids at high flow rate conditions, which is extended to high-density ratio scenarios by increasing the anisotropy order of gradient operator. In order to increase the stability of the model, a higher anisotropy order of the gradient operator is implemented; about 34 present reduction in spurious velocities is noticed in some cases. The type of gradient operator considerably affects the model thermodynamic consistency. Finally, the model is validated by observing a straight line in the Laplace law test. Prediction of thermodynamic behaviours of associating fluids is of significance in biological processes as well as fluid flow in porous media.

***Keywords*:** Associating fluid; Cubic plus association equation of state; central-moments-based lattice Boltzmann method; gradient operator; Laplace law

3.1 INTRODUCTION

Lattice Boltzmann method (LBM) has roots in the lattice gas automaton (LGA) [1-4]. This method has been developed as an option to simulate fluid flow behaviours and numerically solve nonlinear equations. Basically, fluid dynamics can involve the motion of distributions/populations of fabricated particles which can stream and colloid along a Cartesian lattice. LBM has been employed in a broad range of engineering applications such as single-phase flow [5-7], multiphase flow [8-11], phase-change heat transfer [10, 12], turbulent regime in various transport phenomena [13-17], and solving nonlinear partial differential equations (NPDEs) including convection-diffusion equations [18-24]. The kinetic basis of LBM makes it a powerful tool in the modeling of interfacial phenomena in the multiphase flow systems [25-27]. Although the origin of LBM is molecular dynamic kinetic which is more fundamental compared to the continuum approaches, it is capable of recovering the traditional macroscopic scale continuity and Navier–Stokes (N–S) equations. In the absence of required meshes movement, it can be parallelized due to locality of most of the computations. In the LBM, different boundary conditions can be handled easily.

As a common collision operator, Bhatnagar Gross and Krook (BGK), which is known as a single relaxation time collision operator, enforces all the populations to relax to an equilibrium state with the same rate [28]. Due to non-hydrodynamic ghost modes, the single relaxation time is instable in the high-velocity gradient cases, when the single relaxation time of BGK collision operator is implemented. Huang et al. [29] demonstrated an inverse relationship between the highest achievable density (by aforementioned techniques) and the viscosity of fluid. In order to address this concern and achieve high Reynolds numbers, multiple-relaxation-time (MRT) collision operator is presented based on decomposing the collision operator as well as raw moments. These moments correspond to different hydrodynamic parameters and their fluxes which are able to relax at different time scales. The Prandtl number is fixed in BGK collision operator; by damping non-hydrodynamic modes [30] and acoustic waves [31] in MRT collision operator, one can achieve a model to adjust Prandtl number, improve the numerical stability, and handle the modeling of complex fluids such as viscoelastic fluids [32]. Since the MRT operator represents the collision in a frame at rest, the Galilean invariance is also trimmed. Yu and Fan utilized the MRT collision operator in the pseudopotential LBM [33]. Later on, this approach was modified through implementing an improved force scheme by Li et al. [34].

Recently, Geier et al. [35] introduced a novel collision kernel through shifting the lattice directions by the local fluid velocity. They presented a pyramidal hierarchical structure by developing the central moments (CMs) concept. In this structure, the post-collision state of a certain moment at a given order depends on lower-order ones. Thus, this collision operator is also known as "cascaded operator". Originally, an orthogonal basis of central moments, which relaxes to the equilibrium state of the continuous Maxwellian distribution is assumed for the cascaded LBM. In spite of overwhelming analytical formulation and practical implementation specifically in three-dimensional cases [36], this method leads to a considerable stability enhancement in many cases [35, 37-54]. Recently, De Rosis developed a new LBM framework based on the central moments, which is different from the cascaded scheme in two aspects. First, a non-orthogonal basis is adopted and second, the relaxation to the discrete second-order shortened the equilibrium population. The non-pyramidal structure demonstrates notable characteristics in terms of stability, convergence, and accuracy [55, 56].

Generally, two-phase/multiphase LBMs can be categorized in four groups: color-gradient [57, 58], pseudopotential [59, 60], free-energy [61, 62], and mean-field [63]. However, the LBM classification can be changed based on different aspects such as methodology, structure, limitations and capabilities, and application [10]. Due to the simplicity in the implementation and good efficiency in the computation, the pseudopotential LBM approach has received significant attention among several multiphase LBM models [57-62, 64]. The particle interactions in the pseudopotential approach help the phase segregation so that this technique does not require other numerical methods to track and capture the interfaces. Besides the important features of the pseudopotential LBM, its shortcomings include thermodynamic inconsistency and high spurious velocities. Implementing the pseudopotential approach for reaching high Reynolds number/ low viscosity cases is still challenging as multiple issues (reaching high-density ratio, increasing thermodynamic consistency, decreasing spurious velocity, and increasing the Reynolds number/decreasing viscosity) should be handled simultaneously. Thermodynamic inconsistency is addressed by introducing new pseudopotential forms [65] and effective forcing scheme [66]. Sbragaglia et al. introduced multi-range pseudopotential through combination of nearest and next-nearest neighbor interactions [67]. Falcucci et al. presented a double attractive pseudopotential to reach high-density ratios [68]. To overcome high spurious velocities, using higher anisotropy order of gradient operator is proposed [69].

Yuan and Schaefer evaluated the thermodynamic consistency of LBM by comparing the simulation results of an stationry droplet with Maxwell equal-area construction when different cubic and non-cubic equations of state (EOSs) are used. Also, they investigated the impacts of different EOSs on the maximum sperious velocity [70]. They compared the LBM results with experimental data of water. In the liquid phase branch, a notable difference between the experimental data and LBM results was observed. Cubic EOSs such as Peng-Robinson (PR) [71] and Soave-Redlich-Kwong (SRK) [72] have been widely used to study the thermodynamic behaviors of hydrocarbon and non-hydrocarbon fluids due to their simplicity and accuracy.

Compared to the physical interactions, polar components may form a stronger bonding. In the presence of fluids with hydrogen bonding, some unusual thermodynamic behaviors such as high liquid density, reverse density trend during solidification, and high boiling point are observed, which may not be fully explored (and justified) by cubic EOSs [73]. Water is an associating component which can exist in different fluid mixtures such as petroleum reservoir fluids in various forms such as connate water and injection fluids. Taking another example of associating fluids, asphaltene that might contain a group of complex components may form aggregates due to the association forces. Asadi and Zendehboudi [74] introduced a new approach to decrease the differences between LBM results and experimental data of associating fluids. The cubic plus association (CPA) EOS was incorporated in LBM while the CPA EOS association parameters are recalculated to be used in LBM. Originally, CPA EOS was introduced by Kontogeorgis et al. [75] to consider both physical and associating interactions. In general, CPA EOS consists of two terms to take into account both interactions. CPA EOS can turn to a cubic EOS in the absence of associating interactions. Although there are other EOSs such as perturbed-chain statistical associating fluid theory (PC-SAFT) with the capability of considering association bonds, CPA EOS has a lower computational cost.

Most of the available studies use the BGK collision operator to investigate the thermodynamic behaviors of fluids. As mentioned earlier, the single relaxation time collision operator can lead to valid/reasonable results within a specific range of dynamic viscosity. On the other hand, the MRT collision operator effectively works within limited intervals of Reynolds and Mach numbers.

In this chapter, we aim to fill the above knowledge gap by implementing the CPA EOS in the central moments-based LBM, in order to improve the thermodynamical behaviors of fluids and decrease the numerical instability by increasing the isotropy order of gradient operator. The central moments-based collision operatore is employed to increase the stability of model at high Reynolds and Mach number conditions. CPA EOS is incorporated in the LBM to mimc the thermodynamical behaviours of associatiog fluids.

The remaining of the chapter is organized as follows. First, a review on pseudopotential LBM with different collision operators and incorporation of CPA EOS in the LBM are presented in the THEORY AND METHODOLOGY section. Then, the necessity of more accurate EOSs is presented by showing the flexibility of some common pseudopotentials to predict the thermodynamic properties. After that, the introduced approach is evaluated by comparing the two-phase density results of central-moments-based LBM with Maxwell equal-area construction where different anisotropy orders of gradient operator are employed. The sperious velocity at different viscosity is examined, and the method is validated by Laplace law. Finally, the main outcomes of the current study are presented in the CONCLUSIONS section.

3.2 THEORY AND METHODOLOGY

In this section, first, the pseudopotential LBM, classical BGK collision operator, multi-relaxation time (MRT), and central-moments-based LBM are briefly explained. Then, the combination procedure of consistent pseudopotential interactions proposed by Shan and Chen (SC), Sbragaglia and Shan (SS), and cubic/CPA EOSs are presented.

Pseudopotential LBM, classical BGK, MRT, and central-moments based LBM. The discrete LB equation describes the evolution of the particle distribution function (PDF) f_i in time t and space $x = [x, y]$ which moves on a lattice structure along a direction i with velocity $c_i = [c_{xi}, c_{yi}]$ during the time step, $\Delta t = 1$. The corresponding equation is presented as follows:

$$f_i(\boldsymbol{x} + \Delta t\boldsymbol{c_i}, t + \Delta t) = f_i(\boldsymbol{x}, t) + \Omega_i(\boldsymbol{x}, t) + S_i \tag{3-1}$$

In Equation (3-1), S_i stands for the forcing term in the discrete LB equation.

Equation (3-1) is solved through the following steps:

$$\text{Collision :} \quad f_i^*(\boldsymbol{x}, t) = f_i(\boldsymbol{x}, t) + \Omega_i(\boldsymbol{x}, t) \tag{3-2}$$

$$\text{Streaming :} \quad f_i(\boldsymbol{x} + \Delta t\boldsymbol{c_i}, t + \Delta t) = f_i^*(\boldsymbol{x}, t) \tag{3-3}$$

where $\Omega_i(x, t)$ symbolizes the collision operator and superscript $*$ refers to the post-collision quantities. The fluid density, ρ, and velocity vector field, $u = [u_x, u_y]$, are calculated by zeroth and first-order momentums of the population as expressed below:

$$\rho = \sum_i f_i\,; \quad \rho u = \sum_i f_i\,\boldsymbol{c_i} \tag{3-4}$$

The mean-field interaction force applies to simulate the molecular interactions, which lead to the phase separation. The pseudopotential (also known as effective mass) $\psi = \psi(\rho)$, is defined by the local density (ρ). The summation of the pairwise interactions between particles at a given site x and neghboring sites x' is considered as the interparticle force in the single-component multiphase (SCMP) LBM. Shan and Chen defined the lattice version of the interaction potential to introduce the long-range intermolecular interaction, as follows:

$$V(x, x') = G(x, x')\psi(x)\psi(x') \tag{3-5}$$

where $G(x, x') = G(x - x')$ is a Green's function. Based on the interaction potential, the interparticle forces ($\boldsymbol{F}_{int}$) can be written as:

$$\boldsymbol{F}_{int}(x, t) = -G|\boldsymbol{e}_a|\psi(x, t)\sum_{i=0}^{q}\psi(x + \boldsymbol{e}_{\boldsymbol{a}}, t)\boldsymbol{e}_a \tag{3-6}$$

where q symbolizes the number of the neighboring sites. The right-hand side of Equation (3-6) represents the finite difference form of $-\psi\Delta(\psi)$ and an unspecified relative interaction strength at different distances. The relative interaction strength is determined based on the finite difference gradient operator, which imposes the sufficient anisotropy to lower the spurious current velocity at a curved interface of multiphase. Following the standard analysis procedure of finite difference, the Taylor series of an arbitrary multi-dimensional function f at lattice site x and $[: a = 1, \ldots, d]$ as a set of vector starting from x to its d neighbors is given below:

$$f(x + e) = \Sigma_{\mathrm{n}=0}^{\infty}\frac{1}{n!}\left[\nabla^{(n)}f(x)\right] \cdot ee \cdots e \tag{3-7}$$

where x is a lattice site and the product of the right-hand side is a complete contraction between two rank-n tensor contractions. Based on the standard notation of Wolfram [76], one can write:

$$E_{i_1 i_2 \ldots i_n}^{(n)} = \Sigma_i w(|\boldsymbol{e}_a|^2)\ (\boldsymbol{e}_a)_{i_1} \cdots (\boldsymbol{e}_a)_{i_n} \tag{3-8}$$

in which, $w(|c_i|^2)$ are the weights. Considering the finite difference approximation to the gradient of f in Equation (3-7) results in:

$$\Sigma_i w(|\boldsymbol{e}_a|^2)\, f(x+\boldsymbol{e}_a)\boldsymbol{e}_a = (\nabla f)\cdot E^{(2)} + \frac{1}{3!}\left(\nabla^{(3)} f\right)\cdot E^{(4)} + \frac{1}{5!}\left(\nabla^{(5)} f\right)\cdot E^{(6)} + \cdots. \tag{3-9}$$

Shan [69] followed the above procedure and calculated weights, which leads to unit $E^{(2)}$and isotropic $E^{(n)}$ (see Table 3-1).

Table 3-1: Calculated weights based on the unit $E^{(2)}$and isotropic $E^{(n)}$ tensors in two and three dimensions.

	Tensor	$w(1)$	$w(2)$	$w(3)$	$w(4)$	$w(5)$	$w(6)$	$w(8)$
2D	$E^{(4)}$	1/3	1/12					
	$E^{(6)}$	4/15	1/10		1/120			
	$E^{(8)}$	4/21	4/45		1/60	2/315		1/5040
3D	$E^{(4)}$	1/6	1/12					
	$E^{(6)}$	2/15	1/15	1/60	1/120			
	$E^{(8)}$	4/45	1/21	2/105	5/504	1/315	1/630	1/5040

By expanding the interaction forces (see Equation (3-6)) through the Taylor series, one can have the following expression [66]:

$$\boldsymbol{F}_{int}(x,t) = -Gc^2[\psi\nabla\psi + \frac{1}{2}c^2\psi\nabla(\nabla^2\psi) + \cdots] \tag{3-10}$$

The pressure tensor should be obtained to analyse the mechanical balance at the interface. As a general rule, the pressure tensor is given as follows [77]:

$$\Sigma P.A = \Sigma_x F \qquad (3\text{-}11)$$

in which, P introduces the pressure and A is the area. The analytical expression of the normal pressure tensor in the one-dimensional case is expressed as:

$$P_n = c_s^2\rho + \frac{1}{2}Gc^2\psi^2(\rho) + \frac{Gc^4}{12}\left[\alpha\left(\frac{d\psi}{dn}\right)^2 + \beta\psi\frac{d^2\psi}{dn^2}\right] \qquad (3\text{-}12)$$

in which, $\alpha = 1 - 3e_4, \beta = 1 + 6e_4$ where e_4 is the fourth-order tensor as given below [77]:

$$e_4 = \frac{\omega_1}{2} + 2\omega_2 + 8\omega_4 + 25\omega_5 + 32\omega_8 + \cdots \qquad (3\text{-}13)$$

The bulk pressure (p_b) is equal to the first two diagonal terms of the pressure tensor in Equation (3-12). The pseudopotential can be defined based on the bulk pressure as [70, 78]:

$$\psi(\rho) = \sqrt{\frac{2(P_b - c_s^2\rho)}{Gc^2}} \qquad (3\text{-}14)$$

Different EOSs can be incorporated in the LBM through Equation (3-14).

Based on the BGK assumptions, the collision operator (Ω_i) is defined by a single relaxation of population with the same rate to a local equilibrium. The BGK collision operator is given below:

$$\Omega_i = \frac{(f_i^{eq} - f_i)}{\tau} \qquad (3\text{-}15)$$

where τ denotes the single relaxation time scale, which is related to the kinematic viscosity of the fluid according to the following equation:

$$\nu = \left(\tau - \frac{1}{2}\right) c_s^2 \Delta t \tag{3-16}$$

In Equation (3-15), f_i^{eq} is the equilibrium PDF, as defined below:

$$f_i^{eq} = w_i \rho \left[1 + 3\boldsymbol{c_i} \cdot \boldsymbol{u} + \frac{9}{2}(\boldsymbol{c_i} \cdot \boldsymbol{u})^2 - \frac{3}{2}\boldsymbol{u} \cdot \boldsymbol{u}\right] \tag{3-17}$$

where $w_i s$ are a set of weights, which are determined based on the LB model.

In general, the collision process includes multiple physical quantities that may relax on the different time scales. To consider the information of the time scales, a full constant matrix (Λ) is employed instead of a single time scale, τ. Therefore, the collision operator can be rewritten as follows:

$$\Omega_i = \Sigma_j \Lambda_{ij}\left(f_j^{eq} - f_j\right) \tag{3-18}$$

Following the derivation presented by Premnath and Abraham [79], by applying the transformation, $\bar{f_i} = f_i - 1/2\Delta t$, Equation (3-1) can be rewritten as follows:

$$\begin{aligned} &\bar{f_i}(\boldsymbol{x} + \Delta t \boldsymbol{c_i}, t + \Delta t) \\ &\quad = \bar{f_i}(\boldsymbol{x}, t) + \Sigma_j \Lambda_{ij}\left(f_j^{eq} - \bar{f_j}\right)|_{(x,t)} + \Sigma_j \left(I_{ij} - \frac{1}{2}\Lambda_{ij}\right) S_i|_{(x,t)} \Delta t \end{aligned} \tag{3-19}$$

where I_{ij} is the components of the identity matrix. Solving Equation (3-19) requires a complex matrix manipulation. A linear transformation can be used to diagonalize the collision matrix. The transformation matrix **T** transform the distribution functions from velocity space ($\bar{f_i}$) into the moment space ($\hat{f_i}$), which are related to the macroscopic physical quantities such as density, momentum, energy, and their flux. The transformation matrix form is related to the lattice structure. The explicit form of D2Q9 is presented below [80]:

$$\mathbf{T}=\begin{bmatrix} 1 & 1 & 1 & 1 & 1 & 1 & 1 & 1 & 1 \\ -4 & -1 & -1 & -1 & -1 & 2 & 2 & 2 & 2 \\ 4 & -2 & -2 & -2 & -2 & 1 & 1 & 1 & 1 \\ 0 & 1 & 0 & -1 & 0 & 1 & -1 & -1 & 1 \\ 0 & -2 & 0 & 2 & 0 & 1 & -1 & -1 & 1 \\ 0 & 0 & 1 & 0 & -1 & 1 & 1 & -1 & -1 \\ 0 & 0 & -2 & 0 & 2 & 1 & 1 & -1 & -1 \\ 0 & 1 & -1 & 1 & -1 & 0 & 0 & 0 & 0 \\ 0 & 0 & 0 & 0 & 0 & 1 & -1 & 1 & -1 \end{bmatrix} \tag{3-20}$$

The transformed form of Equation (3-19) into moment space can be calculated by multiplying the transformation matrix **T**, as given below:

$$\begin{aligned} &\hat{f}_i(\boldsymbol{x}+\Delta t\boldsymbol{c_i}, t+\Delta t) \\ &\qquad = \hat{f}_i(\boldsymbol{x}, t) + \Sigma_\beta \widehat{\Lambda}_{i\beta}\left(\hat{f}_\beta^{eq} - \hat{f}_\beta\right)|_{(x,t)} + \Sigma_\beta\left(I_{i\beta} - \frac{1}{2}\widehat{\Lambda}_{i\beta}\right)\hat{S}_i|_{(x,t)}\Delta t \end{aligned} \tag{3-21}$$

The transformed collision matrix $\widehat{\Lambda}_{i\beta} = \mathrm{T}\Lambda\mathrm{T}^{-1}$ is become diagonal (for the D2Q9 lattice), as follows:

$$\widehat{\Lambda} = diag[s_1, s_2, s_3, s_4, s_5, s_6, s_7, s_8, s_9] \tag{3-22}$$

The diagonal elements of $\widehat{\Lambda}$, s_1 through s_9, are the new relaxation parameters in associating with elements of $\hat{f}_i$.

According to Malaspinas [81] and Coreixas [82, 83], the complete expression of the equilibrium distributions is

$$
\begin{aligned}
f_i^{eq} = w_i\, \rho\, [1 + \frac{\boldsymbol{c_i} \cdot \boldsymbol{u}}{c_s^2} + \frac{1}{2\, c_s^4}\, \mathcal{H}_i^{(2)} \\
:\, \boldsymbol{uu} + \frac{1}{2c_s^6}\left(\mathcal{H}_{ixxy}^{(3)}\, u_x^2\, u_y + \mathcal{H}_{ixyy}^{(3)}\, u_x\, u_y^2 \right) \\
+ \frac{1}{4c_s^8}\, \mathcal{H}_{ixxyy}^{(4)} u_x^2\, u_y^2\,]
\end{aligned}
\qquad (3\text{-}23)
$$

with $\mathrm{w}_0 = 4/9$, $\mathrm{w}_{1\dots4} = 1/9$, $\mathrm{w}_{5\dots8} = 1/36$, $\mathrm{c_s} = 1/\sqrt{3}$ is the lattice sound speed and $\mathcal{H}^{(\mathrm{n})}$ denotes the Hermite polynomial of order n. Notice that Equation (3-23) degrades into the classical second-order truncated formula if $\mathcal{H}^{(3)}$ and $\mathcal{H}^{(4)}$ are neglected.

In order to create a CMs-based collision operator, one should adopt lattice directions shifted by the local fluid velocity (see Geier et al.[35]), $\bar{\boldsymbol{c}}_i = [|\bar{\boldsymbol{c}}_{xi}\rangle, |\bar{\boldsymbol{c}}_{yi}\rangle]$, where

$$
\begin{aligned}
|\bar{\boldsymbol{c}}_{xi}\rangle = |\boldsymbol{c}_{xi} - u_x\rangle \\
|\bar{\boldsymbol{c}}_{yi}\rangle = |\boldsymbol{c}_{yi} - u_y\rangle
\end{aligned}
\qquad (3\text{-}24)
$$

Then, we transform distributions into moments (and vice versa) by applying the matrix $\bar{\mathcal{T}} = [\bar{T}_0, \dots, \bar{T}_i, \dots, \bar{T}_8]$ (see for example De Rosis and Luo [86]) where

$$
\begin{aligned}
|\bar{T}_0\rangle = |1, \dots, 1\rangle \\
|\bar{T}_1\rangle = |\bar{c}_{xi}\rangle \\
|\bar{T}_2\rangle = |\bar{c}_{yi}\rangle \\
|\bar{T}_3\rangle = |\bar{c}_{xi}^2 + \bar{c}_{yi}^2\rangle \\
|\bar{T}_4\rangle = |\bar{c}_{xi}^2 - \bar{c}_{yi}^2\rangle
\end{aligned}
\qquad (3\text{-}25)
$$

$$|\bar{T}_5\rangle = |\bar{c}_{xi}\bar{c}_{yi}\rangle$$

$$|\bar{T}_6\rangle = |\bar{c}_{xi}^2\bar{c}_{yi}\rangle$$

$$|\bar{T}_7\rangle = |\bar{c}_{xi}\bar{c}_{yi}^2\rangle$$

$$|\bar{T}_8\rangle = |\bar{c}_{xi}^2\bar{c}_{yi}^2\rangle$$

We can evaluate pre-collision and equilibrium CMs as

$$|k_i\rangle = \bar{\mathcal{T}}^T|f_i\rangle \qquad |k_i^{eq}\rangle = \bar{\mathcal{T}}^T\left|f_i^{eq}\right\rangle \tag{3-27}$$

respectively, where

$$|k_i\rangle = [k_0, \dots, k_i, \dots, k_8]^\top \qquad |k_i^{eq}\rangle = \left[k_0^{eq}, \dots, k_i^{eq}, \dots, k_8^{eq}\right]^\top \tag{3-26}$$

and $|f_i^{eq}\rangle = [f_0^{eq}, \dots, f_i^{eq}, \dots, f_8^{eq}]^\top$. We obtain that only three equilibrium central moments are different from zero:

$$k_0^{eq} = \rho \qquad k_3^{eq} = 2\rho c_s^2 \qquad k_8^{eq} = \rho c_s^4 \tag{3-28}$$

and $k_{1,2,4,5,6,7}^{eq} = 0$. Indeed, as stated in De Rosis and Luo [84], the discrete equilibrium CMs are equal to those of the continuous Maxwellian distribution when the full set of Hermite polynomials is considered. Let us denote the $9 * 9$ unit tensor as $\mathbf{I}$ and the $9 * 9$ relaxation matrix as $\Lambda = \mathrm{diag}[1,1,1,1,\omega,\omega,1,1,1]$. Following De Rosis et al.[56], the post-collision state in terms of central moments is

$$| k_i^{\star} \rangle = (\mathbf{I} - \Lambda)\, \bar{\mathcal{T}}^{\top} |f_i\rangle + \Lambda \bar{\mathcal{T}}^{\top} | f_i^{eq} \rangle + (\mathbf{I} - \frac{\Lambda}{2}) \bar{\mathcal{T}}^{\top} | \mathcal{F}_i \rangle \tag{3-29}$$

The last ingredient to be defined is the forcing term $\mathcal{F}_i$. Similarly to the approach adopted for the equilibrium distribution (see Eq.(3-23)), Huang et al. [85] suggested to expand the forcing term as

$$\mathcal{F}_i = w_i \left(\frac{F}{c_s} . \mathcal{H}^{(1)} + \frac{[Fu]}{2c_s^2} . \mathcal{H}^{(2)} + \frac{[Fuu]}{6c_s^3} . \mathcal{H}^{(3)}_{[xyy],[xxy]} + \frac{[Fuuu]}{24c_s^4} . \mathcal{H}^{(4)}_{[xxyy]} \right) \tag{3-30}$$

where the square bracket in Hermite coefficient denotes permutations. The popular formula by Guo et al. [86] is then recovered when $\mathcal{H}^{(3)}$ and $\mathcal{H}^{(4)}$ are disregarded. The central moments of the discrete force term are[56]

$$|R_i\rangle = \bar{\mathcal{T}}^{T} |\mathcal{F}_i\rangle \tag{3-31}$$

where

$$\begin{aligned} |R_1\rangle &= F_x \\ |R_2\rangle &= F_y \\ |R_6\rangle &= F_y c_s^2 \\ |R_7\rangle &= F_x c_s^2 \end{aligned} \tag{3-32}$$

and $R_{0,3,4,5,8} = 0$. These compact expressions are different from those by Huang et al.[84] due to the choice of a different basis. Moreover, one can notice that Equations (3-32) can also be obtained when the velocity terms in Equations (3-15) of De Rosis [44] are neglected. Indeed, we remark the concept stated by De Rosis et al.[56], where it has been demonstrated that the adoption of the Hermite polynomials of the maximum admissible order (n=4 in the D2Q9 space according to Malaspinas[81]) leads to Galilean-invariant (or, in other words, velocity-independent) equilibrium and forcing central moments.

This concise scheme leads to post-collision central moments that are (see De Rosis et al.[56]):

$$\begin{gathered}
k_0^\star = \rho \\
k_1^\star = \frac{F_x}{2} \\
k_2^\star = \frac{F_y}{2} \\
k_3^\star = 2\rho c_s^2 \\
k_4^\star = (1-\omega)k_4 \\
k_5^\star = (1-\omega)k_5 \\
k_6^\star = \frac{F_y}{6} \\
k_7^\star = \rho c_s^4
\end{gathered} \tag{3-33}$$

Then, we can reconstruct post-collision populations $|f_i^\star\rangle = [f_0^\star, \ldots, f_i^\star, \ldots, f_8^\star]^{\mathrm{T}}$ by applying the back-transformation (see De Rosis[55])

$$|f_i^\star\rangle = (\bar{\mathcal{T}}^T)^{-1}|k_i^\star\rangle \tag{3-34}$$

Incorporating equations of state. In this part, Peng-Robinson (PR) EOS, as one of most successive EOSs in both academic and industrial sectors [87], and cubic plus association (CPA) EOS [73], as an accurate and computational cost effective EOS in simulating associating fluids, Shen and Chen EOS (SC EOS), an original EOS which implemented in pseudopotential LBM, and Sbragaglia and Shan EOS (SS EOS), a thermodynamic consistence EOS, are briefly reviewed.

PR as a cubic EOS was developed due to the low accuracy of Soave-Redlich-Kwong (SRK) EOS [72] in predicting the liquid density of heavy hydrocarbons. The liquid density calculated by SRK is usually higher than the experimental measured values [88]. Peng and Robinson EOS followed the same strategy as SRK model in thermodynamic modeling, except the van der Waals attractive term was modified as given below:

$$P = \frac{RT}{v-b} - \frac{a}{v(v+b)+b(v-b)} \tag{35}$$

in which

$$a = a_c\alpha(T) \tag{3-36}$$

$$\alpha = \left[1 + (0.37464 + 1.54226\omega - 0.26992\omega^2)\left(1-\sqrt{T_r}\right)\right]^2 \tag{3-37}$$

$$a_c = 0.45724\frac{R^2T_c^2}{P_c}, b = 0.07780\frac{RT_c}{P_c} \tag{3-38}$$

where P stands for the pressure; R denotes the universal gas constant; v introduces the molar volume; a and b are the attraction and repulsion terms, respectively; α represents the temperature dependence function in the attraction term; and the subscript c refers to the critical properties. Second term in Equation (3-35) is the attraction term. Peng and Robinson added $b(v-b)$ to the attraction term, which improves the attractive pressure force impact.

CPA EOS was proposed based on a cubic EOS and the statistical associating fluid theory (SAFT) for modeling of physical interactions and associating forces, respectively. The CPA EOS reduces to a cubic EOS in the absence of associating force (e.g., hydrogen bonding compounds). Beside the simplicity and accuracy, the numerical implementation of the association term guarantees the computational time effectiveness of the CPA EOS. SRK EOS was used to describe the physical part in the original form introduced by Kontogeorgis et al. [75]. Firoozabadi proposed to use PR EOS as the physical part of CPA EOS to be suitable for thermodynamic modeling of hydrocarbon reservoir fluids [89]. The association term consists of the specific site-site interactions due to hydrogen bonding. The association interactions are listed in two categories, namely; self-association and cross-association for the same and different species, respectively. The bulk pressure of the system represented by CPA EOS is as follows:

$$P=\frac{RT}{v-b}-\frac{a}{v(v+b)+b(v-b)}-\frac{1}{2}\frac{RT}{v}\left(1-v\frac{\partial lng}{\partial v}\right)\Sigma_i x_i\Sigma_{A_i}(1-X_{Ai}),\ i=1,2,\dots,n_c \tag{3-39}$$

in which, x symbolizes the mole fraction; g introduces the hard sphere radial distribution function (RDF); A_i refers to the active association site; and X_{Ai} stands for the fraction of site A on component i that does not form association with other sites, as presented below:

$$\mathrm{g} = \frac{2-\eta}{2(1-\eta)^3} \quad \text{where } \eta = \frac{b}{4v} \tag{3-40}$$

$$\mathrm{X_{Ai}} = \frac{1}{1 + \sum_{j=1}^{n_c} \sum_{k=A,B,\dots} \rho x_j X_{kj} \Delta_{Ai}^{kj}} \tag{3-41}$$

where $\rho = 1/v$ is the density and Δ_{Ai}^{kj} introduces the self-association strength between sites A and B, as defined below:

$$\Delta_{Ai}^{kj} = g\left[exp\left(\frac{\epsilon^{A_iK_i}}{RT}\right) - 1\right] b_{ij} \beta^{A_iK_i} \tag{3-42}$$

$$\mathrm{b_{ij}} = \frac{b_i + b_j}{2} \tag{3-43}$$

in which, $\epsilon^{A_iK_i}$ and $\beta^{A_iK_i}$ refer to the self-association energy and bonding volume parameters, respectively. Like the study conducted by Asadi and Zendehboudi [74], we use four-site scheme (4C) and two site model (2B) for water [89] and alcohols [90], respectively. To keep consistency with the literature, the attraction, repulsion parameters, and universal gas constant of CPA EOS are supposed to be $a = 2/49$, $b = 2/21$, and $R = 1$, respectively, in the lattice units [70, 91].

The original EOS proposed by Shan and Chen is determined by defining the effective mass as follows:

$$\psi(\rho) = \rho_0 \left[1 - e^{-\frac{\rho}{\rho_0}}\right] \tag{3-44}$$

where ρ_0 is a constant. Based on Equation 3-14, the SC EOS can be obtained as:

$$P = \frac{\rho}{3} + \frac{c_0}{2} G \rho_0^2 \left[1 - e^{-\frac{\rho}{\rho_0}}\right]^2 \tag{3-45}$$

According to the critical characteristic condition of single component fluids (i.e., $\left(\frac{\partial P}{\partial v}\right)_T = \left(\frac{\partial^2 P}{\partial v^2}\right)_T = 0$), the critical properties of SC EOS are calculated as follows:

$$\rho_c = \rho_0 \ln 2, \qquad \text{(3-46-a)}$$

$$G_c = -\frac{4}{3\rho_o}, \qquad \text{(3-46-b)}$$

$$T_c = -\frac{1}{g_c} = \frac{3}{4}\rho_0, \qquad \text{(3-46-c)}$$

$$P_c = \rho_0 \left(\ln 2 - \frac{1}{6}\right) \qquad \text{(3-46-d)}$$

Therefore, two-phase separation of the system is guaranteed when $G < G_c$ and $\rho_v < \bar{\rho} < \rho_l$ where $\rho_v, \bar{\rho}$, and ρ_l are the gas phase, average, and liquid densities, respectively. When $G < G_c$, the temperature of the system is lower than critical temperature which means two phases might exist and when the average pressure of the system is between two phase density means that two phases should be exists.

Sbragaglia and Shan introduced a new consistence pseudo-potential as follows [65]:

$$\psi(\rho) = \left(\frac{\rho}{\epsilon + \rho}\right)^{1/\epsilon} \qquad \text{(3-47)}$$

where $\epsilon = -2\alpha/\beta$. The critical properties of SS EOS are obtained by the following equations:

$$\rho_c = -\frac{\epsilon - 2}{2}, G_c = \frac{1}{12}(\epsilon^2 - 4)\left(\frac{2-\epsilon}{2-\epsilon}\right)^{-\frac{2}{\epsilon}}, T_c = -\frac{1}{g_c} = \frac{12}{(4-\epsilon^2)\left(\frac{2-\epsilon}{2-\epsilon}\right)^{-\frac{2}{\epsilon}}}, P_c = \frac{(\epsilon-2)^2}{24} \tag{3-48}$$

Customized EOS. The numerical instability happens within the narrow regions of the interface, which fall in the unstable part of the EOS with $\left(\frac{\partial p}{\partial v}\right)_T > 0$. Due to unphysical meaning of the unstable branch, it can be modified. By increasing the slope of the unstable branch, the internal forces are increased toward the liquid side of spinodal point while the internal forces are lowered toward the vapor region [92]. Colosqui et al. proposed a piecewise linear EOS in the unstable branch which is discontinuous in its first derivation [92]. Asadi and Zendehboudi introduced a new perturbation in the unstable branch that increases the slope and is continuous in its first derivation at the same time as given below [74]:

$$P_{Customized} = P_{CPA} + \delta P \tag{3-49}$$

where,

$$\delta P = \begin{cases} 0 & if\ v < v_l \\ \kappa\left(\sin\left(\frac{\pi(v - v_l)}{L_1} + \frac{3\pi}{2}\right) + 1\right) & if\ v_l < v < v_M \\ \kappa\left(\sin\left(\frac{\pi(v - v_l)}{L_2} + \frac{\pi}{2}\right) + 1\right) & if\ v_M < v < v_g \\ 0 & if\ v_g < v \end{cases} \tag{3-50}$$

in which, $v_m = v_g - \alpha(v_g - v_l)$. v_g and v_l stand for the spinodal molar volumes on the gas and liquid sides, respectively. The perturbation is determined by a pair of (α, κ), individually.

3.3 RESULTS AND DISCUSSION

In the current research work, the central-based collision operator is implemented in the pseudopotential LBM. The flexibility of common pseudopotentials to predict the thermodynamic properties of a fluid is evaluated. The capability of implemented collision operator is determined by comparing the stability of central-moments-based LBM and MRT collision operator in the double layer shear test. A static drop test is selected to show the impact of isotropy order of gradient operator on the stability of the approach. The spurious velocity of static drop case is also studied. The thermodynamic consistency is examined by comparing the two-phase densities simulated by the proposed approach and calculated by Maxwell equal area construction. Finally, the Laplace law test is performed by determining the pressure difference of two phases at the different radius of the droplet.

Thermodynamically behavior of EOSs. Before providing further details of the central-based LBM, we briefly compare the thermodynamic behaviors simulated by different EOSs. Although SC and SS are mainly used in LBM studies, EOSs such as PR and CPA are more suitable to determine the fluid properties. Figure 3-1 shows the algebraic form of cubic equations, schematically. There is no physical meaning for branches with $v < b$. For cases with $p < p_1$, there are three roots $-(\sqrt{2}+1)b < v < 0$, $0 < v < (\sqrt{2}-1)b$, and $v > b$. The root with $v > b$ is physically acceptable and considered as the liquid phase density. For $p_2 < p < p_1$, there is only one root, which belongs to the liquid phase density. When $p_3 < p < p_2$, three roots are found. The highest belongs to gas phase, the lowest one corresponds to liquid phase, and the intermediate one has no physical meaning. In some cases, the negative pressure determines the liquid phase density (see panel b of Figure 3-1) [89, 93]. CPA EOS exhibits a behavior similar to cubic EOSs at the acceptable branches.

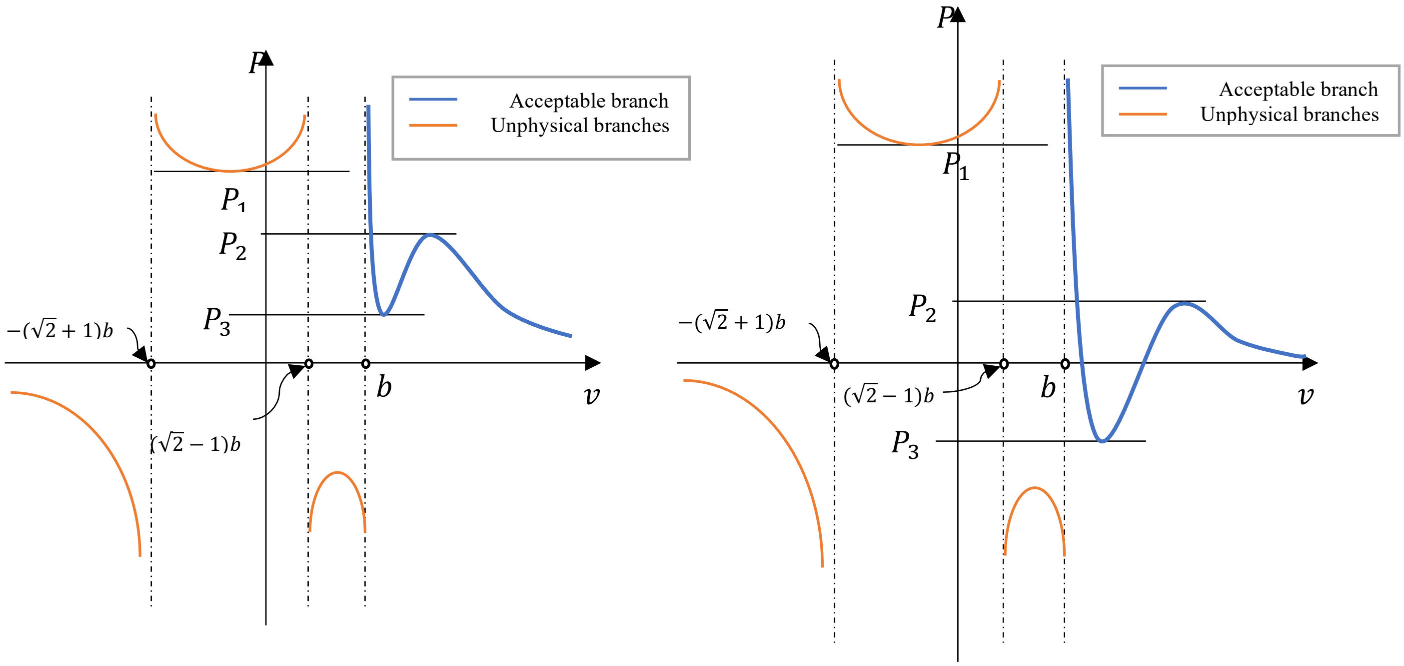

(a)

(b)

Figure 3-1: Algebraic behavior and various branches of cubic and CPA EOSs: a) without negative pressure possibility, and b) with negative pressure.

Figure 3-2 illustrates the algebraic form of LBM based EOS (e.g., SS and SC EOSs) for $T < T_c$. Both EOSs have a vertical asymptote at $v = 0$, implying that the volume of particles is neglected. Both EOSs are not considerably affected upon changing their parameters, keeping their low flexibility/potential in predicting thermodynamic properties of fluids. Additionally, the negative pressure is not calculated by LBM based EOS.

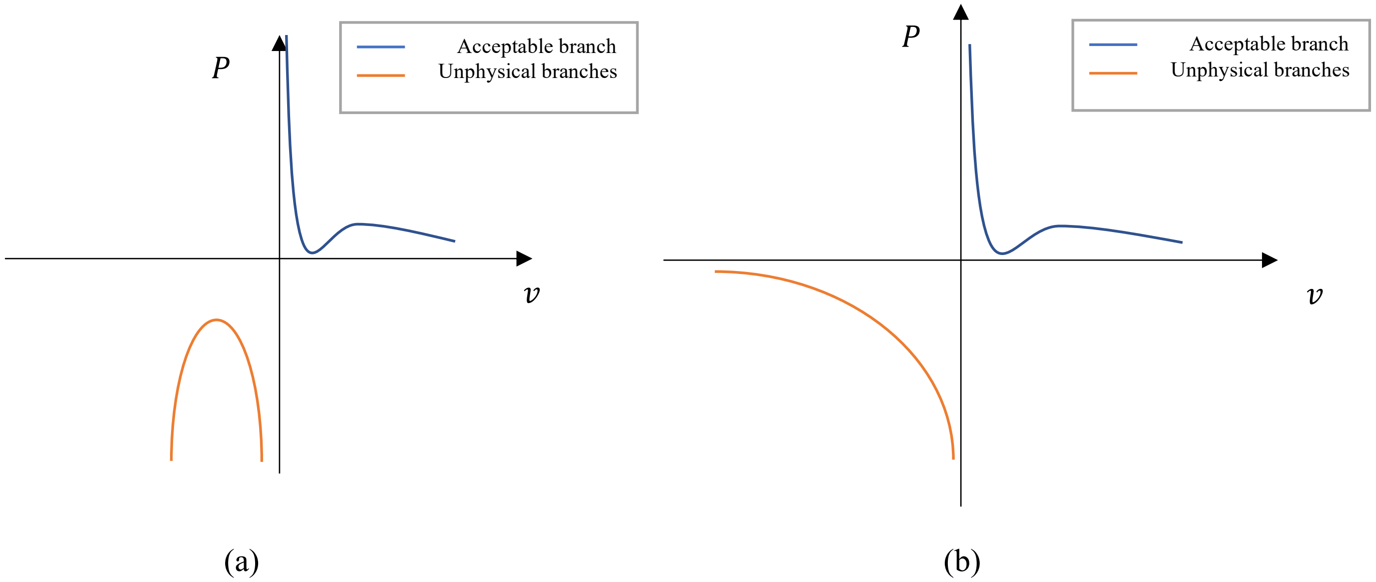

Figure 3-2: Various branches of a) SS and b) SC EOSs.

More importantly, the LBM based EOS has only one parameter that can be used to fit the experimental data. Figure 3-3 presents the calculated phases density at the equilibrium condition based on the Maxwell equal area construction. According to Figure 3-3, the SS EOS proposed by Sbragaglia and Shan has a low thermodynamic consistency with the experimental data and ϵ parameter has a low influence on the reduced properties; however, a good consistency with LBM simulation results is reported. Beside the inconsistency issue of SC EOS, it leads to the same reduced properties at different magnitudes of v_0 (see Equation (3-12)). In the rest of this study, the SS and SC EOSs are not discussed for evaluation purpose.

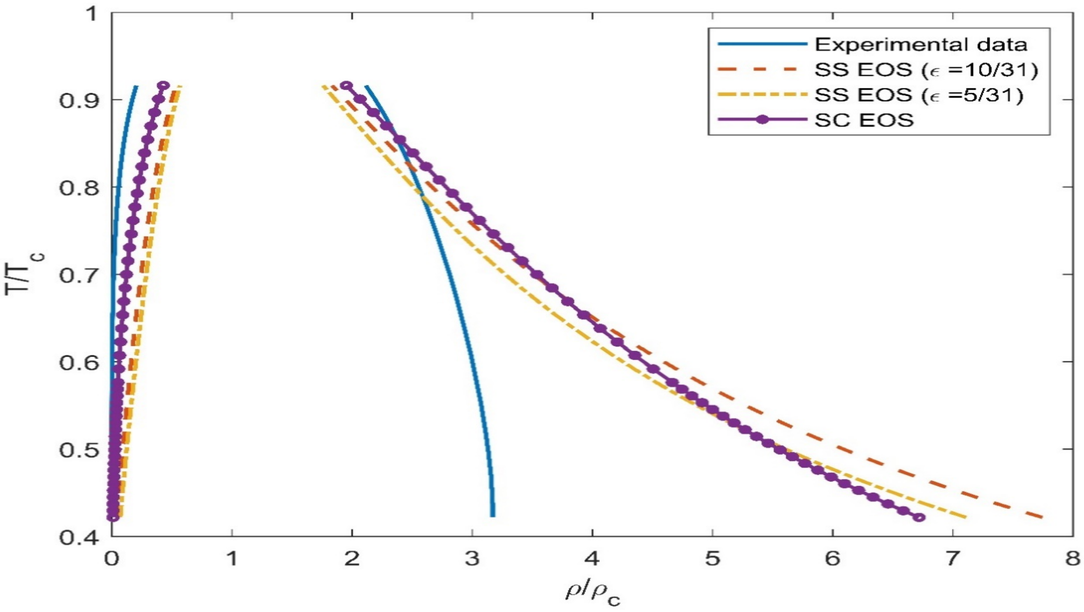

Figure 3-3: Comparison between calculated reduced density of two phases at equilibrium by EOS and experimental date (experimental data adopted from Ref [70].

Double shear layer test. To better demonstrate the dynamic properties of introduced CMs LBM, the results calculated by MRT and CMs collision operators were compared in the double shear layer test [94], which is known as an excellent candidate to examine the numerical scheme's stability [82, 95, 96]. A fully periodic 2D boundary condition with $(x, y) \in [0, L]^2$ is considered. The initial flow filed consists of two longitudinal shear layers and transvers perturbation, as superimposed below:

$$u_x = \begin{cases} u_0 \tanh\left(\kappa\left(\frac{y}{L} - \frac{1}{4}\right)\right), & \frac{y}{L} \leq \frac{1}{2} \\ u_0 \tanh\left(\kappa\left(\frac{3}{4} - \frac{y}{L}\right)\right), & \frac{y}{L} > \frac{1}{2} \end{cases} \tag{3-51}$$

and

$$u_y = u_0 \delta \sin\left(2\pi\left(\frac{x}{L} + \frac{1}{4}\right)\right) \quad (3\text{-}52)$$

where $\kappa = 80$ and $\delta = 0.05$. Fluid dynamics predicts the sheer layers and the generation of two controlling vortices based on the Kelvin-Helmotz instability mechanism. The Reynolds number is $Re = u_0 L/v = 3 \times 10^4$ and Mach number is assumed to be $Ma = u_0/c_s = 0.57$. The simulation is performed when $L = 256$ and sixth-order Hermite polynomial is implemented for central moments based LBM. Figure 3-4 duplicates the mean kinetic energy (normalized by u_0) versus time for both central moments-based LBM and MRT. In the sixth-order Hermit polynomial case of central moments-based LBM, its performance is stable while it becomes unstable at early stages in the MRT case.

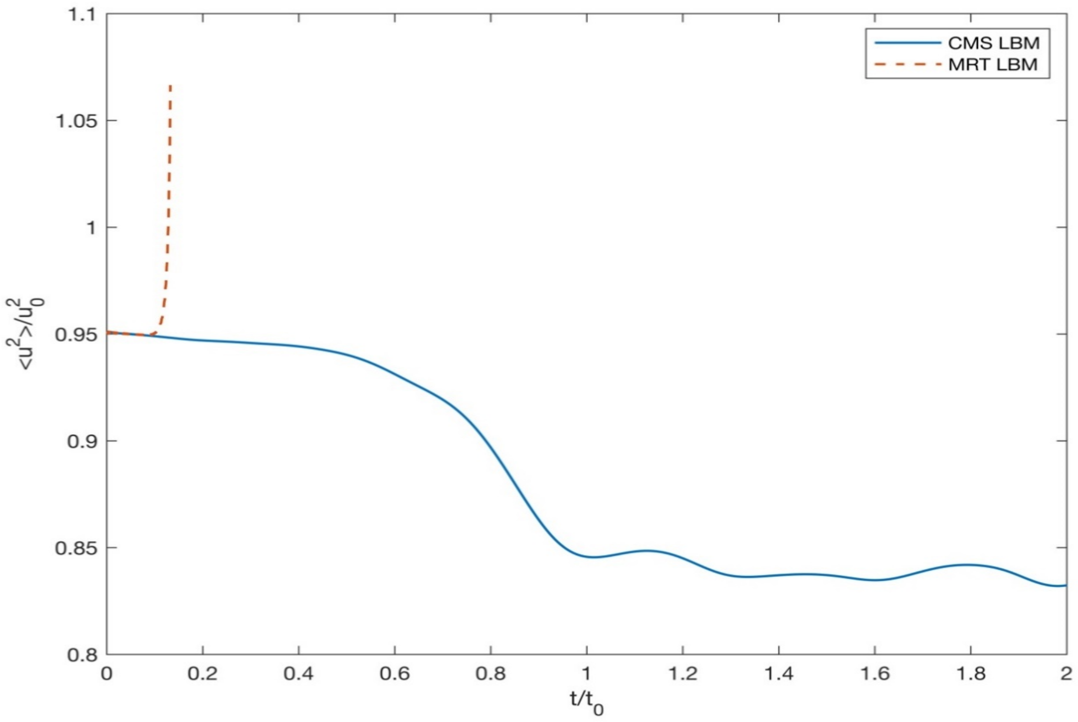

Figure 3-4: Double shear layer: comparison of time evolution of the normalized mean energy at $Ma = 0.57$ when the central moments-based LBM (solid line) and MRT (dash line) are implemented.

Spurious velocity. To investigate spurious velocity, a static single-component bubble is placed in a 2D computational domain. A 100×100 lattice computational domain with a periodic boundary condition in all directions are considered in all tests. Initially, a droplet with a radius of $R_0 = 30$ is placed in the center of the domain with the vapor (liquid) phase outside (inside) the droplet. The initial phases density is selected based on the equilibrium phase density calculated by Maxwell construction and its initial distribution, as determined below:

$$\begin{aligned}\rho(x,y) = {} & \frac{\rho_{liquid} + \rho_{gas}}{2} \\ & - \frac{\rho_{liquid} - \rho_{gas}}{2}\left[\tanh\left(\frac{2\sqrt{(x-x_c)^2 - (y-y_c)^2} - R_0}{w}\right)\right]\end{aligned} \tag{3-53}$$

where w refers to the initial interface thickness; x_c and y_c are the droplet center position; and R_0 is the initial droplet radius. Following the approach by Asadi and Zendehboudi [74], a new stability condition is applied. PR and CPA EOSs' parameters are selected as $R = 1$, $a = 2/49$, $b = 2/21$, $\omega = 0.344$, $\epsilon^{AB} = 0.1636$, and $\beta = 0.0973$.

The spurious velocity, also known as parasite current, is referred to the unphysical circular velocities near multiphase interface, which appears in the numerical simulations such as Level-set, Volume of fluid (VOF), and LBM [97]. The spurious velocity reduces the accuracy of the simulation and cannot be distinguished from the actual velocity, leading to instability problems in severe cases. The spurious velocity and surface tension are related to each other. High spurious velocity is one of the major drawbacks of the pseudopotential LBM, compared to the other LBM approaches such as free-energy LBM method. In general, higher spurious velocities are observed at high density ratios (lower temperature for single-component simulation cases) and low viscosities [33, 70].

In spite of MRT, central-moment-based LBM does not involve freely adjustable relaxation times; therefore there is no need to tune the free parameters. Figure 3-5 shows the spurious velocity at the steady-state condition calculated by the central-moment-based LBM. A dramatic decrease in the maximum spurious velocity is notable (up to 34 percent) by increasing the anisotropy order of the gradient operator, which indicates the enhancement in the stability method. In the higher anisotropy of gradient operators such as 8th order of gradient operator, more neighbour lattice nodes are considered in the simulation. Hence, a wider interfacial thickness (e.g., lower interfacial tension) may cause some instabilities, particularly in low kinematic viscosities. To increase the interfacial tension, the attraction parameter (a) is increased. Following the procedure introduced by Asadi and Zendehboudi [74], the association parameters are updated for the new case, which are $\omega = 0.344$, $\epsilon^{AB} = 0.3410$, and $\beta = 0.0887$ as the acentric factor and new association parameters in the CPA EOS for water. The reduced temperature is kept constant for all simulation runs.

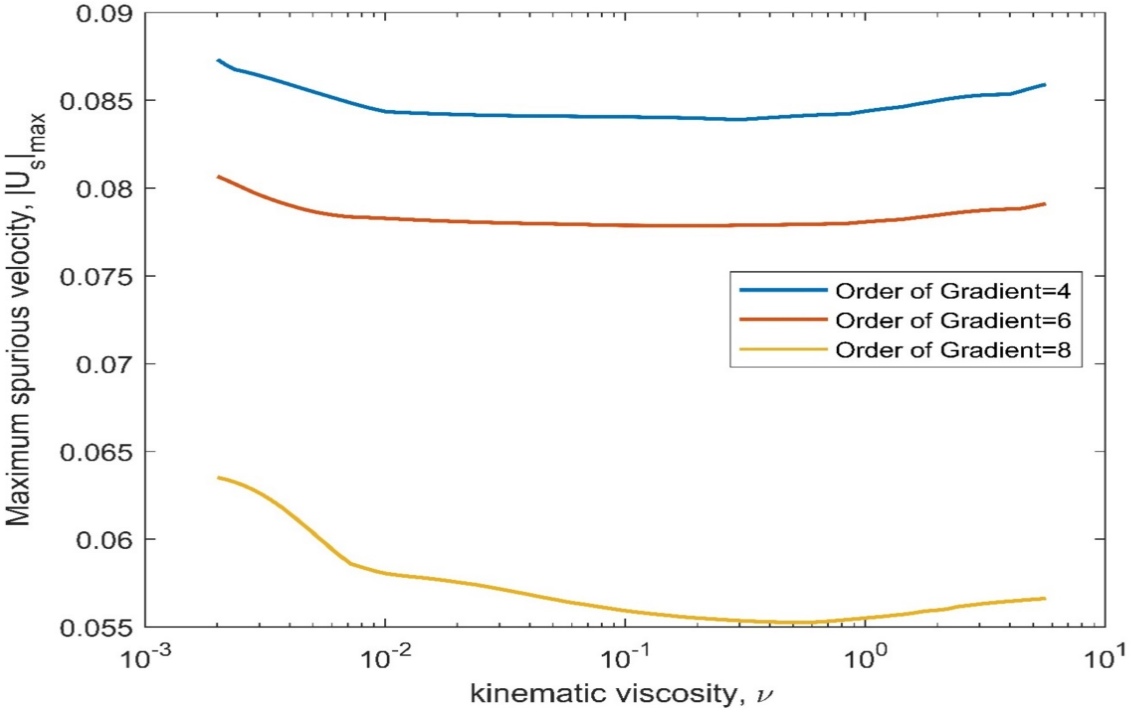

Figure 3-5: Maximum spurious velocity $|U_s|_{max}$ at the steady state condition versus kinematic viscosity of fluid (ν). For 4th and 6th order of gradient operator, the maximum spurious velocity is calculated at $a = 2/49$, $b = 2/21$, $R = 1$, and $T_r = 0.9$. For 8th case, the attractive term in the EOS is changed to $a = 4/49$.

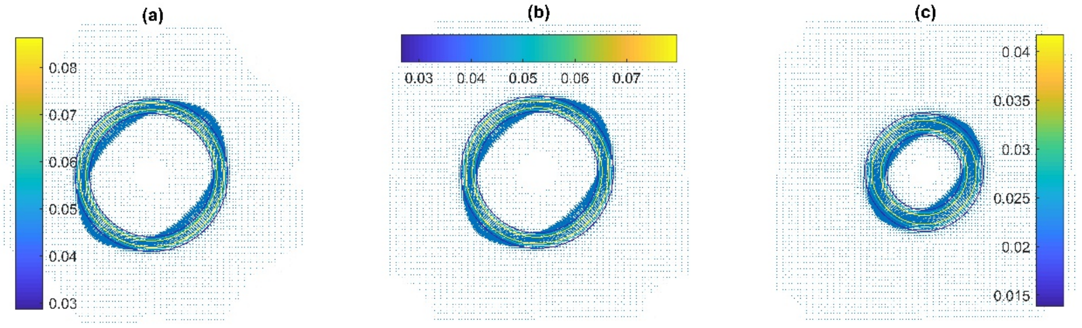

Figure 3-6: Velocity field and contour for a static droplet on the basis of different anisotropy orders of gradient operator: a) 4th, b) 6th , and c) 8th. CPA EOS is implemented in the central-moments-based LBM when $a = 4/49$, $b = 2/21$, $R = 1$, $T_r = 0.9$, and $\vartheta = 1/6$.

Figure 3-6 duplicates the velocity field for central-moment-based Lattice Boltzmann at different anisotropy orders of gradient operators. For all cases, the thermodynamic parameters are the same and calculated at the equal reduce temperature and kinematic viscosity ($\vartheta = 1/6$). A decrease in the magnitude of spurious velocity occurs with increasing the anisotropy order of gradient operator. In addition, the spurious velocity contours are changed, implying alteration in the interfacial thickness; the size of the droplet is also altered. For all three cases, the initial density is same and selected based on the Maxwell constriction; however, the thermodynamic consistency of the LBM results will change by changing the anisotropy order of gradient operator. Therefore, the size of droplet will be changed to maintain equilibrium condition. The thermodynamic consistency will be further discussed in this section.

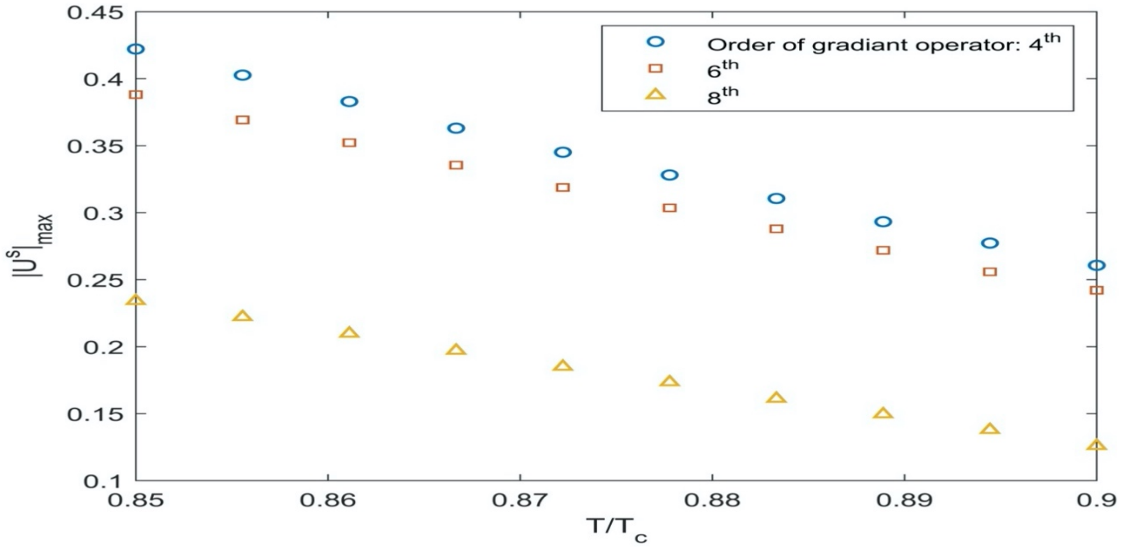

Figure 3-7: Impact of anisotropy order of gradient operator on the maximum spurious velocity at the steady state condition.

Figure 3-7 presents the influence of the anisotropy order of gradient operator on the maximum magnitude of spurious velocity at different reduced temperatures. As a general trend for all these three cases, the spurious velocity will increase as the reduced temperature is decreased. A decline in the reduced temperature leads to an increase in the density ratio (even by considering the thermodynamic inconsistency of the model) and consequently an increase in the spurious velocity.

Thermodynamic consistency. Sbragaglia and Shan [65] showed that the consistency of the pseudopotential LBM is related to ϵ. Shan [77] also concluded that ϵ is a function of anisotropy order of gradient operator (see Equation (3-13)); therefore, the anisotropy order of gradient operator affects the thermodynamic consistency. Figure 3-8 illustrates the thermodynamic consistency at various density ratio conditions while using different orders of gradient operator. The thermodynamic input parameters for the EOS are kept the same as the case utilized in Figure 3-5. As it is shown in Figure 3-6, there is a smaller liquid drop for the case with 8th order of gradient operator while all initial parameters were same for all cases; therefore, the density of the liquid phase is decreased, while the gas density is increased. In addition, the equilibrium gas density in the 8th order of gradient operator is higher than that calculated by Maxwell equal area construction. It has also a lower density for the liquid phase. To approach the equilibrium condition, the liquid phase density should be then lowered and the gas phase density should be increased when the initial densities of both phases are selected based on the Maxwell equal-area construction. This eventually causes a decrease in the droplet radius (see Figure 3-6). It should be mentioned that the liquid phase pressure in some cases will become negative that has a physical meaning (see Figure 3-1 and Refs. [89, 93]) when the attraction parameter is fixed at $a = 4/49$. The thermodynamic inconsistency is notable; however, Li et al. suggested a method to improve the thermodynamic consistency by improving the forcing scheme [66].

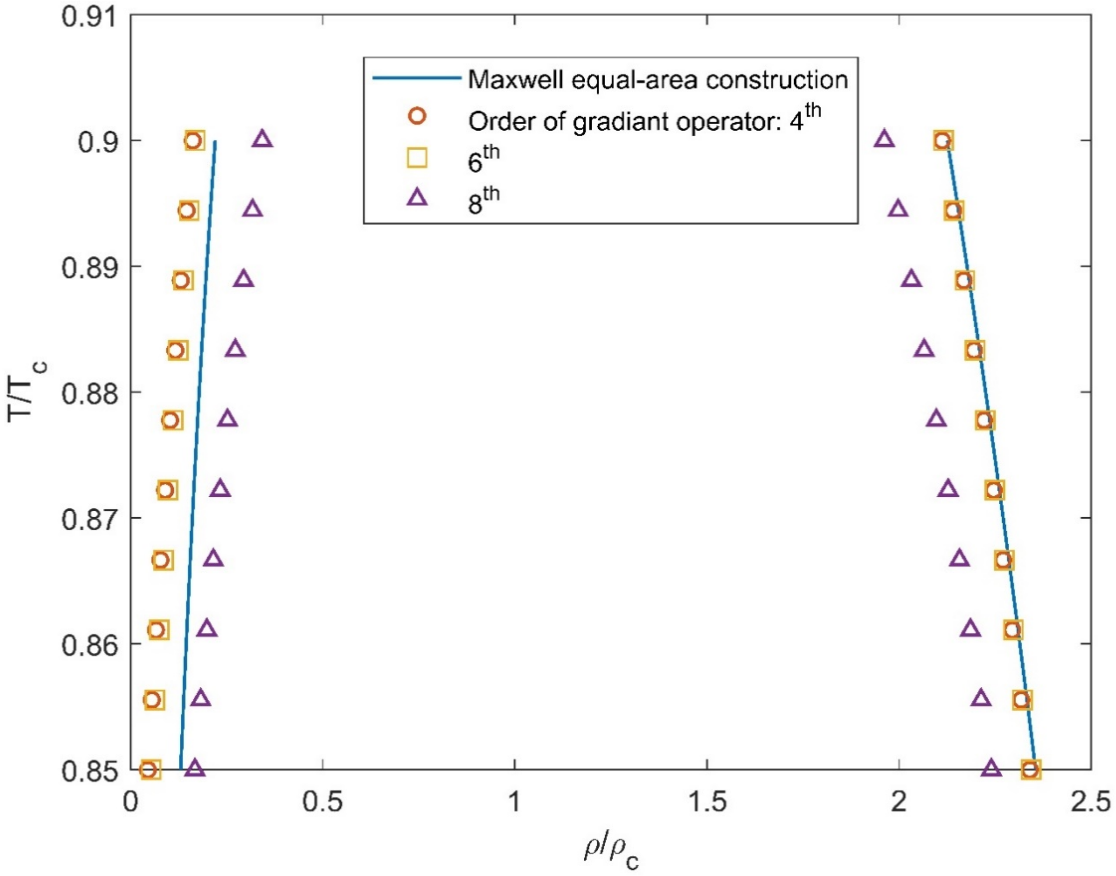

Figure 3-8: Thermodynamic consistency of the central-moments-based LBM at different anisotropy orders of gradient operator.

A higher anisotropy order of gradient operator makes possible simulation of a multiphase fluid with a higher density ratio (lower reduced temperatures for single component multiphase cases), while employing the pseudopotential central-moments-based LBM. As the reduced temperature is decreased, the interfacial tension will be increased. Hence, there is no need to increase the interfacial tension by increasing the attraction term in the CPA EOS. Despite the mid-range approach, there is no direct parameter to tune the interfacial tension/thickness [68, 98, 99], while tuning the EOS input parameters is a strategy to tune the interfacial tension/thickness. However, changing the EOS input parameters may affect the thermodynamic consistency.

Laplace law test. Laplace law test is performed by placing a static droplet in the fully periodic domain. The initial densities are selected based on the Maxwell equal-area construction. After reaching the defined steady-state condition, the pressure can be calculated by EOS. Figure 3-9duplicates a scaled image of density at the steady-state condition. As stated by Mukherjee et al., the exact location of droplet edge is uncertain [100]. Therefore, a subpixel edge location based on partial area effect that is an image processing technique is implemented to increase the accuracy of droplet radius determination [101]. The droplet edge is determined by the red circles in Figure 3-9. The inner plot shows the pressure trend along the cross section (red line). The horizontal parts determine the pressure of bulk phases. The difference between two phases pressure is related to Laplace pressure. The pressure trend between two phases is because of the unstable part of the EOS with $\left(\frac{\partial \mathrm{p}}{\partial \mathrm{v}}\right)_{\mathrm{T}} > 0$. The pressure difference versus the inverse of droplet radius is presented in Figure 3-10. According to Figure 3-10, the pressure difference increases with lowering the radius. All cases are simulated when $a = 2/49$, $b = 2/21$, and $T_r = 0.9$. A linear relationship between the pressure difference Δp and inverse of droplet radius is observed as given by Laplace law below:

$$\Delta p = \frac{\sigma}{R} \tag{3-54}$$

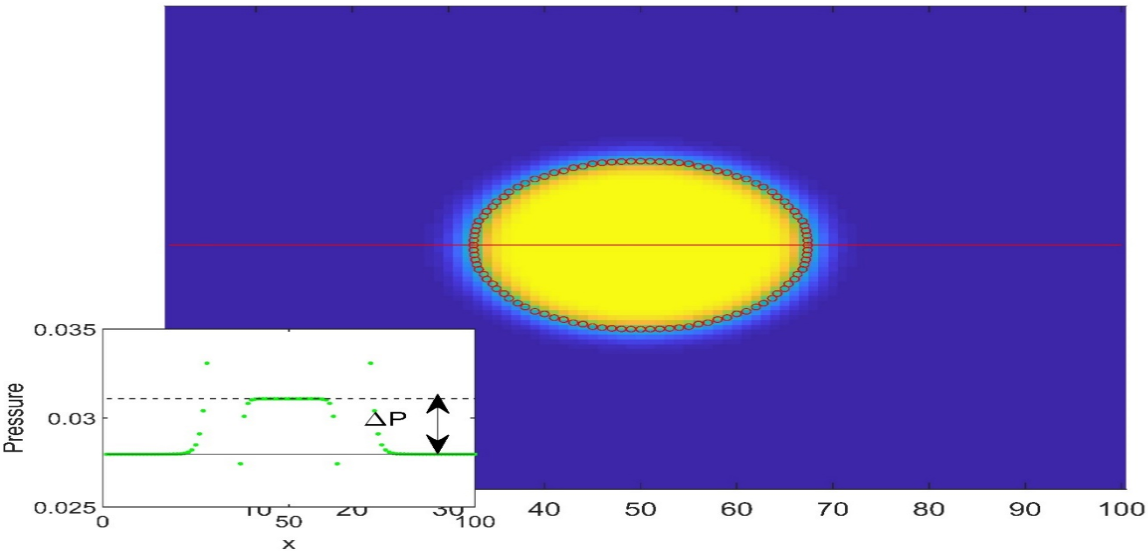

Figure 3-9: Density image and pressure variation along a cross line. Red circles are the droplet edge. Inset plot depicts the pressure distribution along the red line.

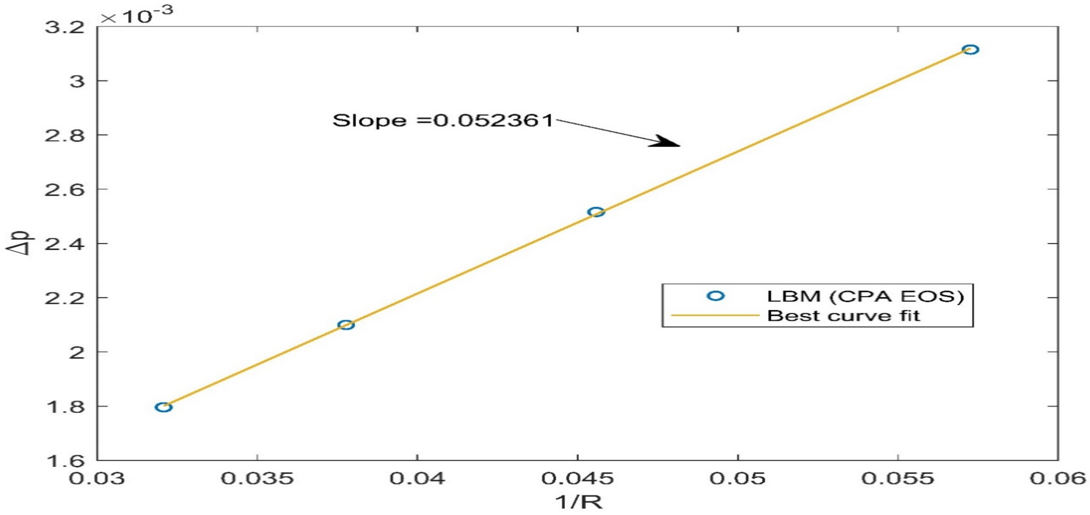

Figure 3-10: The pressure difference Δp versus inverse radius of droplet $1/R$.

Water is an important associating fluid in various biological, energy, and environment processes/systems. Accurate simulation of thermodynamic and physical properties of associating fluids including water can assist to better model, design, operate, and optimize the corresponding processes in terms of theoretical and practical prospects.

3.4 SUMMERY AND CONCLUSIONS

We introduce a pseudopotential central moments-based lattice Boltzmann method (LBM). Cubic plus association equation of state (CPA EOS) is implemented in the model to take into account the association forces in fluids with hydrogen bounds. The following main conclusions can be made based on the results of the current study:

- Shan and Chen (SC) Sbragaglia and Shan (SS) EOSs do not have sufficient flexibility to predict the fluid phase behaviors. By changing their parameters their behaviour of predicting two phase densities do not change considerably (see Figure 3-3).
- Double shear layer test shows that central moments-based LBM with a high-order Hermite polynomial are more stable than multiple-relaxation-time (MRT) collision operator-based LBM at turbulent cases. Thus, the central moments-based LBM is more suitable to be used for simulating high Reynolds and Mach number cases.
- Increasing the order of gradient operator will increase the stability of model in two-phase cases in terms of reduction of the spurious velocity.
- The gradient operator may lead to variations in the calculated interfacial tensions (capillary pressures) which can be manipulated by EOSs parameters.

- The type of the gradient operator may influence the thermodynamic consistency of the model.
- Observing a straight line in the capillary test can be considered as a proper approach for verifying the model.

The capability/potential of the current model to handle high-velocity cases and model the surface adsorption occurrence is an asset to effectively simulate transport phenomena in low permeable porous media. Further studies are recommended to investigate vital aspects such as computational costs, stability, and applicability ranges of various categories of LBM that can make easier implications of LBM in energy, environment, and health systems.

CONFLICTS OF INTEREST

There are no conflicts to declare.

ACKNOWLEDGMENTS

The authors would like to thank Memorial University, InnovateNL, and the Natural Sciences and Engineering Research Council of Canada (NSERC) for the financial assistance of this research project.

REFERENCES

1. Aidun, C.K. and J.R. Clausen, *Lattice-Boltzmann method for complex flows.* Annual review of fluid mechanics, 2010. **42**: p. 439-472.

2. Chen, S. and G.D. Doolen, *Lattice Boltzmann method for fluid flows.* Annual review of fluid mechanics, 1998. **30**(1): p. 329-364.
3. Succi, S., *The lattice Boltzmann equation: for fluid dynamics and beyond*. 2001: Oxford university press.
4. Succi, S. and S. Succi, *The Lattice Boltzmann Equation: For Complex States of Flowing Matter*. 2018: Oxford University Press.
5. Gupta, N., E. Fathi, and F. Belyadi, *Effects of nano-pore wall confinements on rarefied gas dynamics in organic rich shale reservoirs.* Fuel, 2018. **220**: p. 120-129.
6. Tao, S. and Z. Guo, *Boundary condition for lattice Boltzmann modeling of microscale gas flows with curved walls in the slip regime.* Physical Review E, 2015. **91**(4): p. 043305.
7. Yang, L., et al., *Boundary conditions with adjustable slip length for the lattice Boltzmann simulation of liquid flow.* Computers & Fluids, 2018. **174**: p. 200-212.
8. Abadi, R.H.H., A. Fakhari, and M.H. Rahimian, *Numerical simulation of three-component multiphase flows at high density and viscosity ratios using lattice Boltzmann methods.* Physical Review E, 2018. **97**(3): p. 033312.
9. Chen, L., et al., *A critical review of the pseudopotential multiphase lattice Boltzmann model: Methods and applications.* International Journal of Heat and Mass Transfer, 2014. **76**: p. 210-236.
10. Li, Q., et al., *Lattice Boltzmann methods for multiphase flow and phase-change heat transfer.* Progress in Energy and Combustion Science, 2016. **52**: p. 62-105.
11. Liu, H., et al., *Multiphase lattice Boltzmann simulations for porous media applications.* Computational Geosciences, 2016. **20**(4): p. 777-805.

12. He, Y.-L., et al., *Lattice Boltzmann methods for single-phase and solid-liquid phase-change heat transfer in porous media: A review.* International Journal of Heat and Mass Transfer, 2019. **129**: p. 160-197.

13. Arabjamaloei, R. and D. Ruth, *Numerical study of inertial effects on permeability of porous media utilizing the Lattice Boltzmann Method.* Journal of Natural Gas Science and Engineering, 2017. **44**: p. 22-36.

14. Chai, Z., et al., *Non-Darcy flow in disordered porous media: A lattice Boltzmann study.* Computers & Fluids, 2010. **39**(10): p. 2069-2077.

15. Foroughi, S., S. Jamshidi, and M.R. Pishvaie, *New Correlative Models to Improve Prediction of Fracture Permeability and Inertial Resistance Coefficient.* Transport in Porous Media, 2018. **121**(3): p. 557-584.

16. Hasert, M., J. Bernsdorf, and S. Roller. *Lattice Boltzmann simulation of non-Darcy flow in porous media*. in *ICCS*. 2011.

17. Sukop, M.C., et al., *Evaluation of permeability and non-Darcy flow in vuggy macroporous limestone aquifer samples with lattice Boltzmann methods.* Water Resources Research, 2013. **49**(1): p. 216-230.

18. Zhang, L., et al., *Consistent boundary conditions of the multiple-relaxation-time lattice Boltzmann method for convection–diffusion equations.* Computers & Fluids, 2018. **170**: p. 24-40.

19. Wang, H., et al., *Finite-difference lattice Boltzmann model for nonlinear convection-diffusion equations.* Applied Mathematics and Computation, 2017. **309**: p. 334-349.

20. Shi, B. and Z. Guo, *Lattice Boltzmann simulation of some nonlinear convection–diffusion equations.* Computers & Mathematics with Applications, 2011. **61**(12): p. 3443-3452.

21. Shi, B. and Z. Guo, *Lattice Boltzmann model for nonlinear convection-diffusion equations.* Physical Review E, 2009. **79**(1): p. 016701.

22. Shi, B., et al., *A new scheme for source term in LBGK model for convection–diffusion equation.* Computers & Mathematics with Applications, 2008. **55**(7): p. 1568-1575.

23. Lai, H. and C. Ma, *A higher order lattice BGK model for simulating some nonlinear partial differential equations.* Science in China Series G: Physics, Mechanics and Astronomy, 2009. **52**(7): p. 1053-1061.

24. Chai, Z., et al., *Lattice Boltzmann model for high-order nonlinear partial differential equations.* Physical Review E, 2018. **97**(1): p. 013304.

25. Sukop, M., *DT Thorne, Jr. Lattice Boltzmann Modeling Lattice Boltzmann Modeling*. 2006: Springer.

26. Huang, H., M. Sukop, and X. Lu, *Multiphase lattice Boltzmann methods: Theory and application*. 2015: John Wiley & Sons.

27. Guo, Z. and C. Shu, *Lattice Boltzmann method and its applications in engineering*. Vol. 3. 2013: World Scientific.

28. Bhatnagar, P.L., E.P. Gross, and M. Krook, *A model for collision processes in gases. I. Small amplitude processes in charged and neutral one-component systems.* Physical review, 1954. **94**(3): p. 511.

29. Huang, H., M. Krafczyk, and X. Lu, *Forcing term in single-phase and Shan-Chen-type multiphase lattice Boltzmann models.* Physical Review E, 2011. **84**(4): p. 046710.

30. d'Humieres, D., *Multiple–relaxation–time lattice Boltzmann models in three dimensions.* Philosophical Transactions of the Royal Society of London. Series A: Mathematical, Physical and Engineering Sciences, 2002. **360**(1792): p. 437-451.

31. Marié, S., D. Ricot, and P. Sagaut, *Comparison between lattice Boltzmann method and Navier–Stokes high order schemes for computational aeroacoustics.* Journal of Computational Physics, 2009. **228**(4): p. 1056-1070.

32. Lallemand, P. and L.-S. Luo, *Theory of the lattice Boltzmann method: Dispersion, dissipation, isotropy, Galilean invariance, and stability.* Physical Review E, 2000. **61**(6): p. 6546.

33. Yu, Z. and L.-S. Fan, *Multirelaxation-time interaction-potential-based lattice Boltzmann model for two-phase flow.* Physical Review E, 2010. **82**(4): p. 046708.

34. Li, Q., K. Luo, and X. Li, *Lattice Boltzmann modeling of multiphase flows at large density ratio with an improved pseudopotential model.* Physical Review E, 2013. **87**(5): p. 053301.

35. Geier, M., A. Greiner, and J.G. Korvink, *Cascaded digital lattice Boltzmann automata for high Reynolds number flow.* Physical Review E, 2006. **73**(6): p. 066705.

36. Premnath, K.N. and S. Banerjee, *On the three-dimensional central moment lattice Boltzmann method.* Journal of Statistical Physics, 2011. **143**(4): p. 747-794.

37. Geier, M., A. Greiner, and J.G. Korvink, *Properties of the cascaded lattice Boltzmann automaton.* International Journal of Modern Physics C, 2007. **18**(04): p. 455-462.

38. Asinari, P., *Generalized local equilibrium in the cascaded lattice Boltzmann method.* Physical Review E, 2008. **78**(1): p. 016701.

39. Geier, M., *De-aliasing and stabilization formalism of the cascaded lattice Boltzmann automaton for under-resolved high Reynolds number flow.* International journal for numerical methods in fluids, 2008. **56**(8): p. 1249-1254.

40. Geier, M., A. Greiner, and J.G. Korvink, *A factorized central moment lattice Boltzmann method.* The European Physical Journal Special Topics, 2009. **171**(1): p. 55-61.

41. Premnath, K.N. and S. Banerjee, *Incorporating forcing terms in cascaded lattice Boltzmann approach by method of central moments.* Physical Review E, 2009. **80**(3): p. 036702.

42. Geier, M., et al., *The cumulant lattice Boltzmann equation in three dimensions: Theory and validation.* Computers & Mathematics with Applications, 2015. **70**(4): p. 507-547.

43. De Rosis, A. and E. Lévêque, *Central-moment lattice Boltzmann schemes with fixed and moving immersed boundaries.* Computers & Mathematics with Applications, 2016. **72**(6): p. 1616-1628.

44. De Rosis, A., *Alternative formulation to incorporate forcing terms in a lattice Boltzmann scheme with central moments.* Physical Review E, 2017. **95**(2): p. 023311.

45. Fei, L. and K.H. Luo, *Consistent forcing scheme in the cascaded lattice Boltzmann method.* Physical Review E, 2017. **96**(5): p. 053307.

46. Geier, M., A. Pasquali, and M. Schönherr, *Parametrization of the cumulant lattice Boltzmann method for fourth order accurate diffusion part I: Derivation and validation.* Journal of Computational Physics, 2017. **348**: p. 862-888.

47. Geier, M., A. Pasquali, and M. Schönherr, *Parametrization of the cumulant lattice Boltzmann method for fourth order accurate diffusion Part II: Application to flow around a sphere at drag crisis.* Journal of Computational Physics, 2017. **348**: p. 889-898.

48. Kumar, C.S., et al., *Numerical investigations on convective heat transfer enhancement in jet impingement due to the presence of porous media using cascaded lattice Boltzmann method.* International Journal of Thermal Sciences, 2017. **122**: p. 201-217.

49. Shah, N., et al., *Cascaded collision lattice Boltzmann model (CLBM) for simulating fluid and heat transport in porous media.* Numerical Heat Transfer, Part B: Fundamentals, 2017. **72**(3): p. 211-232.

50. Sharma, K.V., R. Straka, and F.W. Tavares, *New Cascaded Thermal Lattice Boltzmann Method for simulations of advection-diffusion and convective heat transfer.* International Journal of Thermal Sciences, 2017. **118**: p. 259-277.

51. Fei, L. and K.H. Luo, *Cascaded lattice Boltzmann method for thermal flows on standard lattices.* International Journal of Thermal Sciences, 2018. **132**: p. 368-377.

52. Fei, L. and K.H. Luo, *Cascaded lattice Boltzmann method for incompressible thermal flows with heat sources and general thermal boundary conditions.* Computers & Fluids, 2018. **165**: p. 89-95.

53. Fei, L., K.H. Luo, and Q. Li, *Three-dimensional cascaded lattice Boltzmann method: Improved implementation and consistent forcing scheme.* Physical Review E, 2018. **97**(5): p. 053309.

54. Geier, M. and A. Pasquali, *Fourth order Galilean invariance for the lattice Boltzmann method.* Computers & Fluids, 2018. **166**: p. 139-151.

55. De Rosis, A., *Nonorthogonal central-moments-based lattice Boltzmann scheme in three dimensions.* Physical Review E, 2017. **95**(1): p. 013310.

56. Rosis, A.D., R. Huang, and C. Coreixas, *Universal formulation of central-moments-based lattice Boltzmann method with external forcing for the simulation of multiphysics phenomena.* Physics of Fluids, 2019. **31**: p. 117102.

57. Grunau, D., S. Chen, and K. Eggert, *A lattice Boltzmann model for multiphase fluid flows.* Physics of Fluids A: Fluid Dynamics, 1993. **5**(10): p. 2557-2562.

58. Gunstensen, A.K., et al., *Lattice Boltzmann model of immiscible fluids.* Physical Review A, 1991. **43**(8): p. 4320.

59. Shan, X. and H. Chen, *Simulation of nonideal gases and liquid-gas phase transitions by the lattice Boltzmann equation.* Physical Review E, 1994. **49**(4): p. 2941.

60. Shan, X. and H. Chen, *Lattice Boltzmann model for simulating flows with multiple phases and components.* Physical Review E, 1993. **47**(3): p. 1815.

61. Swift, M.R., W. Osborn, and J. Yeomans, *Lattice Boltzmann simulation of nonideal fluids.* Physical review letters, 1995. **75**(5): p. 830.

62. Swift, M.R., et al., *Lattice Boltzmann simulations of liquid-gas and binary fluid systems.* Physical Review E, 1996. **54**(5): p. 5041.

63. He, X., S. Chen, and R. Zhang, *A lattice Boltzmann scheme for incompressible multiphase flow and its application in simulation of Rayleigh–Taylor instability.* Journal of Computational Physics, 1999. **152**(2): p. 642-663.

64. Liu, H., A.J. Valocchi, and Q. Kang, *Three-dimensional lattice Boltzmann model for immiscible two-phase flow simulations.* Physical Review E, 2012. **85**(4): p. 046309.

65. Sbragaglia, M. and X. Shan, *Consistent pseudopotential interactions in lattice Boltzmann models.* Physical Review E, 2011. **84**(3): p. 036703.

66. Li, Q., K.H. Luo, and X. Li, *Forcing scheme in pseudopotential lattice Boltzmann model for multiphase flows.* Physical Review E, 2012. **86**(1): p. 016709.

67. Sbragaglia, M., et al., *Generalized lattice Boltzmann method with multirange pseudopotential.* Physical Review E, 2007. **75**(2): p. 026702.

68. Falcucci, G., S. Ubertini, and S. Succi, *Lattice Boltzmann simulations of phase-separating flows at large density ratios: the case of doubly-attractive pseudo-potentials.* Soft Matter, 2010. **6**(18): p. 4357-4365.

69. Shan, X., *Analysis and reduction of the spurious current in a class of multiphase lattice Boltzmann models.* Physical Review E, 2006. **73**(4): p. 047701.

70. Yuan, P. and L. Schaefer, *Equations of state in a lattice Boltzmann model.* Physics of Fluids, 2006. **18**(4): p. 042101.

71. Peng, D.-Y. and D.B. Robinson, *A new two-constant equation of state.* Industrial & Engineering Chemistry Fundamentals, 1976. **15**(1): p. 59-64.

72. Soave, G., *Equilibrium constants from a modified Redlich-Kwong equation of state.* Chemical engineering science, 1972. **27**(6): p. 1197-1203.

73. Kontogeorgis, G.M., et al., *Ten years with the CPA (Cubic-Plus-Association) equation of state. Part 1. Pure compounds and self-associating systems.* Industrial & engineering chemistry research, 2006. **45**(14): p. 4855-4868.

74. Asadi, M.B. and S. Zendehboudi, *Hybridized method of pseudopotential lattice-Boltzmann and cubic-plus-association equations of state assess thermodynamic characteristics of associating fluids.*

75. Kontogeorgis, G.M., et al., *An equation of state for associating fluids.* Industrial & engineering chemistry research, 1996. **35**(11): p. 4310-4318.

76. Wolfram, S., *Cellular automaton fluids 1: Basic theory.* Journal of statistical physics, 1986. **45**(3-4): p. 471-526.

77. Shan, X., *Pressure tensor calculation in a class of nonideal gas lattice Boltzmann models.* Physical Review E, 2008. **77**(6): p. 066702.

78. Benzi, R., et al., *Mesoscopic modeling of a two-phase flow in the presence of boundaries: the contact angle.* Physical Review E, 2006. **74**(2): p. 021509.

79. Premnath, K.N. and J. Abraham, *Three-dimensional multi-relaxation time (MRT) lattice-Boltzmann models for multiphase flow.* Journal of Computational Physics, 2007. **224**(2): p. 539-559.

80. Lallemand, P. and L.-S. Luo, *Theory of the lattice Boltzmann method: Acoustic and thermal properties in two and three dimensions.* Physical review E, 2003. **68**(3): p. 036706.

81. Malaspinas, O., *Increasing stability and accuracy of the lattice Boltzmann scheme: recursivity and regularization.* arXiv preprint arXiv:1505.06900, 2015.

82. Coreixas, C., et al., *Recursive regularization step for high-order lattice Boltzmann methods.* Physical Review E, 2017. **96**(3): p. 033306.

83. Coreixas, C.G., *High-order extension of the recursive regularized lattice Boltzmann method*. 2018.

84. De Rosis, A. and K.H. Luo, *Role of higher-order Hermite polynomials in the central-moments-based lattice Boltzmann framework.* Physical Review E, 2019. **99**(1): p. 013301.

85. Huang, R., H. Wu, and N.A. Adams, *Eliminating cubic terms in the pseudopotential lattice Boltzmann model for multiphase flow.* Physical Review E, 2018. **97**(5): p. 053308.

86. Guo, Z., C. Zheng, and B. Shi, *Discrete lattice effects on the forcing term in the lattice Boltzmann method.* Physical Review E, 2002. **65**(4): p. 046308.

87. Lopez-Echeverry, J.S., S. Reif-Acherman, and E. Araujo-Lopez, *Peng-Robinson equation of state: 40 years through cubics.* Fluid Phase Equilibria, 2017. **447**: p. 39-71.

88. Péneloux, A., E. Rauzy, and R. Fréze, *A consistent correction for Redlich-Kwong-Soave volumes.* Fluid phase equilibria, 1982. **8**(1): p. 7-23.

89. Firoozabadi, A., *Thermodynamics and applications in hydrocarbon energy production*. 2016: McGraw-Hill Education New York.

90. Huang, S.H. and M. Radosz, *Equation of state for small, large, polydisperse, and associating molecules.* Industrial & Engineering Chemistry Research, 1990. **29**(11): p. 2284-2294.

91. Khajepor, S., J. Wen, and B. Chen, *Multipseudopotential interaction: a solution for thermodynamic inconsistency in pseudopotential lattice Boltzmann models.* Physical Review E, 2015. **91**(2): p. 023301.

92. Colosqui, C.E., et al., *Mesoscopic simulation of non-ideal fluids with self-tuning of the equation of state.* Soft Matter, 2012. **8**(14): p. 3798-3809.

93. Skuse, B., A. Firoozabadi, and H.J. Ramey Jr, *Computation and Interpretation of Capillary Pressure From a Centrifuge (includes associated papers 24962 and 25291).* SPE formation evaluation, 1992. **7**(01): p. 17-24.

94. Minion, M.L. and D.L. Brown, *Performance of under-resolved two-dimensional incompressible flow simulations, II.* Journal of Computational Physics, 1997. **138**(2): p. 734-765.

95. Dellar, P.J., *Lattice Boltzmann algorithms without cubic defects in Galilean invariance on standard lattices.* Journal of Computational Physics, 2014. **259**: p. 270-283.

96. Mattila, K.K., P.C. Philippi, and L.A. Hegele Jr, *High-order regularization in lattice-Boltzmann equations.* Physics of Fluids, 2017. **29**(4): p. 046103.

97. Aulisa, E., S. Manservisi, and R. Scardovelli, *A novel representation of the surface tension force for two-phase flow with reduced spurious currents.* Computer Methods in Applied Mechanics and Engineering, 2006. **195**(44-47): p. 6239-6257.

98. Falcucci, G., et al., *Lattice Boltzmann models with mid-range interactions.* Commun. Comput. Phys, 2007. **2**(6): p. 1071-1084.

99. Falcucci, G., et al., *Lattice Boltzmann methods for multiphase flow simulations across scales.* Communications in Computational Physics, 2011. **9**(2): p. 269-296.

100. Mukherjee, S., P. Berghout, and H.E. Van den Akker, *A lattice Boltzmann approach to surfactant-laden emulsions.* AIChE Journal, 2018.

101. Trujillo-Pino, A., et al., *Accurate subpixel edge location based on partial area effect.* Image and Vision Computing, 2013. **31**(1): p. 72-90.

4. CHAPTER FOUR

Advances in Surface Wettability simulation: Implementation of Multi-Range Pseudopotential Lattice Boltzmann Method, Central Moments Collision Operator, and New Contact Angle Measuring Technique

Preface

A version of this manuscript is in the review process. Asadi, M.B. is the primary author of this paper. Along with the co-authors (De Rosis, A., and Zendehboudi, S.), Asadi developed the conceptual Lattice Boltzmann model and designed the manuscript's structure. Most of the literature review, data collection, and the performance comparison of different methods were done by Asadi, M.B., as the first author. The first draft and revised version of the manuscript were prepared by the first author based on the co-authors' feedback and comments received from journal reviewers. De Rosis, A. provided the central moments part and helped in explaining the results. The co-author, Zendehboudi, S., had the supervision role and edited the manuscript.

ABSTRACT

Surface wettability is an important characteristic that considerably affects fluid flow and distribution in both porous and non-porous systems. Lattice Boltzmann Method (LBM) is known as a promising mesoscale approach to simulate multiphase systems. Considering vital mechanisms of surface wettability, such as disjoining pressure and surface adsorption, will help to better design and operate multiphase systems. In this paper, the wettability and adsorption behaviors of a solid surface are studied by the LBM. Multi-range solid-fluid (SF) interaction in pseudopotential LBM is implemented to simulate surface wettability condition and adsorption behavior, independently. A new strategy based on the *Smoothing Splines* technique is employed to determine the contact angle through the non-constant curvature of the interface profile. The proposed method is based on the non-constant curvature shape of interface; therefore, it can capture the effects of disjoining pressure. Furthermore, the introduced SF interaction is able to simulate highly non-wetting cases at high-density ratios. The absorption layer may cause an error in the phase density detection. The importance of density probability to obtain phase density is also shown. A limited range of dynamic viscosity is one of the significant limitations of the single relaxation-time collision operator; this drawback is addressed in this research by implementing multi relaxation time (MRT) and central momentums collision operators and comparing the results. The surface wettability modeling approach introduced in this study is useful to attain more accurate and reliable results while simulating multiphase flow in the porous media and thermodynamic behavior of fluids in shale reserves.

Keywords: Wettability; Lattice Boltzmann Method (LBM); Solid-Fluid (SF) Interaction; Disjoining Pressure; Contact Angle.

4.1 INTRODUCTION

Spreading of a liquid on a solid surface plays an essential role in various processes/phenomena such as lubrication and corrosion [1, 2], surface decontamination [3], enhanced oil recovery (EOR) [4-6], bubble detachment from the boiling systems [7, 8], and carbon capture and storage (CCS) [9, 10]. The wetting behavior is determined by the balance between the cohesive and adhesive forces. The cohesive force is the reason for the droplet detaching and ball up, while the adhesive force helps to spread the droplet on the surface. The contact angle quantifies the surface wettability of a solid by a liquid droplet. A large contact angle ($\theta > 90$) shows the low wettability of the solid surface, and a small contact angle ($\theta < 90$) indicates the high wettability of the surface [11-13]. In most cases, when a complex boundary condition is presented, it appears necessary to rely on numerical simulation approaches to obtain quantitative results. To date, there are three common numerical techniques in this field. The hydrodynamical description is the first approach [14-16], which enables evaluating the spatial and frequency up to the common hydrodynamical scale (e.g., macroscale problems, pipelines, and ships). The difficulty in the definition of different solid properties, with intricate surface roughness and physical-chemical properties, is the main disadvantage of this method. An atomic description might be a good option to solve this issue. In the molecular dynamics (MD) simulation technique, interactions between a set of molecules are evaluated by integrating Newton's law [17, 18]. Because of the high computational cost, this method is limited to the nanometer and the femtosecond scale, which leads to a fundamental scale separation with the practical continuum phenomena [19]. This is not in the engineering interest scale. In this study, we address this problem through the third approach with a focus on the liquid-solid interaction based on the kinetic theory at the mesoscale.

The lattice Boltzmann method (LBM) represents a discretized solution of the Boltzmann equation, which can behave like a solver for the Navier-Stokes equation at the bulk scale. At the same time, it considers the microscopic interactions [20]. The LBM can be calculated in a parallel form easily due to the locality of most parts of the equations [21]. Multiple multiphase LBM models have been developed during the past two decades. The color gradient method is based on the two-component lattice-gas model [22] proposed by Gunstensen [23]. The free energy LBM model was developed to represent the phase effect by introducing a generalized equilibrium distribution function, which has a non-ideal pressure tensor term [24]. The pseudopotential model (also called as inter-particle potential [21] and Shan-Chen [20] model) was introduced by Shan and Chen to consider the nonlocal interaction between particles [25-28]. He et al. proposed an interface tracking model [29]. To the best of our knowledge, the pseudopotential model is the most widely used type of LBM (based on Google Scholar citations [30] of the first pseudopotential model paper [25]). The fundamental idea of the pseudopotential LBM model is to consider the microscopic molecular interactions at the mesoscopic scale utilizing pseudopotential, known as effective mass. The phase interface is not a mathematical boundary in the pseudopotential model due to the atomic phase separation; there is no need to apply any interface-capturing or interface tracking technique. The pseudopotential LBM model is capable of capturing the non-ideal fluid behaviors through implementing non-ideal equations of state (EOSs). The general review of the LBM can be found in the literature [20, 21, 29, 31-34]. Several studies are available to explain the interactions between substrate and fluid.

First, Martys and Chen described the solid-fluid (SF) interaction by introducing an SF interaction force [35]. The strength of the SF interaction was represented by a factor, which was used to adjust the contact angle in their study. This factor is considered as a density while it was assumed later to be pseudopotential [36-38]. Benzi et al. introduced $\psi(p_w)$ to adjust the contact angle [39]. Li et al. showed that the ψ-based method is suitable for high-density ratio cases; they introduced a modified pseudopotential-based SF interaction method to simulate high contact angle ranges [40]. Hu et al. [41] also presented an approach to predetermine the contact angle based on a geometric method [42]. Their strategy vanished the adsorbed layer near the solid surface [43]. Colosqui et al. used an SF interaction form, which contains repulsive core and attraction tails that leads to disjoining pressure [44]. Furthermore, Huang et al. [45] and Bao and Schaefer[46] used the pseudopotential multi-component method to approximate the contact angle.

Most of the aforementioned studies used curve fitting techniques to fit a circle to the droplet. This method is acceptable for droplets with a constant curvature, while the disjoining pressure will change the curvature of the droplet [47]. Form the experimental prospect, Samoila and Sirghi found that the presence of disjoining pressure causes an inflection point in the interface profile, implying that the curvature of the drop profile is not always a constant value [48]. The importance of a non-constant curvature profile on the wetting dynamic is discussed in a research work conducted by Wang[49]. The role of disjoining pressure is of great importance in many processes/phenomena such as membrane separation systems and enhanced oil recovery (EOR) operations [50]. When the curvature of the drop interface is not constant in the presence of disjoining pressure, developing a method to determine the contact angle is crucial. The axisymmetric drop shape analysis (ADSA) was introduced based on the classical Young-Laplace equation [51], which is not applicable in some cases such as non-axisymmetric drops, liquid lens systems, and electrical fields. Bateni et al. developed a polynomial fitting technique to obtain the contact angle [52]. Their approach exhibits an acceptable computational cost while its accuracy depends on the type of polynomial order and number of pixels.

Bhatnagar Gross and Krook (BGK) is the most common collision operator Which is implemented in pseudopotential LBM. It is also known as single relaxation time. With this collision operator, all populations are required to relaxed to an equilibrium state with the same rate [53]. When the single relaxation time collision operator is implemented, the simulation stability is limited at high-velocity gradient cased due to non-hydrodynamic ghost modes. Huang et al. [54] Showed that there is an inverse relationship between the highest achievable density and the viscosity of fluid when BGK collision operator is used. To simulate high Reynolds numbers cases, Multi Relaxation Time (MRT) collision operator is introduced. This collision operator is putted forward based on decomposing the collision operator as well as raw moments. Each moment is corresponded to a different hydrodynamic parameter and their fluxes which can relax at different time scales. Non-hydrodynamic modes [55] and acoustic waves [56] are damped by BGK collision operator; therefore, The Prandtl number is fixed. In MRT collision operator, one can achieve a model with adjustable Prandtl number, improved numerical stability, and able handle the modeling of complex fluids such as viscoelastic fluids [57]. In the MRT operator the Galilean invariance is also trimmed because the collision in a frame at rest. Yu and Fan applied the MRT collision operator in the pseudopotential LBM [58]. Later on, Li et al. modified this approach by utilizing an improved force scheme [59].

Recently, through shifting the lattice directions by the local fluid velocity, a novel collision kernel is proposed by Geier et al. [60]. They introduced a pyramidal hierarchical structure by developing the central moments (CMs) concept. In this operator which is known as “cascaded operator”, the post-collision state of a certain moment at a given order depends on lower-order ones. The orthogonal basis relaxes to the equilibrium state of the continuous Maxwellian distribution. Originally, an orthogonal basis of central moments is considered for the cascaded LBM. However the cascaded operator leads to overwhelming analytical formulation and practical implementation specifically in three-dimensional cases [61], this method showed a considerable stability enhancement in many cases [30, 60, 62-78]. Recently, De Rosis developed a new LBM framework based on the central moments. This method has differences compared to the cascaded scheme in two main point of views. First, a non-orthogonal basis is assumed and second, the equilibrium population is shortened by the relaxation to the discrete second-order. The non-pyramidal structure shows distinguished features in terms of stability, convergence, and accuracy [79, 80].

In this research, the Knowledge gap is covered by mainly to a strategy. First, the pseudopotential LBM is enhanced by implementing a new form of SF interaction which helps to simulate high contact angle range cases. Beside the BGK collision operator, MRT collision operator and MRT collision operator is employment. Second, a new robust approach is introduced to determine the contact angle based on a non-constant curvature shape off drop interface. This new method of contact angle measurement helps to see/capture effects of disjoining pressure. It is worth to mention that the current approach does not introduced a new parameter to implement disjoining pressure in the LBM.

The remainder of this paper is organized as follows: after the introduction, we provide a overview of LBM, and then a general description of the disjoining pressure is presented. This is followed by numerical simulation results and discussions. Lastly, the key outcomes of the current study are listed in the conclusions section.

4.2 THEORY AND METHODOLOGY

First, the LBM structure is reviewed. Three different collision operator, single relaxation time (BGK), Multi Relaxation Time (MRT), and central momentum, are reviewed, and a new SF interaction is proposed. Second, the disjoining pressure concept is overviewed. Then, a new contact angle measuring procedure is explained. Finally, the methodology to calculate the probability histogram for densities is explained.

4.2.1 Lattice Boltzmann Method (LBM)

To describe the evolution of the particle distribution function (PDF) f_i in time t and space $x = [x, y]$ which moves on a lattice structure along a direction i with velocity $c_i = [c_{xi}, c_{yi}]$ during the time step, $\Delta t = 1$, the discrete LB can be used:

$$f_i(\boldsymbol{x} + \Delta t \boldsymbol{c_i}, t + \Delta t) = f_i(\boldsymbol{x}, t) + \Omega_i(\boldsymbol{x}, t) + S_i \tag{4-1}$$

where S_i is the forcing term. The solution of discrete LB can be categorized into two steps:

$$\text{Collision:} \quad f_i^*(\boldsymbol{x}, t) = f_i(\boldsymbol{x}, t) + \Omega_i(\boldsymbol{x}, t) \tag{4-2}$$

$$\text{Streaming:} \quad f_i(\boldsymbol{x} + \Delta t \boldsymbol{c_i}, t + \Delta t) = f_i^*(\boldsymbol{x}, t) \tag{4-3}$$

in which $\Omega_i(x, t)$ refers to the collision operator and superscript $*$ stands for the post-collision quantities. The velocity vector field, $u = [u_x, u_y]$, and fluid density, ρ, are computed by zeroth and first-order momentums of the population as expressed below:

$$\rho = \sum_i f_i\,; \quad \rho u = \sum_i f_i\, \boldsymbol{c_i} \tag{4-4}$$

Single relaxation time LBM (BGK). Based on the BGK model, a single relaxation of population with the same rate to a local equilibrium is considered in the collision operator (Ω_i). The BGK collision operator is given below:

$$\Omega_i = \frac{\left(f_i^{eq} - f_i\right)}{\tau} \tag{4-5}$$

where τ symbolizes the single relaxation time scale. The single relaxation time scale is related to the kinematic viscosity, ν, of the fluid as:

$$\nu = \left(\tau - \frac{1}{2}\right) c_s^2 \Delta t \tag{4-6}$$

where $\mathrm{c_s} = 1/\sqrt{3}$ is the lattice sound speed. In Equation (4-5) f_i^{eq} is the equilibrium PDF and is given as below:

$$f_i^{eq} = w_i \rho \left[1 + 3\boldsymbol{c_i} \cdot \boldsymbol{u} + \frac{9}{2}(\boldsymbol{c_i} \cdot \boldsymbol{u})^2 - \frac{3}{2}\boldsymbol{u} \cdot \boldsymbol{u}\right] \tag{4-7}$$

in which $w_i s$ are a set of weights and are calculated based on the LB model.

Multi Relaxation time (MRT). Generally, the collision process contains multiple physical quantities that may relax on the different time scales. To include the information of different time scales, a full constant matrix (Λ) is considered instead of a single time scale, τ. Therefore, one can rewritten the collision operator as follows:

$$\Omega_i = \Sigma_j \Lambda_{ij}\left(f_j^{eq} - f_j\right) \tag{4-8}$$

Based on the Premnath and Abraham [81] derivation and by applying the transformation, $\bar{f_i} = f_i - 1/2\Delta t$, Equation (4-1) can be rewritten as following format:

$$\begin{aligned} &\bar{f_i}(\boldsymbol{x} + \Delta t\boldsymbol{c_i}, t + \Delta t) \\ &\quad = \bar{f_i}(\boldsymbol{x}, t) + \Sigma_j \Lambda_{ij}\left(f_j^{eq} - \bar{f_j}\right)|_{(x,t)} + \Sigma_j \left(I_{ij} - \frac{1}{2}\Lambda_{ij}\right) S_i|_{(x,t)} \Delta t \end{aligned} \tag{4-9}$$

where I_{ij} refers to the components of the identity matrix. A complex matrix manipulation is required to solve Equation (4-9); therefore, a linear transformation is implemented to diagonalize the collision matrix. The transformation matrix **T** transforms the distribution functions from velocity space ($\bar{f_i}$) into the moment space ($\hat{f_i}$). It is related to the macroscopic physical quantities such as density, momentum, energy, and their flux. The transformation matrix form depends on the lattice structure. The explicit form of D2Q9 is given as follows [82]:

$$\mathbf{T} = \begin{bmatrix} 1 & 1 & 1 & 1 & 1 & 1 & 1 & 1 & 1 \\ -4 & -1 & -1 & -1 & -1 & 2 & 2 & 2 & 2 \\ 4 & -2 & -2 & -2 & -2 & 1 & 1 & 1 & 1 \\ 0 & 1 & 0 & -1 & 0 & 1 & -1 & -1 & 1 \\ 0 & -2 & 0 & 2 & 0 & 1 & -1 & -1 & 1 \\ 0 & 0 & 1 & 0 & -1 & 1 & 1 & -1 & -1 \\ 0 & 0 & -2 & 0 & 2 & 1 & 1 & -1 & -1 \\ 0 & 1 & -1 & 1 & -1 & 0 & 0 & 0 & 0 \\ 0 & 0 & 0 & 0 & 0 & 1 & -1 & 1 & -1 \end{bmatrix} \tag{4-10}$$

By multiplying the transformation matrix **T**, the transformed form of Equation (4-9) into moment space can be written as below:

$$\begin{aligned} &\hat{f}_i(\boldsymbol{x} + \Delta t \boldsymbol{c_i}, t + \Delta t) \\ &= \hat{f}_i(\boldsymbol{x}, t) + \Sigma_\beta \widehat{\Lambda}_{i\beta} \left(\hat{f}_\beta^{eq} - \hat{f}_\beta \right) |_{(x,t)} + \Sigma_\beta \left(I_{i\beta} - \frac{1}{2} \widehat{\Lambda}_{i\beta} \right) \hat{S}_i |_{(x,t)} \Delta t \end{aligned} \tag{4-11}$$

Now, the transformed collision matrix $\widehat{\Lambda}_{i\beta} = \mathrm{T} \Lambda \mathrm{T}^{-1}$is diagonal as follows (for the D2Q9 lattice):

$$\widehat{\Lambda} = diag[s_1, s_2, s_3, s_4, s_5, s_6, s_7, s_8, s_9] \tag{4-12}$$

The diagonal components of $\widehat{\Lambda}$, s_1 through s_9, are the new relaxation parameters which are in associating with elements of $\hat{f}_i$.

Central Moments. The complete expression of the equilibrium distributions can be written as [83] [84, 85]:

$$f_i^{eq} = w_i\, \rho\, [1 + \frac{\boldsymbol{c_i} \cdot \boldsymbol{u}}{c_s^2} + \frac{1}{2\, c_s^4}\, \mathcal{H}_i^{(2)}$$

$$: \boldsymbol{uu} + \frac{1}{2c_s^6}\left(\mathcal{H}_{ixxy}^{(3)}\, u_x^2\, u_y + \mathcal{H}_{ixyy}^{(3)}\, u_x\, u_y^2 \right) \quad (4\text{-}13)$$

$$+ \frac{1}{4c_s^8}\, \mathcal{H}_{ixxyy}^{(4)} u_x^2\, u_y^2\,]$$

with $\mathcal{H}^{(\mathrm{n})}$ refers to the Hermite polynomial of order n. Notice that Eq.(4-13) degrades into the classical second-order truncated formula if $\mathcal{H}^{(3)}$ and $\mathcal{H}^{(4)}$ are neglected.

One can assume lattice directions shifted by the local fluid velocity (see Geier et al.[60]), $\bar{\boldsymbol{c}}_i = [|\bar{\boldsymbol{c}}_{xi}\rangle, |\bar{\boldsymbol{c}}_{yi}\rangle]$ in order to create a CMs-based collision operator, where

$$\begin{aligned} |\bar{\boldsymbol{c}}_{xi}\rangle &= |\boldsymbol{c}_{xi} - u_x\rangle \\ |\bar{\boldsymbol{c}}_{yi}\rangle &= |\boldsymbol{c}_{yi} - u_y\rangle \end{aligned} \quad (4\text{-}14)$$

To transform distributions into moments (and vice versa) the matrix $\bar{\mathcal{T}} = [\bar{T}_0, \dots, \bar{T}_i, \dots, \bar{T}_8]$ is applied (see for example De Rosis and Luo [86]) as below:

$$\begin{aligned} |\bar{T}_0\rangle &= |1, \dots, 1\rangle \\ |\bar{T}_1\rangle &= |\bar{c}_{xi}\rangle \\ |\bar{T}_2\rangle &= |\bar{c}_{yi}\rangle \\ |\bar{T}_3\rangle &= |\bar{c}_{xi}^2 + \bar{c}_{yi}^2\rangle \\ |\bar{T}_4\rangle &= |\bar{c}_{xi}^2 - \bar{c}_{yi}^2\rangle \\ |\bar{T}_5\rangle &= |\bar{c}_{xi}\bar{c}_{yi}\rangle \\ |\bar{T}_6\rangle &= |\bar{c}_{xi}^2\bar{c}_{yi}\rangle \end{aligned} \quad (4\text{-}15)$$

$$|\bar{T}_7\rangle = |\bar{c}_{xi}\bar{c}_{yi}^2\rangle$$

$$|\bar{T}_8\rangle = |\bar{c}_{xi}^2\bar{c}_{yi}^2\rangle$$

Then pre-collision and equilibrium CMs is evaluated as

$$\begin{aligned} |k_i\rangle &= \bar{\mathcal{T}}^T|f_i\rangle \\ |k_i^{eq}\rangle &= \bar{\mathcal{T}}^T\left|f_i^{eq}\right\rangle \end{aligned} \tag{4-16}$$

respectively, where

$$\begin{aligned} |k_i\rangle &= [k_0, \dots, k_i, \dots, k_8]^\top \\ |k_i^{eq}\rangle &= \left[k_0^{eq}, \dots, k_i^{eq}, \dots, k_8^{eq}\right]^\top \end{aligned} \tag{4-17}$$

and $|f_i^{eq}\rangle = \left[f_0^{eq}, \dots, f_i^{eq}, \dots, f_8^{eq}\right]^\top$ and only three equilibrium central moments are not zero:

$$\begin{aligned} k_0^{eq} &= \rho \\ k_3^{eq} &= 2\rho c_s^2 \\ k_8^{eq} &= \rho c_s^4 \end{aligned} \tag{4-18}$$

and $k_{1,2,4,5,6,7}^{eq} = 0$. Indeed, based on De Rosis and Luo [86], when the full set of Hermite polynomials is considered, the discrete equilibrium CMs and those of the continuous Maxwellian distribution are equal. By considering the $9 * 9$ relaxation matrix as $\Lambda = \text{diag}[1,1,1,1,\omega,\omega,1,1,1]$ and the $9 * 9$ unit tensor as **I,** the post-collision state in terms of central moments is[56]

$$|\, k_i^\star \,\rangle \;=\; (\mathbf{I} - \Lambda)\,\bar{\mathcal{T}}^\top|f_i\rangle + \Lambda\bar{\mathcal{T}}^\top|\, f_i^{eq}\rangle + \;(\mathbf{I} - \frac{\Lambda}{2})\bar{\mathcal{T}}^\top|\,\mathcal{F}_i\rangle \tag{4-19}$$

The last component which needs to be defined is the forcing term $\mathcal{F}_i$. Same as the approach which is used in the equilibrium distribution (see Eq.(4-13)), Huang et al. [87] suggested to expand the forcing term as

$$\mathcal{F}_i = w_i \left(\frac{F}{c_s} . \mathcal{H}^{(1)} + \frac{[Fu]}{2c_s^2} . \mathcal{H}^{(2)} + \frac{[Fuu]}{6c_s^3} . \mathcal{H}^{(3)}_{[xyy],[xxy]} + \frac{[Fuuu]}{24c_s^4} . \mathcal{H}^{(4)}_{[xxyy]} \right) \qquad (4\text{-}20)$$

where the square bracket in Hermite coefficient refers permutations. The popular formula by Guo et al. [88] is then recovered when $\mathcal{H}^{(3)}$ and $\mathcal{H}^{(4)}$ are disregarded. The central moments of the discrete force term are[56]

$$|R_i\rangle = \bar{\mathcal{T}}^T |\mathcal{F}_i\rangle \qquad (4\text{-}21)$$

where

$$\begin{aligned} |R_1\rangle &= F_x \\ |R_2\rangle &= F_y \\ |R_6\rangle &= F_y c_s^2 \\ |R_7\rangle &= F_x c_s^2 \end{aligned} \qquad (4\text{-}22)$$

and $R_{0,3,4,5,8} = 0$. Because of a different basis, the above compact expressions are different from those by Huang et al.[84]. It is worth to mention that Eq.(4-22) can also be obtained when the velocity terms in Eq(4-15) of De Rosis[69] are neglected. Truly, the concept stated by De Rosis et al.[56] is remarked, where it has been demonstrated that the adoption of the Hermite polynomials of the maximum admissible order (n=4 in the D2Q9 space according to Malaspinas[81]) leads to Galilean-invariant (or, in other words, velocity-independent) equilibrium and forcing central moments. This concise scheme leads to post-collision central moments that are (see De Rosis et al.[56]):

$$\begin{aligned} k_0^\star &= \rho \\ k_1^\star &= \frac{F_x}{2} \\ k_2^\star &= \frac{F_y}{2} \end{aligned} \qquad (4\text{-}23)$$

$$k_3^\star = 2\rho c_s^2$$

$$k_4^\star = (1-\omega)k_4$$

$$k_5^\star = (1-\omega)k_5$$

$$k_6^\star = \frac{F_y}{6}$$

$$k_7^\star = \rho c_s^4$$

Then, the post-collision populations $|f_i^\star\rangle = [f_0^\star, \dots, f_i^\star, \dots, f_8^\star]^{\mathrm{T}}$are reconstructed by applying the back-transformation (see De Rosis^{55})

$$|f_i^\star\rangle = (\bar{\mathcal{T}}^T)^{-1}|k_i^\star\rangle \tag{4-24}$$

Li et al. provides a comprehensive study for a better understanding of different forcing schemes [89].

Fluid-fluid (FF) and solid-fluid (SF) interactions. Interactions between FF and SF are simulated by the pseudopotential LBM, which was proposed by Shan and Chen [25]. The intermolecular interaction forces that lead to the phase segregation mimic the intermolecular interactions. The interaction forces are defined by the pseudopotential ψ (or effective mass) based on the local density. The interaction forces contain two FF and SF parts. The FF interaction forces for a single component multiphase case is determined as follows [90]:

$$\mathrm{F}_{\mathrm{FF}} = -G_f\psi(x)\Sigma_i\omega_i\psi(x+c_i)c_i \tag{4-25}$$

where G_f symbolizes the FF interaction strength. Based on the simple interaction force defined in Equation (4-25), the pseudopotential (ψ) can be defined with an EOS as follows [91]:

$$\psi = \sqrt{\frac{2(p_{EOS} - \rho c_s^2)}{G_f c_s}} \tag{4-26}$$

Li et al. introduced a new forcing scheme to improve the thermodynamic consistency at a higher density ratio [89]. Also, a new approach was presented to tune the surface tension in a single range multi relaxation time (MRT) method [92]. In this study, Carnahan-Starling (C-S) EOS is used. The cohesive forces are represented by Equation (4-25). To simulate the adhesive forces, the forces between the solid and fluid phases should be calculated. Martys and Chen suggested the following SF interaction [35]:

$$\mathrm{F_{SF}} = -G_w \rho(x) \Sigma_i \omega_i s(x + c_i) c_i \tag{4-27}$$

where G_w stands for the SF strength; and $s(x + e_i)$ symbolises a switch function which is equal to 0 and 1 for fluid and solid phases, respectively. The density factor introduced by Equation (4-27) is replaced by a pseudopotential, as given below [36]:

$$\mathrm{F_{SF}} = -G_w \psi(x) \Sigma_i \omega_i s(x + c_i) c_i \tag{4-28}$$

Benzi et al. introduced the wall density parameter (ρ_w) to adjust the surface wettability and to include its effect by considering the pseudopotential form, $\psi(\rho_w)$, in the SF interaction [39], as expressed below:

$$\mathrm{F_{SF}} = -G \psi(x) \Sigma_i \omega_i \psi(\rho_w) s(x + c_i) c_i \tag{4-29}$$

Li et al. updated the switch function, $s(x+e_\alpha)$, to a new switch function $S(x+e_i)=\phi(x)\,s(x+c_i)$ and by choosing $\phi(x)=\psi(x)$ introduced a new SF interaction [40] as follows:

$$\mathrm{F_{SF}} = -G_w \psi(x) \Sigma_i \omega_i S(x+c_i) c_i \tag{4-30}$$

They showed that the Benzi et al. approach can cover a smaller range of contact angle, and for high contact angle cases, the droplet will be detached from the surface; therefore, the Benzi et al. method is unable to mimic the static contact angle. Their modified SF interaction is able to simulate a wide range of static contact angles. Later on, Hu et al. [41] implemented a geometrical method proposed by Ding and Spelt [42]. They customized the density of the *ghost cells* to predetermine the contact angle. Although their technique is suitable to predetermine the contact angle, it leads to eliminate the adsorbed layer that has a physical meaning [43].

To overcome the above drawbacks, we recall the multirange potential proposed by Sbragaglia et al. [93] for SF interaction in a more general form, as shown below:

$$\mathrm{F_{SF}} = -\psi(x) \Sigma_i \Sigma_j\, G_j \omega_i S(x+jc_i) c_i \tag{4-31}$$

By choosing appropriate interaction strength constants (G_j), the attraction tail and repulsion core of SF interaction can be regenerated. To reproduce the adsorbed layer, $S(x+j*e_i)$ is chosen as $S(x+je_i)=\psi(\rho_w)s(x+je_i)$. By changing the wall density and strength parameters, the adsorption property of the solid surface can be tuned. The multirange potential implementation for SF interaction provides the opportunity to simulate high contact angle cases. Furthermore, disjoining pressure impacts can be mimicked. In the next subsection, the main equations of disjoining pressure will be provided.

4.2.2 Disjoining pressure

In this section, the concept of disjoining pressure is overviewed, and its important parameters are mentioned. The disjoining pressure concept is developed to explain the impact of surface forces on a nanoscale liquid film [94]. The different surface forces contribute to the disjoining pressure formation [94-97]. The components of disjoining pressure are listed as follows:

1- Electrical double layers and their overlap cause the electrostatic element (Π_E) of the disjoining pressure as given below:

$$\Pi_\mathrm{E} = \mathrm{RTc_0}(\exp(\varphi) + \exp(-\varphi)) - 2RTc_0 - \frac{(RT)^2\epsilon\epsilon_0}{2F^2}\left(\frac{\partial\varphi}{\partial y}\right)^2 \qquad (4\text{-}32)$$

where $\epsilon_0, \epsilon, F, T, R,$ and c_0 represent the dielectric constant of vacuum, dielectric constant of water, Faraday's constant, temperature in K, universal gas constant, and electrolyte concentration, respectively; φ and y refer to the dimensionless electric potential in F/RT unit, and coordinate normal to the liquid-gas, respectively.

2- The energy which is required to form an organized structure in the thin molecular compared to the unorganized structure in the bulk liquid of the disjoining pressure (Π_S), as expressed below [98, 99]:

$$\Pi_\mathrm{S} = \beta_1 \exp(-z/\alpha_1) + \beta_2 \exp(-z/\alpha_2) \qquad (4\text{-}33)$$

in which, α_{i} (α_1 and α_2) and β_1 (β_1 and β_2) are the constants related to the characteristic length and the magnitudes of the structural forces. The indices 1 and 2 indicate the short-range and long-range structural interactions; and *z* indicates the local thickness of the film.

3- van der Waals or molecular component of disjoining pressure is defined as follows [100]:

$$\Pi_{\mathrm{M}} = -A_{123}(4 - 3z_x^2 - 3z_{xx}z)/24\pi z^3 \qquad (4\text{-}34)$$

where A_{123} refers to the Hamaker constant for the interaction of media 1 (gas) and 3 (solid) through medium 2 (absorbed liquid film). The total disjoining pressure ($\Pi(\mathrm{z})$) can be thus described by the following expression:

$$\Pi(\mathrm{z}) = \Pi_{\mathrm{M}}(\mathrm{z}) + \Pi_{\mathrm{E}}(\mathrm{z}) + \Pi_{\mathrm{S}}(\mathrm{z}) \qquad (4\text{-}35)$$

The augmented Laplace equation is implemented to describe the shape of the liquid-gas interface as follows:

$$p_2 - p_1 = \sigma_{12}\kappa - \Pi(\mathrm{z}) \qquad (4\text{-}36)$$

where p_1 and p_2 are the pressure of the gas and liquid phases, respectively. σ_{12} introduces the superficial tension of the gas-liquid phase, and κ stands for the local curvature of gas-liquid interface. By neglecting the interconnection of $\sigma_{12}(z)$ and $\Pi(z)$ [48, 101] and considering the constant macroscopic value of σ_{12}, Equation (4-25) can be rewritten as follows:

$$\kappa = \frac{\mathrm{p_e} + \Pi(\mathrm{z})}{\sigma_{12}} \qquad (4\text{-}37)$$

where $\mathrm{p_e} = p_2 - p_1$ is the excess pressure.

4.2.3 Contact Angle Measurement

The local curvature of the liquid-gas interface can be expressed by the local thickness of the gas-liquid interface as follows:

$$\kappa = \frac{\frac{d^2h(x)}{dx^2}}{\sqrt{\left(1+\left(\frac{dh(x)}{dx}\right)^2\right)^3}} \tag{4-38}$$

where $h(x)$ represents the gas-liquid profile in the *z-x* plain (see **Error! Reference source not found.**). The solid-liquid contact angle can be defined as the extremum tilting angle that happens at the inflection point, as given below:

$$\theta_{max} = \tan^{-1}\left(\frac{dh(x)}{dx}\Big|_{@\frac{d^2h(x)}{dx^2}=0}\right) \tag{4-39}$$

In Equation (4-39), θ_{max} is the maximum tilting angle.

To calculate the contact angle, a function for a gas-liquid interface needs to be considered. In this regard, the remainder of this subsection will introduce our procedure for obtaining a function for a gas-liquid interface.

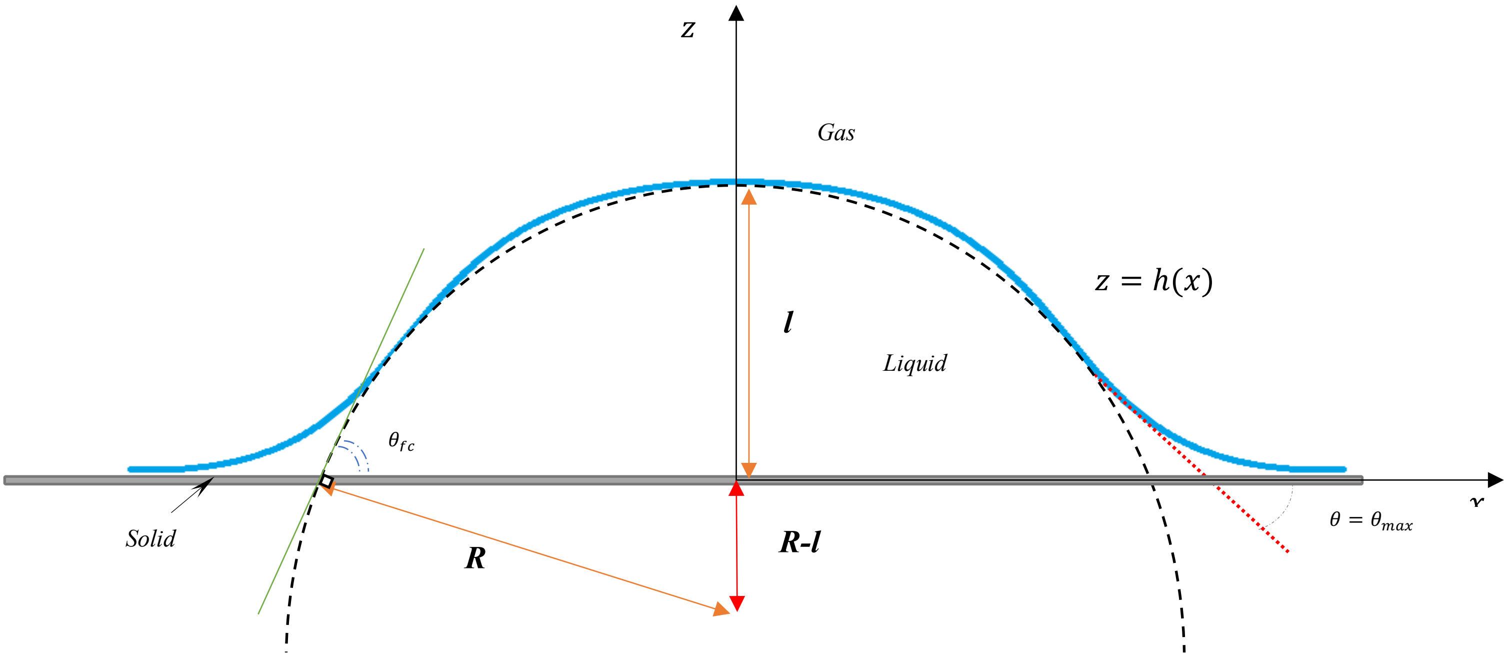

Figure 4-1: Schematic of a droplet on the solid surface.

Due to the discretizational nature of LBM, a continues function is needed to obtain the curvature of the droplet and to determine the contact angle. Initially, the interface of two phases should be defined. Colosqui et al. defined a cut-off density as the mean density of both liquid and gas phases [102]. They assumed a constant curvature of droplet shape; therefore, they fitted a circle of radius R by least squares. In this method, the equilibrium contact angle will be $\theta_{fc} = \text{acos}\,(1 - l/R)$ where l is the droplet height. Figure 4-1 shows that this measured contact angle is only accurate when the curvature is constant. Furthermore, the contact angle measurement for a dynamic case needs two fitted circles. The interface can be defined as a region with a finite width [103]. Thus, a single lattice layer would not be chosen to represent the interfacial between liquid and gas phases. The gas-liquid interface is represented by a band of lattices. It is found that the interface thickness is around 4-5 lattices [59, 104, 105]. A range of density should be selected to determine the interfacial region. When the interface of two phases is determined, data points need to be smoothed to avoid numerical noises. In this study, a robust local regression method is applied. It should be mentioned that the calculated contact angle in the current research is the apparent contact angle [49]. There are three steps to the local regression smoothing process. First, the regression weights for each data point in the span (e.g., the interval of date which is considered in the smoothing process) should be determined as follows:

$$w_i = \left(1 - \left|\frac{x - x_i}{d(x)}\right|^3\right)^3 \tag{4-40}$$

In Equation (4-40), x is the predictor value linked with the response value to be smoothed; x_i are the closest neighbors to x through the defined span; $d(x)$ denotes the distance from x along the abscissa to the most distant in predictor value in the span. Using this type of weighing, the smoothing data point has the highest weight and points outside of the span have a zero weight. Then, a weighed linear least-squares regression is implemented using a second-degree polynomial. Finally, the smoothed value is calculated based on the weighed regression at the predictor value of interest. Data points may have outliers. Therefore, it is necessary to use a robust approach to obtain the bulk behavior of data. To achieve a robust method, the smoothing procedure is performed as explained above. The weights in Equation (4-40) are then updated as follows:

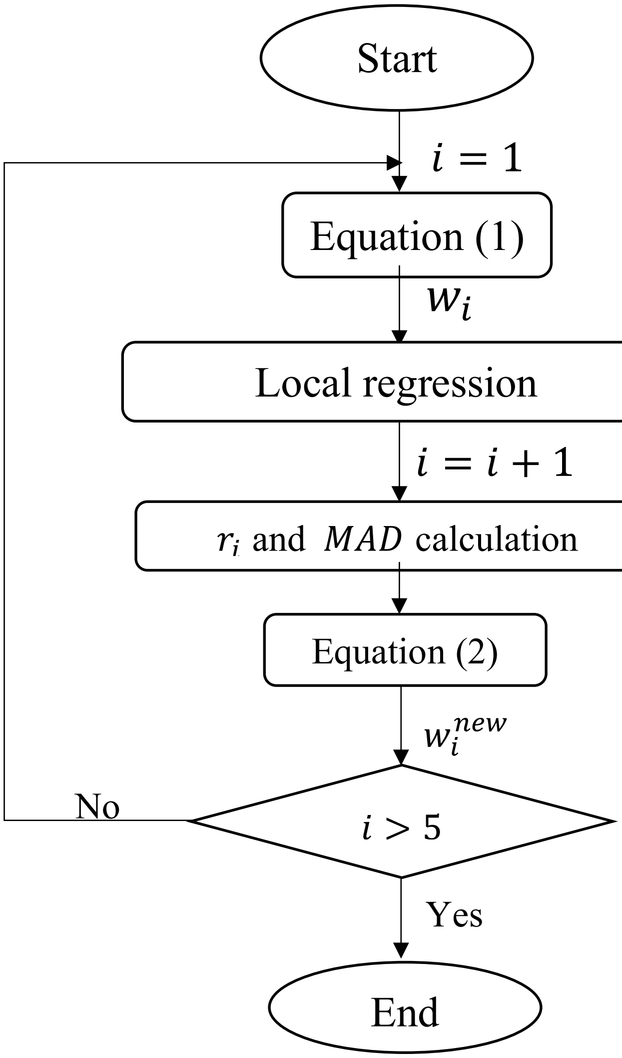

Figure 4-2: Smoothing Splines flow chart.

$$w_i = \begin{cases} \left(1 - \left(\frac{r_i}{6MAD}\right)^2\right)^2, & |r_i| < 6MAD \\ 0, & |r_i| \geq 6MAD \end{cases} \qquad (4\text{-}41)$$

where r_i indicates the residual of i^{th} smoothed point and MDA refers to the median absolute deviation of residuals. When the weights are updated, the local regression is run again to calculate residuals. Previous steps are applied five times. Figure 4-2 summarizes the robust local regression procedure.

This regression method of smoothing data is implemented by MATLAB smooth function. When the data is smoothed, a function should be defined to calculate the inflection point. In this study, we employ the Curve Fitting Toolbox of MATLAB to fit the data by the *Smoothing Splines* method.

4.2.4 Density Probability Histogram

In order to determine density of both phases, a probability histogram of calculated densities is obtained. The number of bins can affect the results. The number of bins (k) for data points (x) can be suggested directly or calculated based on assigned bin width (h) as given below:

$$k = \left\lceil \frac{x_{max} - x_{min}}{h} \right\rceil \tag{4-42}$$

where the braces are the ceiling function. The bins width (h) is calculated through using the Scott's normal reference rule as:

$$h = \frac{3.49\hat{\sigma}}{\sqrt[3]{n}} \tag{4-43}$$

in which, $\hat{\sigma}$ and n denote the standard deviation and number of data, respectively.

4.3 LIMITATIONS

The spurious velocity in the FF interface is related to the anisotropy order of the gradient operator. As the anisotropy is increased, the spurious velocity will decrease. The anisotropy order is constant in the current study. The density of both phases can be tuned through the Li et al. forcing scheme [89].

4.4 RESULTS AND DISCUSSION

In this section, the current study of surface wettability by LBM is divided to two main group. First, the surface wettability is studied at a static condition. Top and bottom sides of computation domain are assumed at no leak condition (solid wall) and periodic boundary condition is assumed for both left and right sides. In the second group of results same condition is applied except left and right boundaries of the computational domain. On these boundaries, constant velocity condition is applied in order to study the contact angle hysteresis.

4.4.1 Static drop study

In this section, the numerical setup will be first explained briefly. The fluctuation behavior of maximum spurious velocity in the presence of solid surface is shown. The new contact angle measurement is applied in a partially wetting case and its sensitivity to the limits of the selected interfacial density interval is studied. The importance of probability histogram in the phases' density is highlighted. Finally, the capability of the introduced model to simulate an extreme non-wetting condition without detaching the droplet is assessed.

For a static droplet case, a surface in a 500×100 lattice domain with periodical boundaries is considered. The same critical properties of the fluid reported in Yuan and Schaefer [91] are used. A droplet, which is considered as a semicircle with a radius of $r_{int} = 70$, is placed on a smooth surface. To simulate a homogenous wettability behavior, the wall density (ρ_w) is considered uniformly. For the chemically patterned surface cases, the wall density and SF interactions strength parameters (G_j) should be chosen based on the chemical properties. In the single component case, initial densities are determined by the Maxwell construction. Each test is run until the maximum relative spurious velocity ($U_{RS,max}$) meets the stability condition for the required times in a row. Spurious velocity is a proper criterion to evaluate the accuracy of LBM models in equilibrium cases. These non-physical velocities are present at equilibrium and, it seems that there is no mass exchange with them [36]. Figure 4-3 shows the magnitude of spurious velocity in the computational domain when the droplet is stabilized. Due to the periodic boundary condition, the wall is placed at the left and right sides of the domain . All points whose spurious velocities are greater than $0.95 \times U_{RS,max}$, are indicated by red points. All these points are at the gas-liquid interface. According to Figure 4-3, the spurious velocities are higher at the solid-liquid interface, compared to the solid-gas interface. The SF momentum exchange can be considered to determine the hydrodynamic boundary condition at the solid surface (e.g., slip and/or non-slip) [44].

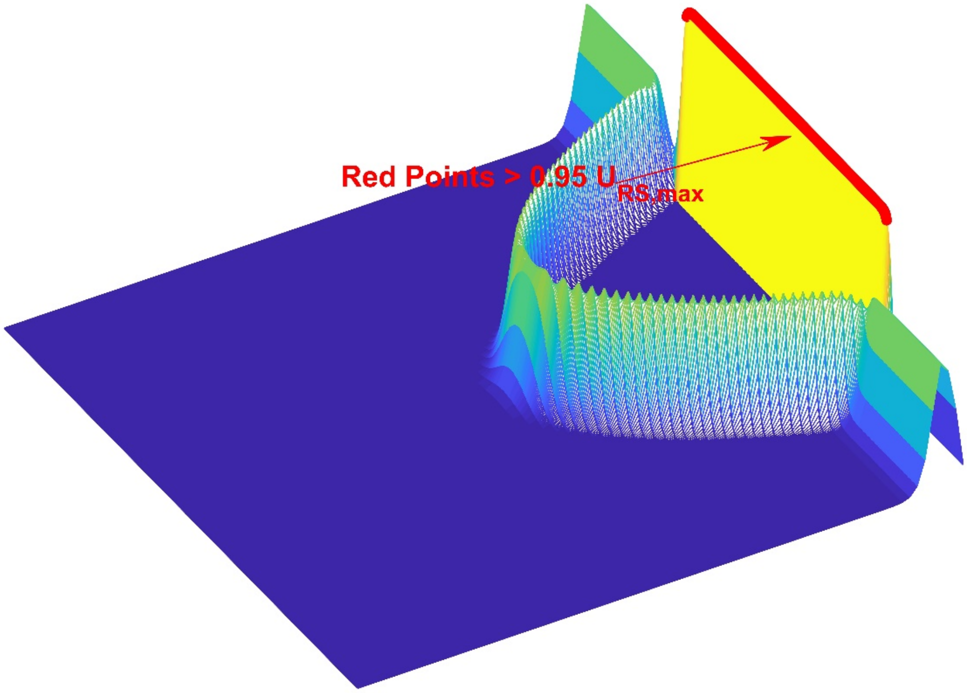

Figure 4-3: Spurious velocity in the computational domain. Red points represent the spurious velocities higher than $0.95|U_{s_{max}}|$.

Due to the fluctuation behavior, defining one point with a maximum relative spurious velocity less than the critical value (as the stabilized point) may not be safe, as depicted in Figure 4-4 [91]. Hence, the stability condition should meet for the required times in a row. Wagner shows that spurious velocities appear due to non-compatible discretization of driving forces for the order-parameter and momentum equations [106]. To decrease the spurious velocity in the pseudopotential LBM, several techniques including integration of different EOSs with LBM [91, 107], utilization of higher isotropy order of the interaction force [93, 108], interaction forces scheme modification [54, 109, 110], and use of MRT collision operator [58, 59] are introduced. The Carnahan-Starling EOS is used in this study. The universal gas constant R, attraction a, and repulsion parameters $b$are selected as 1, 0.5, 4 (all in lattice units), respectively.

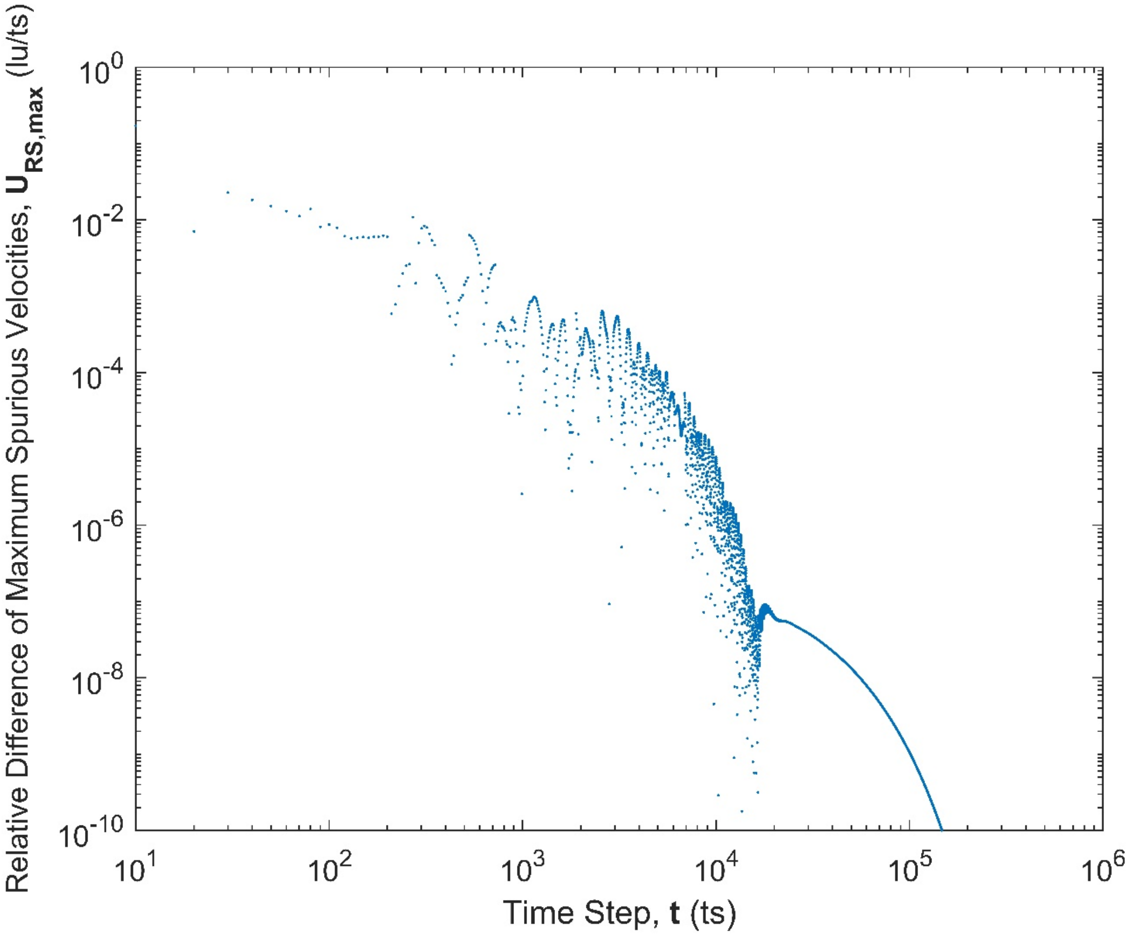

Figure 4-4: Maximum relative spurious velocities at different time steps.

As mentioned before, fitting a circle is a common method to determine the contact angle. This approach is limited to axisymmetric cases. A new method is introduced for non-axisymmetric cases in this work. As it is demonstrated in Figure 4-5, a line is fitted over the interface points, while the adsorption layer is also considered. The fluid density at the FF interface is decreased gradually, and the interface points are selected based on the pre-defined criteria of the interface density. The strength values, G_j, assigned for this case follow a pattern as $G_1 = 1$, and $G_j = -0.01 * e^{-2(j-2)}$, where $j = 2, \ldots, 7$. It should be noted that G_js are free parameters used to tune various surface properties. As it is shown in Figure 4-5, the *span* parameter of the *smoothing* function should be selected in the way to give the most preferable interface line. The generated line should be horizontal at the adsorption layer (e.g., zero curvature). Therefore, the *span* parameter is increased upon considering more interfacial points in the smoothing procedure, until it leads to a non-horizontal line in the adsorption layer. The red line is the fitted circle to the interface. For the smaller droplet cases with a higher surface absorption, the difference between contact angles obtained by the circle fitting and *Smoothing Splines* techniques will increase. Furthermore, *Smoothing Splines* technique is suitable for contact angle determination in both axisymmetric and non- axisymmetric cases. By comparing the new fitting approach based on smoothing splines and circle fitting, several differences are observed. For instance, the curvature of Smoothing Splines method is not constant which is because of possible disjoining pressure (see Equation (4-37)). van der Waals seems to be the most probable effective component (see Equation (4-34)). A deterministic method to observe the impact of the strength values, G_j, on observed disjoining pressure is highly recommended. Additionally, there is no need to assume constant G_j at all time steps. The strength values might change during time steps in some processes like non isothermal processes.

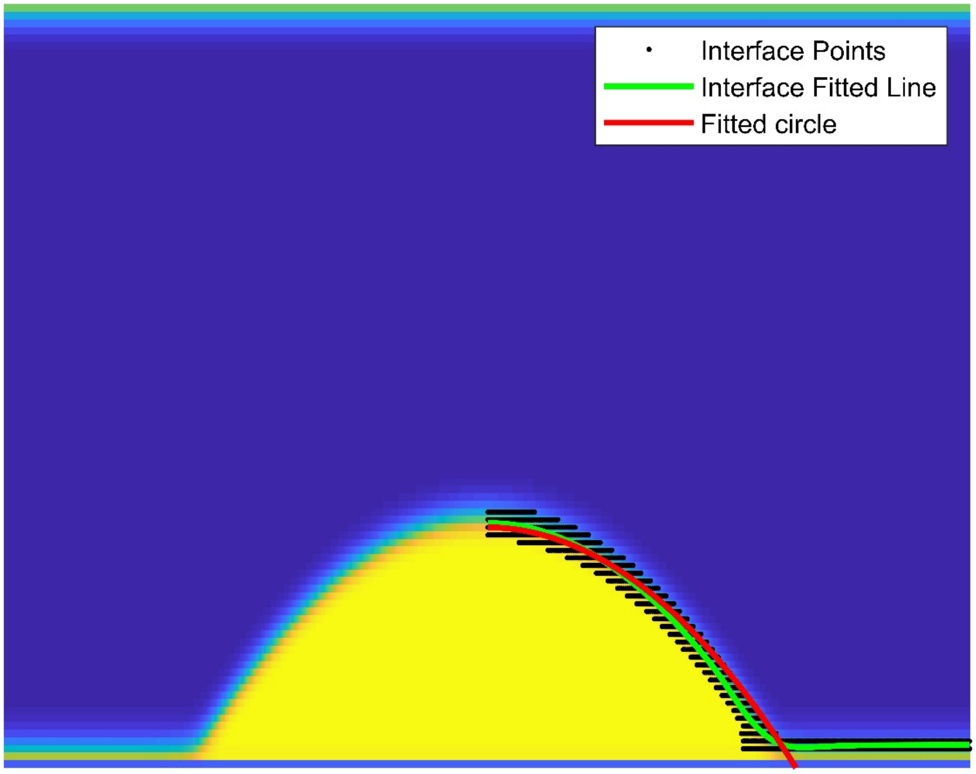

Figure 4-5: Interface selection: Smoothing Splines fitted function to define the interface.

The contact angle versus percentage of liquid density is illustrated in Figure 4-6 for the lower limit of the interfacial density interval, while Figure 4-7 presents the variation of contact angle with percentage of liquid density at the upper limit of interfacial density interval. It should be noted that both limits of the interfacial density interval are defined based on the percentage of the liquid phase density at the equilibrium. As the lower limit is increased, the magnitude of contact angle does not change considerably until the thickness of the adsorption layer lowers. The same trend happens for the upper limit sensitivity scenario (see Figure 4-6). Generally, one can conclude that the limit selection of the interfacial density interval does not change the measured contact angle appreciably when the new introduced contact angle measurement approach is implemented.

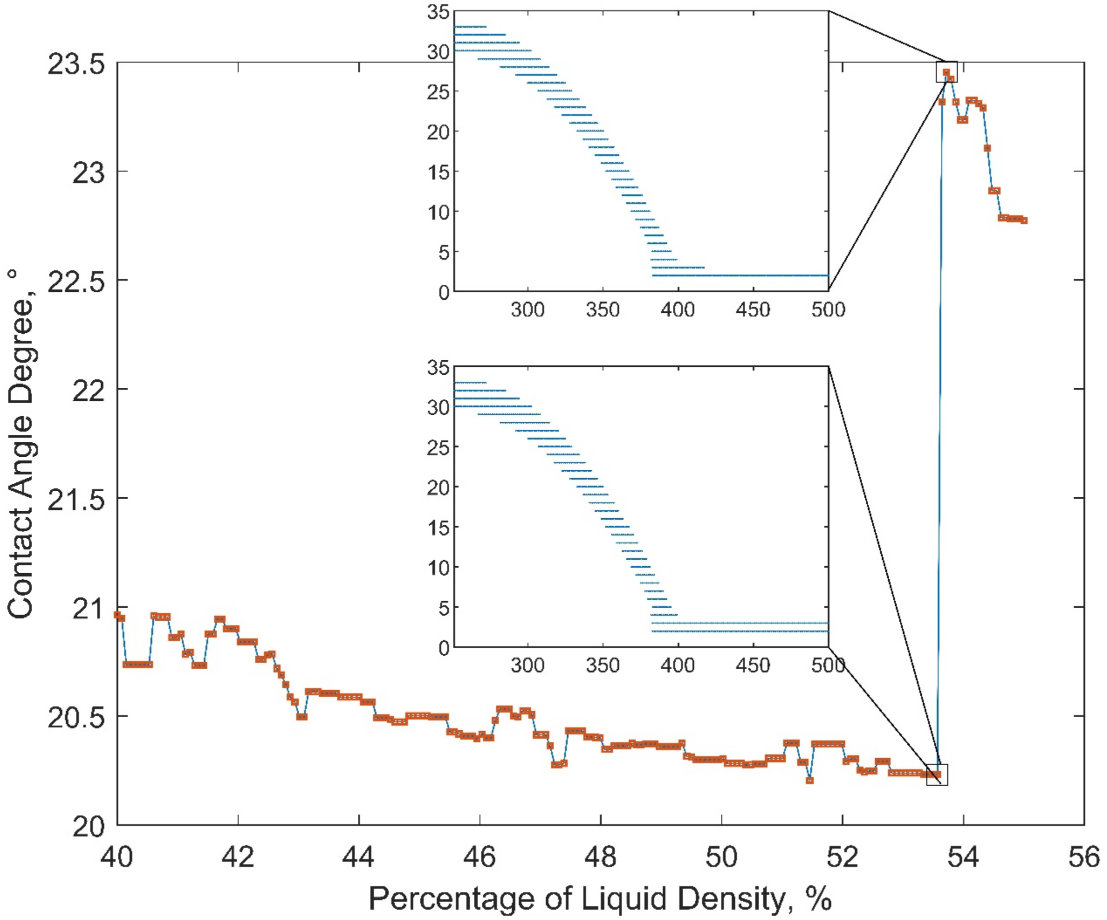

Figure 4-6: Effect of lower limit of interfacial density interval on measured contact angle.

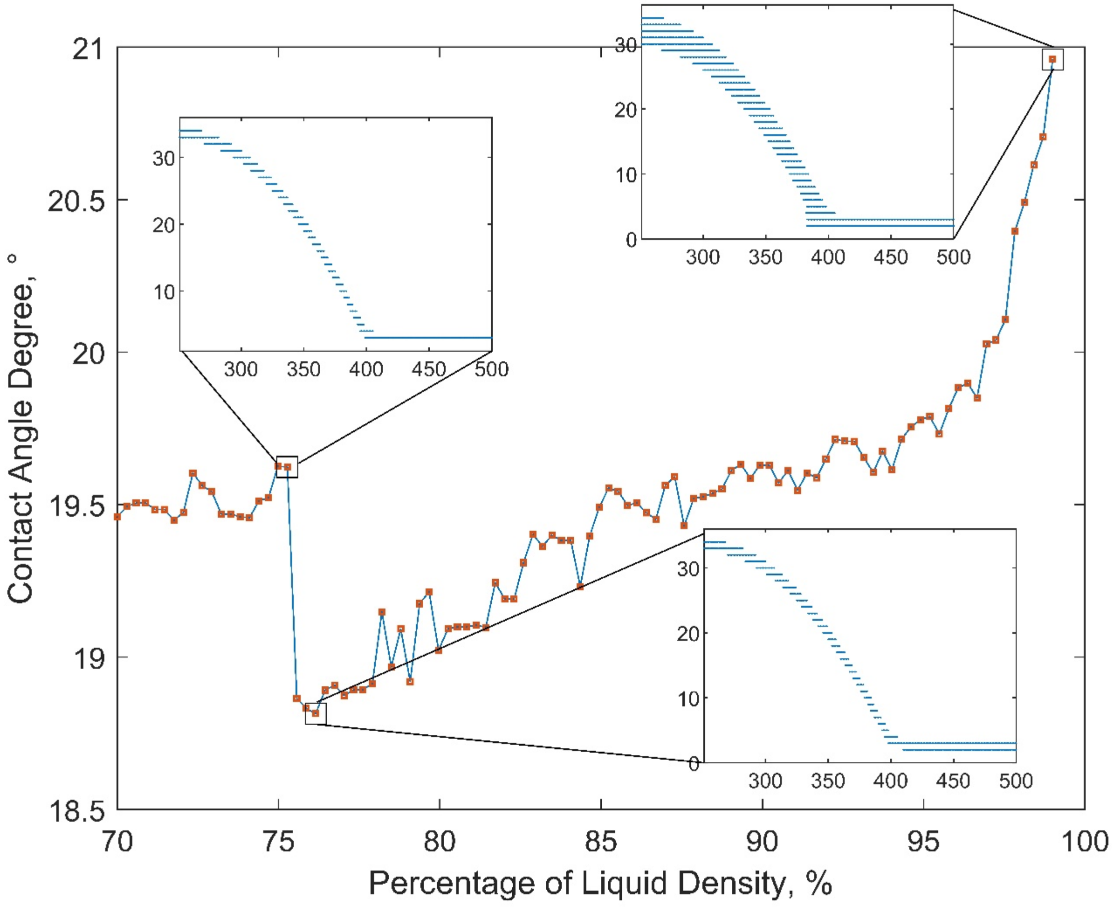

Figure 4-7: Measured contact angle sensitivity: the impact of upper limit of interfacial density interval.

The density is gradually changed at the interface; the density might also be different than Maxwell construction due to thermodynamic inconsistency in pseudopotential LBM and disjoining pressure (e.g., the augmented Young−Laplace equation). Therefore, the liquid and gas phase densities are calculated based on the density probability histogram of the domain. Figure 4-8 illustrates the probability histogram of the drop, shown in Figure 4-9, which is a bimodal distribution of the probability of the density. A high probability with a high density is considered as the liquid phase density, while a high probability with a low-density value is selected as the gas phase density. The selected densities might be altered by changing the number of bins (e.g., changing the intervals of densities in the histogram may affect the selected densities). It is worth noting that the highest and lowest densities are not always the selected densities.

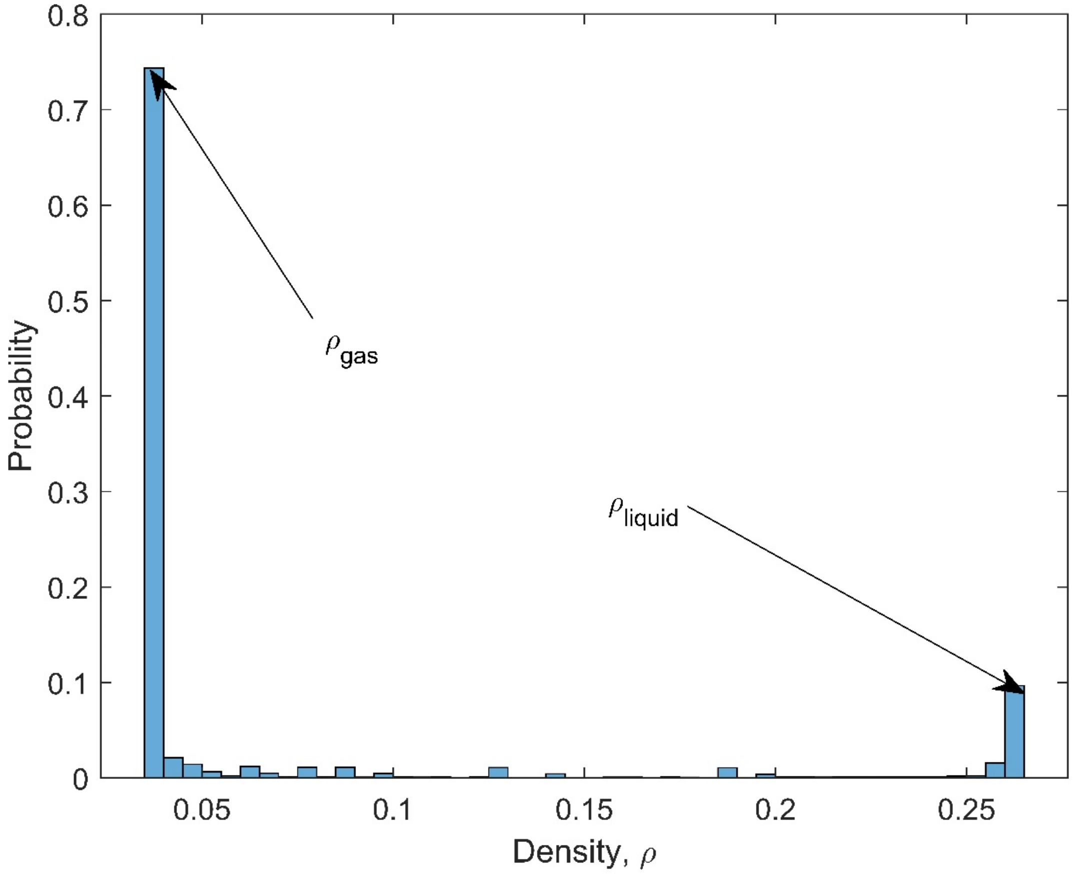

Figure 4-8: Histogram of probability of the fluid density.

Another limitation, which is tackled by the current approach, is the simulating of non-wetting conditions. Usually, the droplet will be detached from the surface when the LBM is used to simulate high contact angle cases. Li et al. was able to simulate extreme non-wetting conditions utilizing a new SF interaction approach [40]. Figure 4-11 exhibits the capability of the current SF interaction model. The extreme non-wetting case is simulated at different reduced temperatures (e.g., different density ratio). The surface adsorption and wettability behavior can be treated independently. For the case presented in Figure 4-12, the surface has a high adsorption potential; however, the adsorption is decreased for the case described in Figure 4-9. Figure 4-10 depicts the density histogram of different cases presented in Figure 4-15. For the high reduced temperature cases, the gas phase density is higher than the lowest density in the computational domain. On the other hand, the liquid phase density is lower than the highest density in the computational domain for the high reduced temperature cases.

The adsorption impacts on the fluid flow in porous media are simulated by LBM for single phase cases. To the best of the authors' knowledge, the adsorption phenomenon in multiphase flow through the porous media has not been evaluated by LBM, yet.

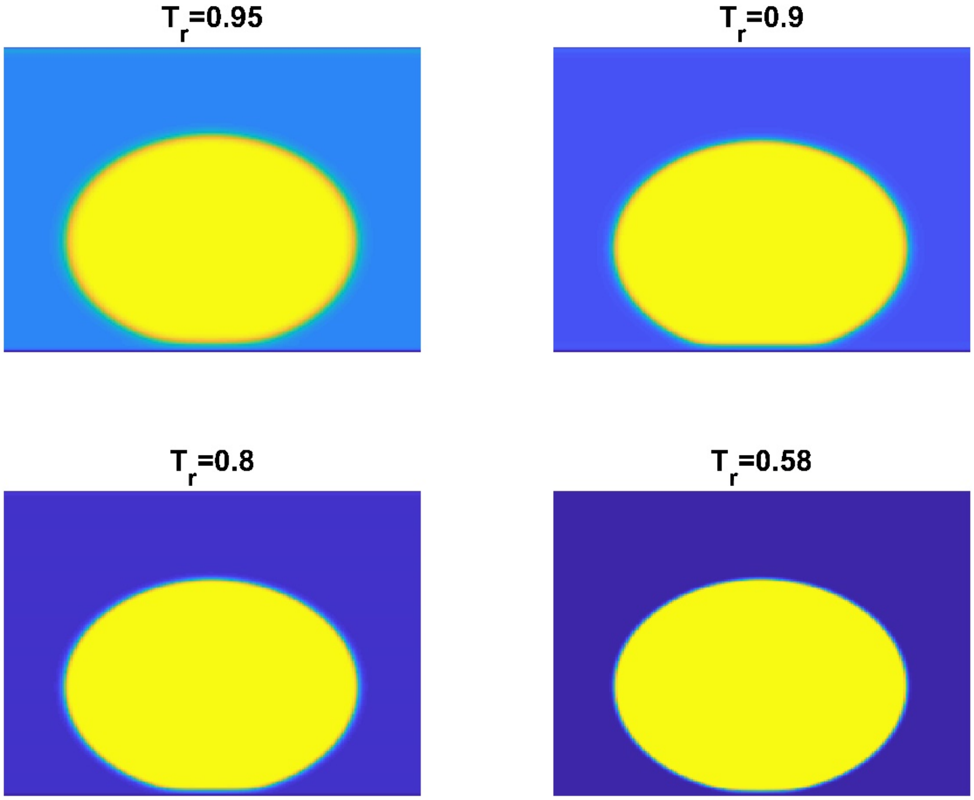

Figure 4-9: Contact angle of extreme non-wet cases obtained by the new SF interaction.

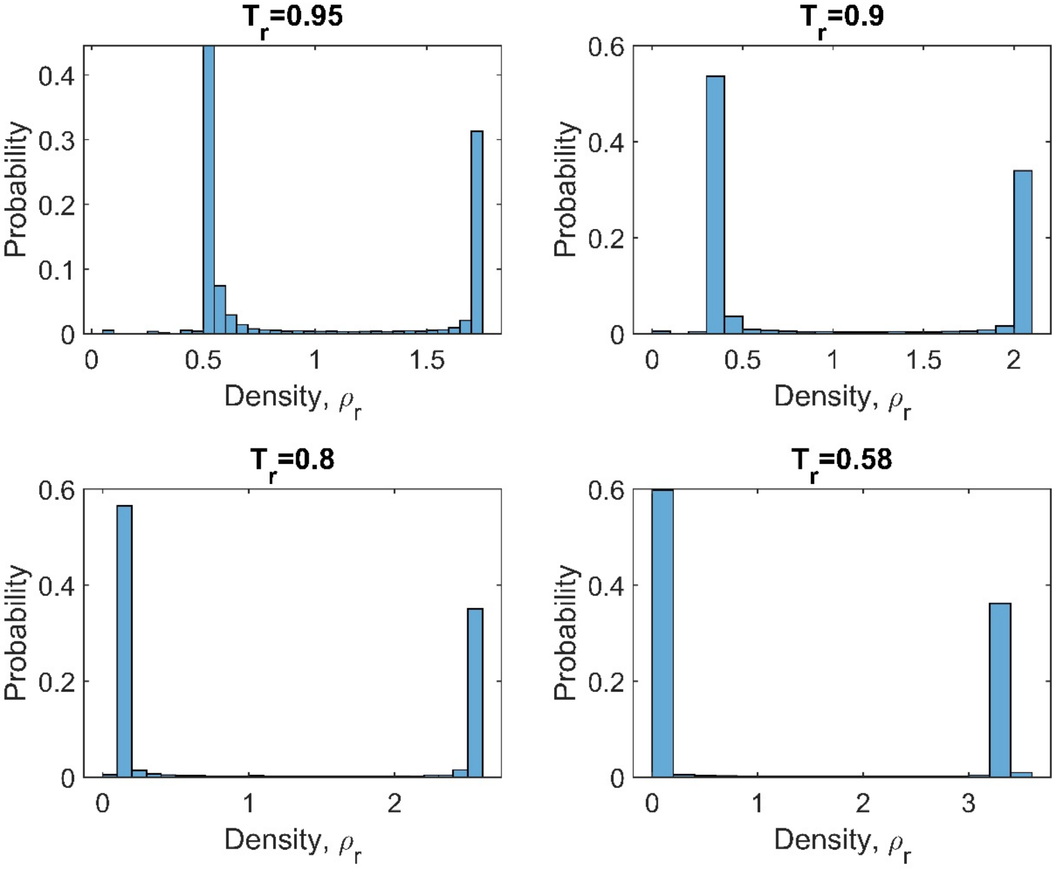

Figure 4-10: Density histogram of different cases in Figure 4-16.

4.4.2 Contact angle hysteresis (dynamic drop study)

As mentioned before, a computational domain with no leak (solid wall) on top and bottom side of domain is considered to mimic a channel. The constant velocity on both left and right side of the domain is assumed. Same as static drop case study, the domain size is considered as 200×200 and drop size is $R = 40$. The domain reduced temperature is constant at 0.875. The strength values are kept as $G_1 = 1$, and $G_j = -0.01 * e^{-2(j-2)}$, where $j = 2, \ldots, 7$. The flow system is controlled by dimensionless numbers such as a Reynolds number Re, Mach number, Ma. Thermodynamic parameters of EOS are kept as the static drop case. The velocity field is applied when the drop reache to a stable case then the density and vertex field is saved every five times step. In Figure 4-11Mach and Reynolds number are $Ma = 0.8$, $Re = 55.42$, and dynamic viscosity is $\eta = 1/6$. The flow direction is from left side toward right side. Figure 4-11 duplicated the contact angle changes during different time step. The central moments collision operator is implemented in this case study. The drop motion behaviour is shown in the Supplementary material section.

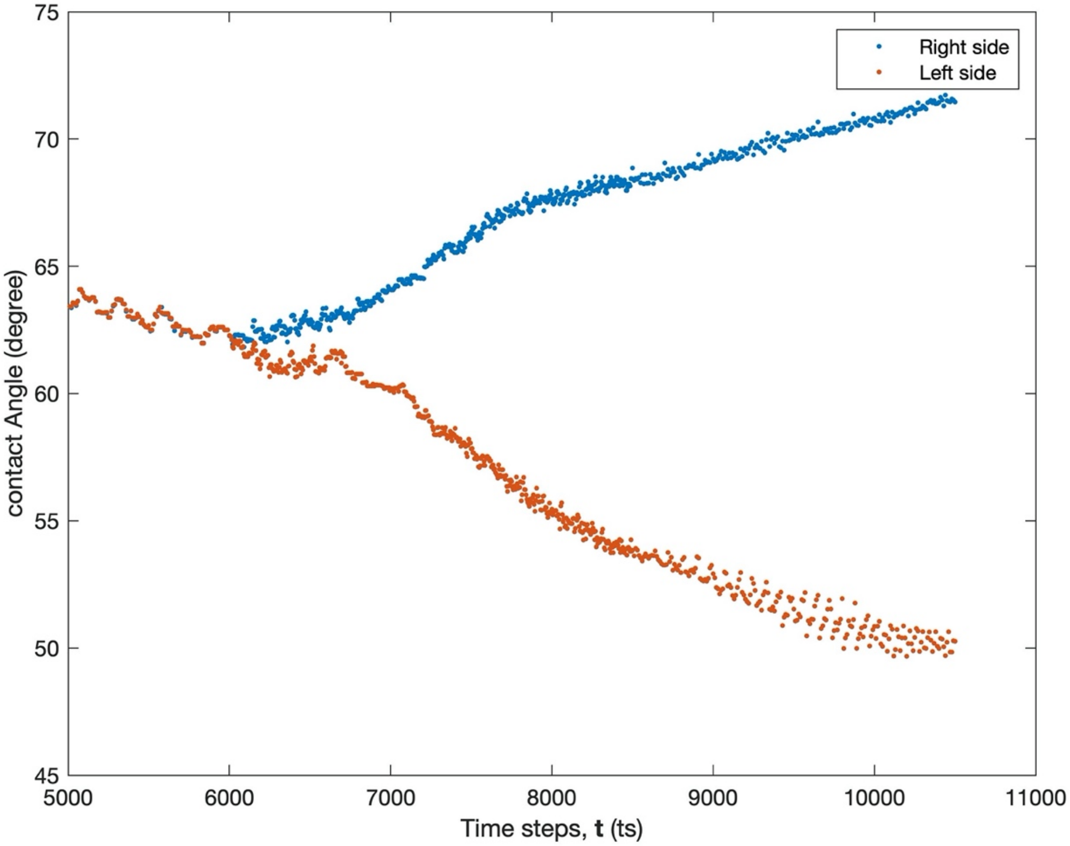

Figure 4-11: contact angle hysteresis: dynamic case study by central moment collision operator.

Capillary pressure introduces the surface wettability impact into the multiphase fluid flow behavior, particularly in the porous media. Capillary forces (pressure) play an important role in various applications such petroleum production/recovery, membrane separation, drug delivery, and shale gas thermodynamic behaviours [111, 112].

4.5 CONCLUSIONS

In this research, the pseudopotential LBM is systematically investigated to simulate the wettability phenomena and to more accurately mimic mechanisms such as disjoining pressure and surface adsorption. The main conclusions of this study are listed as follows:

- A new SF interaction is introduced to handle both surface adsorption and wettability, leading to a more reliable and accurate technique for contact angle determination.
- The role of maximum relative spurious velocities to simulate the steady state contact angle is further highlighted. The maximum relative spurious velocities have a fluctuational behavior.
- A new interfacial detection by *Smoothing Splines* is introduced. *Smoothing Splines* helps to determine the contact angle without imposing a specific function to the interface profile. Thus, the contact angle is calculated based on the disjoining pressure concept (e.g., the curvature of the interface profile is not assumed to be constant).
- The sensitivity of contact angle to the upper and lower limits of interfacial density interval is evaluated. The impact of the cutting edge selection of interface density on the measured contact angle is not considerable.
- The density of both phases should be selected based on the probability histogram of the domain density. Absorption may lead to deviations in the density probability histogram.

- New introduced SF interaction approach is able to simulate extreme non-wetting cases without detaching the droplet.
- Central moments collision operator is implemented to simulate high Mach number dynamic case study of surface wettability.

The $G_j s$ are free parameters used to tune different surface properties; they are assigned arbitrary. Finding a systematic approach to calculate these parameters can be useful. The solid surface in the current study is smooth and chemically homogeneous. Studying the wettability behavior of more complex surfaces such as chemically patterned surfaces and impacts of surface roughness and wettability on the fluid flow in the porous media appears to be promising.

ACKNOWLEDGEMENTS

Financial supports of Memorial University, Canada; the Natural Sciences and Engineering Research Council (NSERC) of Canada; and Equinor Canada are greatly acknowledged.

NOMENCLATURES

Acronyms

LBM = Lattice Boltzmann Method

SF = solid-fluid

CCS = Carbon Capture and Storage

EOR = Enhanced Oil Recovery

MD = Molecular Dynamics

EOS = Equation of State

ADSA = Axisymmetric Drop Shape Analysis

BGK = Bhatnagar−Gross−Krook

FF = Fluid-fluid

MRT = Multi Relaxation Time

C-S = Carnahan-Starling

MDA = median absolute deviation of residuals

Variables

A_{123} = Hamaker constant

c_0 = electrolyte concentration

c_s = speed of sound

e_i = discrete velocity vector

$f_i()$ = Density distribution function

G_f = FF interaction strength

G_w = SF strength strength

S_i = forcing source

F = Faraday’s constant

$h(x)$ = gas-liquid profile

p = Pressure

R = gas universal gas constant

$s()$ = Wall switch function

T = temperature

u = velocity

Greek symbols/variables

ω_i = Weight factors

ϵ_0 = dielectric constant of vacuum

σ_{12} = superficial tension

ϵ = dielectric constant of water

θ = Contact angle

ϑ = kinematic viscosity

ρ = density

τ = dimensionless relaxation time

φ = dimensionless electric potential

ψ = Pseudopotential (effective mass)

Subscripts

E = Electrostatic element

f = fluid

m = molecular element

max = Maximum

RS = Relative spurious velocity

S = Structural element

w = Wall

Superscripts

eq = equilibrium

REFERENCES

1. Carrasco, J., A. Hodgson, and A. Michaelides, A molecular perspective of water at metal interfaces. Nature materials, 2012. 11(8): p. 667.
2. Guo, J., et al., Real-space imaging of interfacial water with submolecular resolution. Nature materials, 2014. 13(2): p. 184.
3. Garland, E.R., et al., Structure of submonolayer oleic acid coverages on inorganic aerosol particles: evidence of island formation. Physical Chemistry Chemical Physics, 2008. 10(21): p. 3156-3161.
4. Li, Y., et al., Investigation of spontaneous imbibition by using a surfactant-free active silica water-based nanofluid for enhanced oil recovery. Energy & Fuels, 2017.
5. Lu, Y., N.F. Najafabadi, and A. Firoozabadi, Effect of Temperature on Wettability of Oil/Brine/Rock Systems. Energy & Fuels, 2017. 31(5): p. 4989-4995.
6. Zhang, H., et al., Enhanced oil recovery driven by nanofilm structural disjoining pressure: flooding experiments and microvisualization. Energy & Fuels, 2016. 30(4): p. 2771-2779.
7. Gong, S. and P. Cheng, Lattice Boltzmann simulation of periodic bubble nucleation, growth and departure from a heated surface in pool boiling. International Journal of Heat and Mass Transfer, 2013. 64: p. 122-132.
8. Li, Q., et al., Enhancement of boiling heat transfer using hydrophilic-hydrophobic mixed surfaces: A lattice Boltzmann study. Applied Thermal Engineering, 2018. 132: p. 490-499.
9. Arif, M., A. Barifcani, and S. Iglauer, Solid/CO2 and solid/water interfacial tensions as a function of pressure, temperature, salinity and mineral type: Implications for CO2-

wettability and CO2 geo-storage. International Journal of Greenhouse Gas Control, 2016. 53: p. 263-273.

10. Iglauer, S., et al., CO2 wettability of caprocks: Implications for structural storage capacity and containment security. Geophysical Research Letters, 2015. 42(21): p. 9279-9284.
11. Zhang, J. and D.Y. Kwok, Contact line and contact angle dynamics in superhydrophobic channels. Langmuir, 2006. 22(11): p. 4998-5004.
12. Zhang, J. and D.Y. Kwok, Lattice Boltzmann Study on the Contact Angle and Contact Line Dynamics of Liquid− Vapor Interfaces. Langmuir, 2004. 20(19): p. 8137-8141.
13. Davies, A.R., J.L. Summers, and M.C. Wilson, On a dynamic wetting model for the finite-density multiphase lattice Boltzmann method. International Journal of Computational Fluid Dynamics, 2006. 20(6): p. 415-425.
14. Cottin-Bizonne, C., et al., Dynamics of simple liquids at heterogeneous surfaces: Molecular-dynamics simulations and hydrodynamic description. The European Physical Journal E, 2004. 15(4): p. 427-438.
15. Priezjev, N.V., A.A. Darhuber, and S.M. Troian, Slip behavior in liquid films on surfaces of patterned wettability: Comparison between continuum and molecular dynamics simulations. Physical Review E, 2005. 71(4): p. 041608.
16. Qian, T., X.-P. Wang, and P. Sheng, A variational approach to moving contact line hydrodynamics. Journal of Fluid Mechanics, 2006. 564: p. 333-360.
17. Jiménez-Ángeles, F. and A. Firoozabadi, Tunable substrate wettability by thin water layer. The Journal of Physical Chemistry C, 2016. 120(43): p. 24688-24696.

18. Jiménez-Ángeles, F. and A. Firoozabadi, Contact Angle, Liquid Film, and Liquid–Liquid and Liquid–Solid Interfaces in Model Oil–Brine–Substrate Systems. The Journal of Physical Chemistry C, 2016. 120(22): p. 11910-11917.

19. Brenner, H. and V. Ganesan, Molecular wall effects: Are conditions at a boundary “boundary conditions”? Physical Review E, 2000. 61(6): p. 6879.

20. Huang, H., M. Sukop, and X. Lu, Multiphase lattice Boltzmann methods: Theory and application. 2015: John Wiley & Sons.

21. Liu, H., et al., Multiphase lattice Boltzmann simulations for porous media applications. Computational Geosciences, 2016. 20(4): p. 777-805.

22. Rothman, D.H. and J.M. Keller, Immiscible cellular-automaton fluids. Journal of Statistical Physics, 1988. 52(3-4): p. 1119-1127.

23. Gunstensen, A.K., et al., Lattice Boltzmann model of immiscible fluids. Physical Review A, 1991. 43(8): p. 4320.

24. Swift, M.R., W. Osborn, and J. Yeomans, Lattice Boltzmann simulation of nonideal fluids. Physical review letters, 1995. 75(5): p. 830.

25. Shan, X. and H. Chen, Lattice Boltzmann model for simulating flows with multiple phases and components. Physical Review E, 1993. 47(3): p. 1815.

26. Shan, X. and H. Chen, Simulation of nonideal gases and liquid-gas phase transitions by the lattice Boltzmann equation. Physical Review E, 1994. 49(4): p. 2941.

27. Shan, X. and G. Doolen, Multicomponent lattice-Boltzmann model with interparticle interaction. Journal of Statistical Physics, 1995. 81(1-2): p. 379-393.

28. Shan, X. and G. Doolen, Diffusion in a multicomponent lattice Boltzmann equation model. Physical Review E, 1996. 54(4): p. 3614.

29. Chen, S. and G.D. Doolen, Lattice Boltzmann method for fluid flows. Annual review of fluid mechanics, 1998. 30(1): p. 329-364.
30. Fei, L. and K.H. Luo, Consistent forcing scheme in the cascaded lattice Boltzmann method. Physical Review E, 2017. 96(5): p. 053307.
31. Benzi, R., S. Succi, and M. Vergassola, The lattice Boltzmann equation: theory and applications. Physics Reports, 1992. 222(3): p. 145-197.
32. Chen, L., et al., A critical review of the pseudopotential multiphase lattice Boltzmann model: Methods and applications. International Journal of Heat and Mass Transfer, 2014. 76: p. 210-236.
33. Succi, S. and S. Succi, The lattice Boltzmann equation: for fluid dynamics and beyond. 2001: Oxford university press.
34. Wolf-Gladrow, D.A., Lattice-gas cellular automata and lattice Boltzmann models: an introduction. 2004: Springer.
35. Martys, N.S. and H. Chen, Simulation of multicomponent fluids in complex three-dimensional geometries by the lattice Boltzmann method. Physical review E, 1996. 53(1): p. 743.
36. Sukop, M., DT Thorne, Jr. Lattice Boltzmann Modeling Lattice Boltzmann Modeling. 2006.
37. Raiskinmäki, P., et al., Lattice-Boltzmann simulation of capillary rise dynamics. Journal of statistical physics, 2002. 107(1-2): p. 143-158.
38. Raiskinmäki, P., et al., Spreading dynamics of three-dimensional droplets by the lattice-Boltzmann method. Computational Materials Science, 2000. 18(1): p. 7-12.

39. Benzi, R., et al., Mesoscopic modeling of a two-phase flow in the presence of boundaries: the contact angle. Physical Review E, 2006. 74(2): p. 021509.

40. Li, Q., et al., Contact angles in the pseudopotential lattice Boltzmann modeling of wetting. Physical Review E, 2014. 90(5): p. 053301.

41. Hu, A., et al., Contact angle adjustment in equation-of-state-based pseudopotential model. Physical Review E, 2016. 93(5): p. 053307.

42. Ding, H. and P.D. Spelt, Wetting condition in diffuse interface simulations of contact line motion. Physical Review E, 2007. 75(4): p. 046708.

43. Guo, L., et al., Modeling adsorption with lattice Boltzmann equation. Scientific reports, 2016. 6: p. 27134.

44. Colosqui, C.E., et al., Mesoscopic model for microscale hydrodynamics and interfacial phenomena: Slip, films, and contact-angle hysteresis. Physical Review E, 2013. 87(1): p. 013302.

45. Huang, H., et al., Proposed approximation for contact angles in Shan-and-Chen-type multicomponent multiphase lattice Boltzmann models. Physical Review E, 2007. 76(6): p. 066701.

46. Bao, J. and L. Schaefer, Lattice Boltzmann equation model for multi-component multi-phase flow with high density ratios. Applied Mathematical Modelling, 2013. 37(4): p. 1860-1871.

47. Starov, V. and M. Velarde, Surface forces and wetting phenomena. Journal of Physics: Condensed Matter, 2009. 21(46): p. 464121.

48. Samoila, F. and L. Sirghi, Disjoining pressure in partial wetting on the nanoscale. Langmuir, 2017. 33(21): p. 5188-5196.

49. Wang, H., From contact line structures to wetting dynamics. Langmuir, 2019. 35(32): p. 10233-10245.

50. Fang, C., S. Sun, and R. Qiao, Structure, Thermodynamics, and Dynamics of Thin Brine Films in Oil–Brine–Rock Systems. Langmuir, 2019. 35(32): p. 10341-10353.

51. Del Rıo, O. and A. Neumann, Axisymmetric drop shape analysis: computational methods for the measurement of interfacial properties from the shape and dimensions of pendant and sessile drops. Journal of colloid and interface science, 1997. 196(2): p. 136-147.

52. Bateni, A., et al., A high-accuracy polynomial fitting approach to determine contact angles. Colloids and Surfaces A: Physicochemical and Engineering Aspects, 2003. 219(1-3): p. 215-231.

53. Bhatnagar, P.L., E.P. Gross, and M. Krook, A model for collision processes in gases. I. Small amplitude processes in charged and neutral one-component systems. Physical review, 1954. 94(3): p. 511.

54. Huang, H., M. Krafczyk, and X. Lu, Forcing term in single-phase and Shan-Chen-type multiphase lattice Boltzmann models. Physical Review E, 2011. 84(4): p. 046710.

55. d'Humieres, D., Multiple–relaxation–time lattice Boltzmann models in three dimensions. Philosophical Transactions of the Royal Society of London. Series A: Mathematical, Physical and Engineering Sciences, 2002. 360(1792): p. 437-451.

56. Marié, S., D. Ricot, and P. Sagaut, Comparison between lattice Boltzmann method and Navier–Stokes high order schemes for computational aeroacoustics. Journal of Computational Physics, 2009. 228(4): p. 1056-1070.

57. Lallemand, P. and L.-S. Luo, Theory of the lattice Boltzmann method: Dispersion, dissipation, isotropy, Galilean invariance, and stability. Physical Review E, 2000. 61(6): p. 6546.

58. Yu, Z. and L.-S. Fan, Multirelaxation-time interaction-potential-based lattice Boltzmann model for two-phase flow. Physical Review E, 2010. 82(4): p. 046708.

59. Li, Q., K. Luo, and X. Li, Lattice Boltzmann modeling of multiphase flows at large density ratio with an improved pseudopotential model. Physical Review E, 2013. 87(5): p. 053301.

60. Geier, M., A. Greiner, and J.G. Korvink, Cascaded digital lattice Boltzmann automata for high Reynolds number flow. Physical Review E, 2006. 73(6): p. 066705.

61. Premnath, K.N. and S. Banerjee, On the three-dimensional central moment lattice Boltzmann method. Journal of Statistical Physics, 2011. 143(4): p. 747-794.

62. Geier, M., A. Greiner, and J.G. Korvink, Properties of the cascaded lattice Boltzmann automaton. International Journal of Modern Physics C, 2007. 18(04): p. 455-462.

63. Asinari, P., Generalized local equilibrium in the cascaded lattice Boltzmann method. Physical Review E, 2008. 78(1): p. 016701.

64. Geier, M., De-aliasing and stabilization formalism of the cascaded lattice Boltzmann automaton for under-resolved high Reynolds number flow. International journal for numerical methods in fluids, 2008. 56(8): p. 1249-1254.

65. Geier, M., A. Greiner, and J.G. Korvink, A factorized central moment lattice Boltzmann method. The European Physical Journal Special Topics, 2009. 171(1): p. 55-61.

66. Premnath, K.N. and S. Banerjee, Incorporating forcing terms in cascaded lattice Boltzmann approach by method of central moments. Physical Review E, 2009. 80(3): p. 036702.

67. Geier, M., et al., The cumulant lattice Boltzmann equation in three dimensions: Theory and validation. Computers & Mathematics with Applications, 2015. 70(4): p. 507-547.

68. De Rosis, A. and E. Lévêque, Central-moment lattice Boltzmann schemes with fixed and moving immersed boundaries. Computers & Mathematics with Applications, 2016. 72(6): p. 1616-1628.

69. De Rosis, A., Alternative formulation to incorporate forcing terms in a lattice Boltzmann scheme with central moments. Physical Review E, 2017. 95(2): p. 023311.

70. Geier, M., A. Pasquali, and M. Schönherr, Parametrization of the cumulant lattice Boltzmann method for fourth order accurate diffusion part I: Derivation and validation. Journal of Computational Physics, 2017. 348: p. 862-888.

71. Geier, M., A. Pasquali, and M. Schönherr, Parametrization of the cumulant lattice Boltzmann method for fourth order accurate diffusion Part II: Application to flow around a sphere at drag crisis. Journal of Computational Physics, 2017. 348: p. 889-898.

72. Kumar, C.S., et al., Numerical investigations on convective heat transfer enhancement in jet impingement due to the presence of porous media using cascaded lattice Boltzmann method. International Journal of Thermal Sciences, 2017. 122: p. 201-217.

73. Shah, N., et al., Cascaded collision lattice Boltzmann model (CLBM) for simulating fluid and heat transport in porous media. Numerical Heat Transfer, Part B: Fundamentals, 2017. 72(3): p. 211-232.

74. Sharma, K.V., R. Straka, and F.W. Tavares, New Cascaded Thermal Lattice Boltzmann Method for simulations of advection-diffusion and convective heat transfer. International Journal of Thermal Sciences, 2017. 118: p. 259-277.

75. Fei, L. and K.H. Luo, Cascaded lattice Boltzmann method for thermal flows on standard lattices. International Journal of Thermal Sciences, 2018. 132: p. 368-377.

76. Fei, L. and K.H. Luo, Cascaded lattice Boltzmann method for incompressible thermal flows with heat sources and general thermal boundary conditions. Computers & Fluids, 2018. 165: p. 89-95.

77. Fei, L., K.H. Luo, and Q. Li, Three-dimensional cascaded lattice Boltzmann method: Improved implementation and consistent forcing scheme. Physical Review E, 2018. 97(5): p. 053309.

78. Geier, M. and A. Pasquali, Fourth order Galilean invariance for the lattice Boltzmann method. Computers & Fluids, 2018. 166: p. 139-151.

79. De Rosis, A., Nonorthogonal central-moments-based lattice Boltzmann scheme in three dimensions. Physical Review E, 2017. 95(1): p. 013310.

80. Rosis, A.D., R. Huang, and C. Coreixas, Universal formulation of central-moments-based lattice Boltzmann method with external forcing for the simulation of multiphysics phenomena. Physics of Fluids, 2019. 31: p. 117102.

81. Premnath, K.N. and J. Abraham, Three-dimensional multi-relaxation time (MRT) lattice-Boltzmann models for multiphase flow. Journal of Computational Physics, 2007. 224(2): p. 539-559.

82. Lallemand, P. and L.-S. Luo, Theory of the lattice Boltzmann method: Acoustic and thermal properties in two and three dimensions. Physical review E, 2003. 68(3): p. 036706.

83. Malaspinas, O., Increasing stability and accuracy of the lattice Boltzmann scheme: recursivity and regularization. arXiv preprint arXiv:1505.06900, 2015.

84. Coreixas, C., et al., Recursive regularization step for high-order lattice Boltzmann methods. Physical Review E, 2017. 96(3): p. 033306.

85. Coreixas, C.G., High-order extension of the recursive regularized lattice Boltzmann method. 2018.

86. De Rosis, A. and K.H. Luo, Role of higher-order Hermite polynomials in the central-moments-based lattice Boltzmann framework. Physical Review E, 2019. 99(1): p. 013301.

87. Huang, R., H. Wu, and N.A. Adams, Eliminating cubic terms in the pseudopotential lattice Boltzmann model for multiphase flow. Physical Review E, 2018. 97(5): p. 053308.

88. Guo, Z., C. Zheng, and B. Shi, Discrete lattice effects on the forcing term in the lattice Boltzmann method. Physical Review E, 2002. 65(4): p. 046308.

89. Li, Q., K.H. Luo, and X. Li, Forcing scheme in pseudopotential lattice Boltzmann model for multiphase flows. Physical Review E, 2012. 86(1): p. 016709.

90. Shan, X., Pressure tensor calculation in a class of nonideal gas lattice Boltzmann models. Physical Review E, 2008. 77(6): p. 066702.

91. Yuan, P. and L. Schaefer, Equations of state in a lattice Boltzmann model. Physics of Fluids, 2006. 18(4): p. 042101.

92. Li, Q. and K. Luo, Achieving tunable surface tension in the pseudopotential lattice Boltzmann modeling of multiphase flows. Physical Review E, 2013. 88(5): p. 053307.

93. Sbragaglia, M., et al., Generalized lattice Boltzmann method with multirange pseudopotential. Physical Review E, 2007. 75(2): p. 026702.

94. Churaev, N.V., B.V. Derjaguin, and V.M. Muller, Surface forces. 2013: Springer Science & Business Media.

95. Churaev, N. and V. Sobolev, Prediction of contact angles on the basis of the Frumkin-Derjaguin approach. Advances in colloid and interface science, 1995. 61: p. 1-16.

96. Churaev, N., V. Sobolev, and V. Starov, Disjoining pressure of thin nonfreezing interlayers. Journal of colloid and interface science, 2002. 247(1): p. 80-83.

97. Kuchin, I., et al., Influence of the disjoining pressure on the equilibrium interfacial profile in transition zone between a thin film and a capillary meniscus. Colloids and Interface Science Communications, 2014. 1: p. 18-22.

98. Churaev, N. and V. Sobolev, Wetting of low-energy surfaces. Advances in colloid and interface science, 2007. 134: p. 15-23.

99. Israelachvili, J.N., Intermolecular and surface forces. 2011: Academic press.

100. Dai, B., L.G. Leal, and A. Redondo, Disjoining pressure for nonuniform thin films. Physical Review E, 2008. 78(6): p. 061602.

101. Benet, J., et al., Disjoining Pressure, Healing Distance, and Film Height Dependent Surface Tension of Thin Wetting Films. The Journal of Physical Chemistry C, 2014. 118(38): p. 22079-22089.

102. Colosqui, C.E., et al., Mesoscopic model for microscale hydrodynamics and interfacial phenomena: slip, films, and contact-angle hysteresis. Phys Rev E Stat Nonlin Soft Matter Phys, 2013. 87(1): p. 013302.

103. Li, Q., P. Zhou, and H. Yan, Pinning–depinning mechanism of the contact line during evaporation on chemically patterned surfaces: a lattice Boltzmann study. Langmuir, 2016. 32(37): p. 9389-9396.

104. Zheng, H., C. Shu, and Y.-T. Chew, A lattice Boltzmann model for multiphase flows with large density ratio. Journal of Computational Physics, 2006. 218(1): p. 353-371.

105. Lee, T. and C.-L. Lin, A stable discretization of the lattice Boltzmann equation for simulation of incompressible two-phase flows at high density ratio. Journal of Computational Physics, 2005. 206(1): p. 16-47.

106. Wagner, A.J., The origin of spurious velocities in lattice Boltzmann. International Journal of Modern Physics B, 2003. 17(01n02): p. 193-196.

107. Zhang, J. and F. Tian, A bottom-up approach to non-ideal fluids in the lattice Boltzmann method. EPL (Europhysics Letters), 2008. 81(6): p. 66005.

108. Shan, X., Analysis and reduction of the spurious current in a class of multiphase lattice Boltzmann models. Physical Review E, 2006. 73(4): p. 047701.

109. Li, Q., K. Luo, and X. Li, Forcing scheme in pseudopotential lattice Boltzmann model for multiphase flows. Physical Review E, 2012. 86(1): p. 016709.

110. Sun, K., et al., Evaluation of force implementation in pseudopotential-based multiphase lattice Boltzmann models. Physica A: Statistical Mechanics and its Applications, 2012. 391(15): p. 3895-3907.

111. Jin, Z. and A. Firoozabadi, Thermodynamic modeling of phase behavior in shale media. SPE Journal, 2016. 21(01): p. 190-207.

112. Nojabaei, B., R.T. Johns, and L. Chu, Effect of capillary pressure on phase behavior in tight rocks and shales. SPE Reservoir Evaluation & Engineering, 2013. 16(03): p. 281-289.

5. CHAPTER FIVE

Summary and Recommendations for Future Work

This research work focuses on improving LBM to simulate fluid-fluid and solid-fluid interactions. Thermodynamic consistency is improved by integrating the CPA EOS with LBM and decreasing the spurious velocity by using higher-order isotropic gradient operator. Central moments collision operator is implemented to increase the model stability at high Reynolds number conditions. A new solid-fluid interaction scheme is introduced to improve the simulation of surface wettability. This thesis includes three main sections: incorporating CPA EOS in the LBM (Chapter 2), implementing central moments in the LBM (Chapter 3), and improving surface wettability simulation (Chapter 4).

5.1 Fluid-Fluid interactions

Some fluids associate due to hydrogen bonding. To simulate unusual thermodynamic behaviours, CPA EOS is integrated with LBM. The thermodynamic consistency of LBM results is verified by Maxwell equal area construction. The modeling results are then compared with the experimental data of water to show the reliability of outputs. To increase the stability of the model, the central moments collision operator is applied in the pseudopotential approach of LBM. The main findings/conclusions of the first phase are as follows:

- Sbragaglia and Shan (SS) and Shan and Chen (SC) EOSs, which are commonly used in LBM simulations, do not have sufficient flexibility to predict the fluid phase behaviors. The approach introduced in this thesis fills this knowledge gap.
- Better thermodynamic consistency in LBM results is achieved in both the liquid and gas phases when CPA EOS is utilized for associating fluids.
- The global optimization approach is implemented to determine the CPA EOS constants in the lattice units.

- There is better agreement between LBM results and experimental data when CPA EOS is incorporated in the model in comparison with PR EOS.
- Li et al.'s forcing scheme is applied when CPA EOS is used; not only thermodynamic consistency is improved, but also the model stability is increased at lower reduced temperatures.
- To increase the stability at lower temperature, an extended form of CPA EOS is proposed to determine the initial densities.
- CPA/LBM approach shows a reliable behaviour of the interfacial tension of water as a function of the reduced temperature.
- In comparison with MRT collision operator, central moments-based LBM with a high-order Hermite polynomial is more stable in double sheer layer test at high Reynolds number.

5.2 Solid-Fluid interactions

In this research phase, the pseudopotential LBM approach is examined to simulate the wettability phenomena; vital mechanisms such as disjoining pressure and surface adsorption are mimicked accurately. The main outcomes of this phase are as follows:

- New solid-fluid interaction is proposed to handle both surface absorption and surface wettability.
- A new contact angle measurement is introduced based on Smoothing Splines technique. In spite of the circle where the curvature is constant, it is not constant in this method. Thus, the effect of disjoining pressure should be taken into account in the contact angle measurements.

- The probability histogram is presented as a tool to measure the phase density in the presence of a surface.
- New solid-fluid interaction is able to simulate high non-wetting case without detaching the drop.

5.3 Recommendations for Future Work

Simulating fluid-fluid and solid-fluid interactions by LBM, the following recommendations for future work are summarized:

- In the fluid-fluid interaction, a single range approach is implemented mostly. The interfacial tension can be handled by a multirange pseudopotential approach.
- Implementing central moments collision operator increases the stability of the model at high Reynolds number, which can be an asset for simulating fluid flow in low permeable porous media.
- The surfaces used in the current research are smooth and chemically homogenous. Thus, heterogeneous and rough surfaces can be considered to better simulate real cases.
- In the current study, cases are assumed at the isothermal condition. Adding an energy balance equation to the current model can be a significant improvement while studying phase change phenomena.
- Considering the nucleation in the current model can be helpful for various processes/phenomena such as asphaltene precipitation and hydrate formation.
- Increasing the number of phases and components to simulate processes that involve multiphase flow and chemical reactions.

- Implementing more robust non-cubic equations of state such as PC-SAFT and comparing the results with the outputs of CPA and common cubic equations of state in terms of the equilibrium stability, accuracy, and computational costs.
- Examining different force schemes such as exact difference method (EDM) and method of explicit derivative (MED) in simulation of multiphase systems at various process and thermodynamic conditions and comparing results in terms of stability, accuracy, and computational time.
- Further investigation of multiphase flow using the entropic multiple-relaxation-time multirange pseudopotential lattice Boltzmann model (EMRT-MP LBM) to simulate complex fluid-fluid and fluid-solid interfacial phenomena for a broad range of Weber numbers and Reynolds numbers at high density ratios. The performance of EMRT-MP strategy can be then compared with central moments collision operator approach.